

An Investigation into Neural Tissue-Electrode Contact as a  
Performance Impairing Factor in Flexible, Micro-  
Electrocorticographic Probes Meant for Brain-Computer Interfacing

by

Joshua Michael Cunningham

A thesis submitted in partial fulfillment of the requirements for the degree of

Master of Science  
in  
Materials Engineering

Department of Chemical and Materials Engineering

University of Alberta

© Joshua Michael Cunningham, 2017

# ABSTRACT

The on-going development of micro- and nano-fabrication methods is facilitating interest and investigation into neural probes and implants for use as neurosurgical diagnostic tools and brain-computer interfaces (BCI). Key to the development of all neural probes, from invasive to non-invasive, is the improvement of the spatial resolution of the device while maintaining acceptable temporal sampling rates.

The partially-invasive electrocorticogram (ECoG) is one such neural probe technology that has been advanced significantly in recent years and is currently a top performer when applied in BCI applications due to its high bandwidth and the lack of any acute glial immune response to its presence. The electrodes of flexible micro-ECoG ( $\mu$ ECoG) probes have been reduced in diameter from 3 mm to tens of microns and have had the number of recording sites increased from 16 to 256. But, will the continued reduction in electrode size using current fabrication methods and materials limit/prevent contact from being made between the electrode surface and the cortical tissue and thereby affect the signal quality negatively?

This thesis serves as a preliminary exploration into this problem through mechanical deflection testing of microfabricated flexible  $\mu$ ECoG probe arrays with 20 and 30  $\mu$ m electrodes that have been electrochemically modified to obtain various interface depths and comparing the results to a simple mathematical equation used to model static deflection in discs. This is the first time, to my knowledge, that electrode-tissue contact being lost at some point due to physical and geometrical restraining factors has been brought to light as an issue and been given any specific consideration as to what performance limitations might arise, and to also explore some possible solutions. I found that for a flexible MEA with an insulating Parylene-C layer around 2  $\mu$ m thick, contact could not be established during pressure-induced deflection tests of either of the as-made, unmodified 20 and 30  $\mu$ m diameter electrodes. However, by electrodepositing additional electrode material, PEDOT<sup>+</sup>|ClO<sub>4</sub><sup>-</sup> and gold, I demonstrate that these void spaces can

be effectively filled, thereby enabling electrode-tissue contact once again and obtaining maximum signal strength. The use of a simple equation calculating the magnitude of deflection at the centre of a circular disc can predict whether electrode-electrode contact will be made during deflection test done by applying pressure onto the flexible probes to complete a circuit, indicating contact being made. This model proved to be imperfect and inaccurate but the points lined up well with a curve that had physical parameters that didn't match reality. It is possible that this method could be refined significantly to serve as a more accurate predictor.

The exploration and investigation into the human brain is one of the most important and thrilling scientific tasks humankind knows of and it may also be the most interdisciplinary project at the global scale to have ever been attempted, but with that many people and that much time and energy being poured into this expedition and the never-ending ethical dilemmas and hurdles of human testing that have to be overcome, all the data that gets collected needs to be the rawest, strongest and highest-fidelity data possible or it could prevent or limit analysis and interpretation.

By making the neural probe community aware of this design consideration and by taking steps to avoid limitations that change the fundamental signal capture mechanisms involving electrode-tissue contact, it should be possible to further reduce the diameter of electrodes in flexible  $\mu$ ECOG neural probes while maintaining a high signal. With a neural probe containing a high-resolution multi-electrode array (MEA) that provides a clean, stable array of signals over a reasonable area, computer algorithms can be applied in numerous ways. Once an interface for communication directly with computer systems is established, it is possible for software to learn to recognise more complex patterns through higher resolution inputs and execute tasks such as: fine movement control of robotic prostheses and systems; actively stimulating a region to mimic a catalogued pattern to prevent/lessen neurological episodes such as seizures; or for treating or mediating degenerative and other neurological diseases in ways yet unknown.

# PREFACE

This project began to be an undertaking of mine when I became obsessed with the brain - the enigmatic cognitive power it has *within* and the complete loss of control over our body's movement or the altered perception of our senses *without* (even the loss of our own existence).

Unsatisfied with the answers I was looking for I decided to enter into the field of neuroscience in the fastest way that I could, which was as a material's engineer with limited microfabrication skills, and contribute in some way.

I set out upon the task of designing and fabricating a probe comparable to the state-of-the-art with the intention that it could eventually be tested on an animal or human test subject. To be of some clinical use to neuroscientists, I had to work across several disciplines and make the occasional intuitive leap. As a result, my understanding of these peripheral sciences grew much more throughout this project than I had foolishly expected.

This document is my summary of the knowledge and experience gained while working to complete my objective and make my best contribution to the field possible, however significant. Similarly, I hope to contribute in some way to your knowledge or understanding of the brain, the state-of-the-art probes being used to explore the brain's functions and expand our knowledge of our selves.

Enjoy.

This thesis is an original work by Josh Cunningham.

No part of this thesis has been previously published.

## DEDICATION

I dedicate this thesis work to my family: my parents, my grandparents, my brothers, my sister, my aunts, my uncles, my cousins and all the other family members who have loved and supported me. I would also like to dedicate this to my amazing friends who supported me throughout this thesis project.

I could not have brought this project to fruition without you all in my life - every single one of you!

Thank you all so much.

My love for you all cannot be expressed with words.

## ACKNOWLEDGEMENTS

I would like to distinctly acknowledge and sincerely thank my primary supervisor Dr. Anastasia Elias for consistently providing me with direction in my experiments, for continuing my funding with her own NSERC when my initial funding ran out and for supporting me throughout my numerous struggles, both academic and personal, so that I could bring this project to completion. Thank you so much for your mentorship and guidance over the past years.

I would also like to acknowledge and thank my co-supervisor Dr. Carlo Montemagno of Ingenuity Lab for providing experimental direction, feedback, my initial funding, work space and for opening communication channels with Neuralynx, enabling me to be able to test out their products, and with Dr. Ballanyi, enabling me to test my devices *in vitro* with *ex vivo* tissue.

Thank you Neuralynx for supplying Ingenuity Lab with a sample flexible,  $\mu$ ECoG probe system (including 2 flexible probe front-ends, a spring-pin-based back-end device connector and the requisite adapters and cabling for the 'Nano-Z' active device controller) for me to practice using experimentally and thereby obtain a strong understanding of the system requirements.

Additionally, I want to thank all of my colleagues/summer students/WISER students in Dr. Elias' Research Group. It was sincerely a pleasure working with you all and getting to be a member of a group of passionate scientists. Some sort of special acknowledgement should also go to Caitlin Guzzo, the most cheerful, scientifically investigative, motivating and bow-wearing summer-student I have had the pleasure of supervising thus far. I'd also like to acknowledge and thank all my friends, fellows and colleagues from the Ingenuity Lab and the Department of Chemical and Materials Engineering.

Very special thanks to Dr. Stojan Djokic for his electrochemical guidance and the many insights that he provided me with throughout our numerous

conversations on subjects varying from ‘electrochemistry problems I needed some help with’ to ‘great stories about Nikola Tesla in his childhood’.

A special thank you to Dr. Thomas Thundat and his research group members for organizing periods of time when I could borrow their Gamry potentiostat system for my electrochemical experiments. And another thank you to Richard Hull for getting the ZIF-clip wire connections soldered very nicely by an expert at Digi-Key Electronics on my behalf.

Finally, I want to acknowledge and say thank you to Dr. Klaus Ballanyi and his research group for providing me with space, instructing me, and allowing me to use the electrophysiological recording equipment after performing the animal dissections on my behalf and providing me with living tissue samples of neonatal rat brain slices with various functional nuclei to try and measure. Vladimir Rancic and Bijal Rawal, thank you so much for your assistance and patience.

# TABLE OF CONTENTS

Abstract .....	ii
Preface .....	iv
Dedication .....	v
Acknowledgements .....	vi
Table of Contents.....	viii
List of Figures .....	xiv
List of Tables .....	xxii
List of Equations .....	xxiv
Definition of Symbols.....	xxv
Glossary of Abbreviated Terms .....	xxvi
Chapter 1 - Introduction to Brain-Computer Interfacing.....	0
1.1 - The Investigation of Neural Processes.....	1
1.2 - Thesis Statement .....	5
1.3 - Experimental Plan.....	6
Chapter 2 - The Brain's Structures and Functions, Neuronal Signals and Brain-Computer Interfacing .....	9
2.1 - Introduction to the Brain and Neural Probes.....	10
2.2 - Functional Neural Anatomy .....	11
2.2.1 The Brainstem .....	14
2.2.2 The Cerebellum .....	14
2.2.3 The Diencephalon .....	14
2.2.4 The Cerebral Cortex .....	15
2.2.5 The Ventricular System .....	16
2.3 - Neural Histology and Functionality .....	17
2.3.1 Microstructural Cellular Organization.....	19
2.4 - Modes of Investigating Neuronal Signalling .....	21
2.4.1 Top-Down Investigative Modes .....	21
2.4.2 Bottom-Up Investigative Modes .....	24
2.4.3 Neuronal Signalling Mechanisms .....	25
2.4.3.1 Action Potentials.....	26
2.4.3.2 Local Electrical Field Potentials .....	27
2.5 - Implantable Brain-Computer Interfaces .....	29

2.5.1 Highly-Invasive Implantable BCIs .....	29
2.5.1.1 Microwire Electrodes, Tetrodes and Microwire Electrode Arrays ..	30
2.5.1.2 Planar Silicon Multi-Electrode Shanks and Arrays .....	31
2.5.2 Partially-Invasive Implantable BCIs.....	32
2.5.2.1 Electrocorticographic Multi Electrode Arrays.....	33
Chapter 3 - Design and Fabrication of a Micro-Electrocorticographic Neural Probe System .....	37
3.1 - Introduction to Neural Probe Design and Fabrication.....	38
3.2 - Neural Probe System Design: Device Concepts and Objectives .....	40
3.2.1 $\mu$ ECoG Passive Neural Probe Systems .....	42
3.2.2 Front-End $\mu$ ECoG Probe Device .....	43
3.2.3 Back-End ZIF Connector Device .....	44
3.2.4 Front-End $\mu$ ECoG Probe Design Schematic .....	45
3.2.5 Front-End to Back-End Connection .....	47
3.2.6 ZIF Connector Hard-Shell Case Design .....	49
3.3 - $\mu$ ECoG Front-End Microelectrode Array Layouts.....	51
3.3.1 Concepts Behind the Two MEA Layouts .....	51
3.3.2 Physiological Layout 1 - High Density .....	52
3.3.3 Physiological Layout 2 - Medium Density .....	54
3.4 - Thin-Film $\mu$ ECoG Probe Micro-Fabrication Materials and Methods .....	56
3.4.1 The nanoFAB Microfabrication Facility .....	56
3.4.2 $\mu$ ECoG Photomask Fabrication .....	57
3.4.3 Materials and Suppliers List .....	59
3.4.4 $\mu$ ECoG Device Fabrication Process Flow .....	61
3.5 - ZIF Connector Device Fabrication and Assembly .....	69
3.5.1 Prototyping a Back-End Hard-Shell Case.....	69
3.5.2 Pre-Assembly Processes: ZIF Connector .....	72
3.5.3 Back-End ZIF Connector Device Assembly .....	73
3.6 - Device Inspection and Characterization .....	75
3.6.1 Microfabricated Device Fabrication Process Quality Characterization .	75
3.6.1.1 Mid-Process Visual Inspection .....	76
3.6.1.2 Deposited Parylene-C Layer Thicknesses .....	77
3.6.1.3 Parylene-C Etch Rate Determination .....	78

3.6.1.4 Physical Vapor Deposition of the Au-Ti Conducting Circuitry Layers .....	79
3.6.1.5 Thin-Film Metallic Layer Resistivity .....	79
3.6.1.6 Prototype ZIF Connector Device Electrical Resistance Tests .....	81
3.6.1.7 Fabrication Yields for Thin-Film $\mu$ ECoG Devices .....	82
3.7 - Summary of Design and Fabrication .....	83
Chapter 4 - Electrochemical Modification of Thin-Film $\mu$ ECoG Electrodes .....	87
4.1 - Introduction to Neural Electrochemistry .....	88
4.2 - Biocompatible Electrode Materials .....	89
4.2.1 The Discovery and Development of PEDOT .....	90
4.3 - Experimentally Used Electrode Materials .....	91
4.3.1 Sputtered Gold and Electrochemically Deposited Gold Electrodes .....	91
4.3.2 Electrodes Electro-Polymerized with Poly(3,4-ethylenedioxythiophene) .....	92
4.4 - Electrochemical Apparatus and Materials .....	94
4.4.1 Electrochemical Instrumentation .....	95
4.4.2 Experimental Materials and Suppliers List .....	96
4.4.3 Electrochemical Apparatus .....	97
4.4.3.1 Electrochemical Cell Container .....	97
4.4.3.2 Inert Gas Supply .....	98
4.4.3.3 Magnetically Forced Convection .....	98
4.4.3.4 Electromagnetic Shielding .....	99
4.5 - Electrochemical Deposition Processes and Electrolytes .....	99
4.5.1 Electrochemical Deposition Methods .....	100
4.5.2 Electrolyte Solutions .....	100
4.5.3 Preparing the Electrochemical Cell .....	100
4.6 - Gold Adhesion Layer Modification Deposition .....	101
4.6.1 Adhesive Gold Modification .....	102
4.7 - Constant-Current PEDOT Modifications .....	102
4.7.1 Thin PEDOT Modification P1 .....	103
4.7.2 Thick PEDOT Modification P2 .....	103
4.8 - Resulting Electrode Modifications .....	104
4.8.1 Average P1 and P2 Layer Thicknesses: .....	105
4.9 - Visual Inspection of Microelectrode Surfaces .....	106

4.9.1 As-Made Microelectrodes (AM) .....	106
4.9.2 Gold Modified Electrodes (GM).....	107
4.9.3 PEDOT Modification 1 on As-Made Microelectrodes (AMP1).....	108
4.9.4 PEDOT Modification 2 on As-Made Microelectrodes (AMP2).....	109
4.9.5 PEDOT Modification 1 on Gold Modified Microelectrodes (GMP1).....	110
4.9.6 PEDOT Modification 2 on Gold Modified Microelectrodes (GMP2).....	111
4.10 - <i>In Vitro</i> Electrochemical Impedance Spectroscopy (EIS) Characterization Methods and Results.....	112
4.10.1 Bode-Plot Results from <i>In Vitro</i> EIS Testing of Microelectrodes .....	113
4.11 - Summary of Work .....	119
Chapter 5 - Deflection Modeling and Testing of Modified and Unmodified $\mu$ ECoG Electrodes.....	121
5.1 - Introduction.....	122
5.2 - Atomic Force Microscopy Microelectrode Surface Characterizations.....	128
5.2.1 Cross-Sectional Microelectrode Profile Depths .....	129
5.2.2 Histogram Mean Depths From VIA-Wells .....	132
5.2.3 Comparison of Cross-Sectional Profile and Histogram Mean Depths...	135
5.3 - PEDOT Delamination Studies .....	136
5.3.1 Results and Discussion: Modification Layer Thicknesses .....	137
5.3.1.1 Gold Adhesion Layer Thicknesses.....	138
5.3.1.2 PEDOT Layer Thicknesses .....	138
5.3.1.3 Combined Layer Thicknesses .....	139
5.3.2 Materials and Methods: Delamination Testing .....	139
5.3.3 Results and Discussion: Delamination Studies .....	140
5.4 - Deflection Under Pressure .....	142
5.4.1 Materials and Methods: Deflection Tests .....	143
5.4.2 Results and Discussion: Deflection Tests .....	145
5.5 - Mathematical Modeling of Symmetrical Deflection of a Static Disc .....	146
5.5.1 Methods: Physical Modeling Parameters .....	148
5.5.2 Results and Discussion: Modeling Predictions.....	149
5.5.3 Model Predictions Vs. Experimental Results .....	151
5.6 - Summary of Work .....	153
5.6.1 Depth Measurement Methods Using AFM Software: .....	153
5.6.2 Layer Thickness and Adhesion:.....	154

5.6.3 Deflection Testing and Mathematical Modeling: .....	156
Chapter 6 - Summary of Experimental Results, Conclusions and Suggestions for Future Work .....	157
6.1 - Restatement of Thesis.....	158
6.2 - Experimental Results and Discussion .....	159
6.2.1 Thin-Film $\mu$ ECoG Probe System Design Objectives .....	159
6.2.1.1 $\mu$ ECoG Design Objective Summaries .....	159
6.2.1.2 ZIF-Connector Design Objective Summaries .....	161
6.2.2 Electrochemical Modification and <i>In Vitro</i> EIS of $\mu$ ECoG Microelectrodes .....	162
6.2.2.1 Electrochemical Microelectrode Modifications .....	162
6.2.2.2 Visual Inspection of Electrodeposited Layers .....	163
6.2.2.3 In Vitro Electrochemical Impedance Spectroscopy (EIS) Testing .	164
6.2.3 Physical Characterization of Microelectrode Interfaces, Mathematical Deflection Modeling and Pressure-Based Probe Deflection Testing .....	165
6.2.3.1 Physical Characterization of Microelectrode Interfaces: PEDOT Layer thickness .....	165
6.2.3.2 Physical Characterization of Microelectrode Interfaces: PEDOT Layer adhesion.....	166
6.2.3.2 Mathematical Probe Deflection Modeling .....	166
6.2.3.3 Probe Deflection Tests Under Pressure .....	167
6.3 - Conclusions and Suggestions for Future Work.....	167
6.3.1 Design Improvements.....	167
6.3.2 Fabrication Changes .....	168
6.3.3 Electrochemical Modification and Characterization .....	168
6.3.4 Deflection Modeling and Tests .....	168
6.3.5 Adhesion/Delamination Tests .....	169
6.3.6 Tests within an Animal Model .....	169
6.4 - Closing Remarks .....	170
References.....	172
Appendix A - Fabrication and Characterization Methods for $\mu$ ECoG Devices ..	189
A.1 - $\mu$ ECoG Device Fabrication Methods.....	190
A.1.1 Chemical Vapour Deposition / Polymerization of Parylene-C: .....	190
A.1.2 Reactive Ion Etching with O <sub>2</sub> Plasma:.....	191
A.1.3 Optical Lithography:.....	191

A.1.4 Physical Vapour Deposition: .....	193
A.2 - Methods of Device Characterization.....	194
A.2.1 Surface Contact Profilometry .....	194
A.2.2 Optical Microscopy.....	195
A.2.3 Four-Point Probe .....	195
Appendix B - Supplemental Electrochemistry Background .....	196
B.1 - Basics of Three-Electrode Cells .....	197
B.2 - Working Electrodes .....	198
B.3 - Counter Electrodes.....	198
B.4 - Reference Electrodes .....	200
B.4.1 Silver-Silver Chloride RE (Aqueous): .....	200
B.4.2 Silver-Silver Ion RE (Non-Aqueous): .....	201
B.5 - Storage of Reference Electrodes.....	202

# LIST OF FIGURES

- Figure 1** - Cross-section depicting two VIA-wells (highlighted within dashed red boxes) exposing circular, gold microelectrodes to neural tissue. The truncated sections of identical purple circles, (representing the tissue at its mechanical limit), reach distinctly different depths into the VIA-wells, preventing direct tissue contact with the smaller diameter electrode (on the left). .....4
- Figure 2** - An artificially coloured midsagittal section of the human brain showing the medial surface of the left cerebral hemisphere. Yellow: brainstem; Red: cerebellum; Green: diencephalon; Blue: ventricles/other intracerebral components; Pink: corpus callosum; Purple: cerebral cortex (Black: approximate parcellation lines). (Labels of cortical lobes: O - Occipital, P - Parietal, L - Limbic, F - Frontal, T - Temporal) ..... 13
- Figure 3** - Drawings of a few Purkinje neurons from the cerebellum (left) and a small section of networked pyramidal neurons from the cerebral cortex (right) done and first published in "Comparitive study of the areas of the human cortex" (1899) by Santiago Ramón y Cajal. .... 18
- Figure 4** - Another Ramón y Cajal sketch from "Comparitive study of the areas of the human cortex" showing a comparison of the highly organized pyramidal neurons and other neurons as arranged in tissue from various sensory areas of the neo-cortex. .... 20
- Figure 5** - Example neuronal action potential. Initially at -70 mV, then +110 mV in 1 ms, then -110 mV in 0.4 ms, then -40 mV in 0.8 ms, then +40 in 1.5 ms and ready to fire again.<sup>42</sup> ..... 26
- Figure 6** - Silicon based penetrating neural probes. (Michigan style probe on the left<sup>52</sup> - Utah style probe on the right<sup>53</sup>)..... 31

**Figure 7** - Cervello® Elite EcoG with an 8 x 8 array of 3 mm Pt electrodes.<sup>64</sup> . 34

**Figure 8** - A state-of-the-art microfabricated flexible,  $\mu$ ECoG array with 360 actively multiplexed  $300 \times 300 \mu\text{m}^2$  Pt electrodes on the left and the probe array in use on a visual cortex on the right.<sup>68</sup> ..... 35

**Figure 9** - A diagram showing the fabricated devices along the signal processing chain. .... 42

**Figure 10** - A schematic diagram of the  $\mu$ ECoG probe device. From left to right: a magnification of the probe head and neck, then the macroscopic device view showing the probe body, the device ID and finally the legs and connector pads of the ZIF tail (which has been reinforced and thickened with Kapton tape)..... 45

**Figure 11** - Enlarged view of the “neck” and its trace-pitch step-down pattern (pitches to probe head are:  $70 \mu\text{m} > 20 \mu\text{m} > 5 \mu\text{m}$ )..... 45

**Figure 12** - CAD image of the ZIF tail, the ‘Legs’ step-up zone, device ID ‘A’, and 18 connector pads ( $0.7 \times 3.0 \text{ mm}$ , 1 mm pitch). .... 46

**Figure 13** - Conceptual schematic diagram for the electrical connection between the probe and the wires of the back-end. .... 48

**Figure 14** - 2D AutoCAD schematic of a two-piece protective, hard-shell case for the ZIF-connector..... 50

**Figure 15** - Optical micrograph of a horizontal brain slice excised from an actual neo-natal rat. Enclosed within the yellow boundary is the functional neural nucleus of interest: the *LC*. (Image provided by Vladimir Rancic of Dr. Ballanyi’s Lab.) ..... 52

**Figure 16** - CAD design for Physiological Layout 1, the “high-density” electrode layout. Blue is insulated metal; purple regions represent the bare metal of the microelectrodes that is not insulated. (Units are in  $\mu\text{m}$ ) ..... 53

**Figure 17** - One of the neural structures of interest in neo-natal rat brain slices: the VMH. (Image provided by Vladimir Rancic of Dr. Ballanyi’s Lab.) ..... 54

**Figure 18** - Physiological Layout 2, the “medium-density” electrode layout. (Units are in  $\mu\text{m}$ ) ..... 55

**Figure 19** - Metal pattern layer (Mask #1: left, blue); Insulated VIA-well etching layer (Mask #2: centre, red); And the combined layer stack (right, red/blue)..... 58

**Figure 20** - Alignment marks (repeated at various sizes) are used to accurately align Mask #2 (centre) with the metallic pattern from Mask #1 (left). Mask #1 & Mask #2 properly aligned (right). ..... 58

**Figure 21** - AutoCAD 3D Rendering of the bottom-half (red) and top-half (blue) of the hard-shell/protective-case. .... 70

**Figure 22** - The connector housing CAD layout showing a 3D model of the top and bottom halves along with necessary utility-discs, visually indicating the MakerBot® 3D printer’s input data, on a 1 cm x 1 cm grid that represents the physical printing area available..... 71

**Figure 23** - An early prototype ZIF connector hard-shell case with a dime for scale. .... 71

**Figure 24** - The wired ZIF-clip, freshly encapsulated with epoxy (L) and the same connector 24 to 48h later being prepared for placement into the 3D printed housing (R). .... 72

**Figure 25** - On the left, the wired ZIF secured to the topside of the housing’s bottom-half. On the right, a perspective angle photo of the same bottom half along with its counterpart with a dime included for scale. .... 73

**Figure 26** - An EMR noise resistant ZIF connector device - fully assembled and ready for experimental use..... 74

**Figure 27** - Photos post lithography patterning process showing good (right) and bad (left) development. .... 76

**Figure 28** - Optical micrographs post-fabrication of batch 1 (left) and batch 2 (right). Each row represents a wafer (labelled ‘W#’) and each column represents a device on the wafer (labelled as ‘A, B, C, D, or E’). .... 82

**Figure 29** - Batch 2: 94.4% Fabrication Yield Represented Numerically and Visually. .... 83

**Figure 30** - Phys. Layout 1: High-Density (L) and Phys. Layout 2: Medium Density (R). .... 84

**Figure 31** - Fully fabricated neural probe device, approximately to scale. .... 84

**Figure 32** - Images of a  $\mu$ ECoG Probe mounted into a ZIF-Connector device taken from two different angles (dimes for scale)..... 85

**Figure 33** - Fully assembled and labelled back-end ZIF-connector device. .... 85

**Figure 34** - The molecular structure of an EDOT monomer (LEFT) and a 5-mer PEDOT<sup>+</sup> chain with a representative counter ion A<sup>-</sup> (RIGHT).<sup>91</sup> .... 90

**Figure 35** - The electrochemical cell within the Faraday cage. Apparatus components not shown: Gamry Reference 3000, N<sub>2</sub> gas blanketing tube and stir bar..... 99

**Figure 36** - 'As-Made' gold microelectrodes at 1500x magnification. (Left: 20  $\mu\text{m}$  diameter; Right: 30  $\mu\text{m}$  diameter) ..... 106

**Figure 37** - 'Gold-Modified' rough-gold microelectrodes at 1500x magnification. (Left: 20  $\mu\text{m}$  diameter; Right: 30  $\mu\text{m}$  diameter) ..... 107

**Figure 38** - 'As-Made' & PEDOT Modification 1 microelectrodes at 1500x magnification. (Left: 20  $\mu\text{m}$  diameter; Right: 30  $\mu\text{m}$  diameter) ..... 108

**Figure 39** - 'As-Made' & PEDOT Modification 2 (AMP2) microelectrodes at 1500x magnification. (Left: 20  $\mu\text{m}$  diameter; Right: 30  $\mu\text{m}$  diameter) ..... 109

**Figure 40** - Gold Modified & PEDOT Modification 1 microelectrodes at 1500x magnification. (Left: 20  $\mu\text{m}$  diameter; Right: 30  $\mu\text{m}$  diameter) ..... 110

**Figure 41** - Gold-Modified & PEDOT Modification 2 microelectrodes at 1500x magnification (Left: 20  $\mu\text{m}$  diameter; Right: 30  $\mu\text{m}$  diameter) ..... 111

**Figure 42** - Average impedance and phase angle vs. frequency curves for each modification type from the 'N' single-test measurements of individual 20  $\mu\text{m}$  electrodes of that type. Error bars represent standard deviation within the sample set..... 114

**Figure 43** - Average impedance and phase angle vs. frequency curves for each modification type from the 'N' single-test measurements of individual 30  $\mu\text{m}$  electrodes of that type. Error bars represent standard deviation within the sample set. (0.1 to 100,000 Hz at 10  $\text{mV}_{\text{RMS}}$  AC in 1M PBS at room temperature in low noise mode) ..... 115

**Figure 44** - An illustration qualitatively demonstrating the existence of "limiting dimensions" for VIA-wells in  $\mu\text{ECoG}$  probes. Shown are two identical purple circles trying to make contact with the two gold microelectrodes at the bottoms of their respective VIA-wells. The smaller

diameter VIA-well has prevented direct contact while one twice its diameter has allowed it.....	123
<b>Figure 45</b> - Cross-sectional VIA-well profiles of a 30 $\mu\text{m}$ 'As-Made' electrode (AM) obtained through AFM.....	129
<b>Figure 46</b> - Cross-sectional VIA-well profiles of a 30 $\mu\text{m}$ 'Gold-Modified' electrode (GM) obtained through AFM. ....	129
<b>Figure 47</b> - Cross-sectional VIA-well profiles for a 30 $\mu\text{m}$ AM electrode with a thin PEDOT coating (AMP1) obtained through AFM.....	130
<b>Figure 48</b> - Cross-sectional VIA-well profiles of a 30 $\mu\text{m}$ AM electrode modified with a thick PEDOT coating (AMP2) obtained through AFM. ....	130
<b>Figure 49</b> - Cross-sectional VIA-well profiles of a 20 $\mu\text{m}$ GM microelectrode coated with an additional thin layer of PEDOT (GMP1) obtained through AFM.....	131
<b>Figure 50</b> - Cross-sectional VIA-well profiles of the electrode modification with the most material deposited, GM and thick PEDOT (GMP2) obtained through AFM. Red, green and blue markers placed at electrode surface peaks (i.e. points of minimal depth) measuring 0.184, 0.503 and 0.051 $\mu\text{m}$ while the maximum depth was measured to be 0.940 $\mu\text{m}$ . ....	131
<b>Figure 51</b> - Visualization from the height sensor AFM data within a 75 $\mu\text{m}$ by 75 $\mu\text{m}$ scan area; showing 4 electrodes surrounded by a P-C matrix with interfaces at varying depths, as darker areas are relatively deeper than brighter areas. ....	133
<b>Figure 52</b> - Histograms of the AFM image's pixel-population showing two distinct population sets. The relative separation between population-means is considered as the interface depth. (e.g. 'As-Made' interface depth of 1.828 $\mu\text{m}$ ) .....	133

**Figure 53** - 1500x magnification micrographs of a  $\mu$ ECoG probe head before (left) and after delamination tape-tests (right). ..... 141

**Figure 54** - An illustration of the pressure-induced deflection testing apparatus. .... 143

**Figure 55** - Schematic Model for the Static-Disk Symmetrical Deflection Equation.<sup>137</sup> ..... 148

**Figure 56** - Magnitudes of deflection at various pressures for a 2  $\mu$ m (dashed lines) and a 25  $\mu$ m (solid lines) thick P-C base layer. .... 150

**Figure 57** - Estimated pressure required for the necessary deflection magnitude (solid = 2  $\mu$ m, dashed = 0.5  $\mu$ m) for 2, 5, 10, 20, 25  $\mu$ m thick base layers of P-C  $\mu$ ECoG probes. .... 151

**Figure 58** - Predicted pressure required for the deflection model compared to the experimental results of the deflection test: (20  $\mu$ m, 1250 kPa), (30  $\mu$ m, 125 kPa) - marked with X's. .... 152

**Figure 59** - Outer Left (OL): 20  $\mu$ m AM, Inner Left (IL): 30  $\mu$ m AM; Inner Right (IR): 20  $\mu$ m GM, Outer Right (OR): 30  $\mu$ m GM..... 163

**Figure 60** - OL: 20  $\mu$ m AMP1, IL: 30  $\mu$ m AMP1; IR: 20  $\mu$ m GMP1, OR: 30  $\mu$ m GMP1..... 163

**Figure 61** - OL: 20  $\mu$ m AMP2, IL: 30  $\mu$ m AMP2; IR: 20  $\mu$ m GMP2, OR: 30  $\mu$ m GMP2..... 163

**Figure 62** - Parylene-C (P-C) monomer molecular model. .... 190

**Figure 63** - An illustrative schematic showing a developed photoresist layer which, due to the IR processing performed, now exhibits a slightly undercut sidewall that is ideal for lift-off patterning..... 192

**Figure 64** - An illustrative schematic of contact profilometry. .... 194

**Figure 65** - Illustrated schematic of a 4-point probe tip above a Si test substrate. .... 195

**Figure 66** - An illustrated the three-electrode cell with an X-shaped Teflon®-coated magnetic stir bar at the bottom of the cell container, a green capped WE on the left, a Red capped CE on the right and a white capped RE resting diagonally. .... 197

**Figure 67** - Magnified illustration of the three-electrodes (WE, RE, CE from L to R) shown in Figure 76 visually showing the solution resistance ( $R_S$ ) removed from any potential measurements and the reduced RE solution resistance ( $R_{RE}$ ). .... 198

**Figure 68** - A properly stored non-aqueous Ag|Ag<sup>+</sup> RE being kept in a storage container filled to an adequate level with the appropriate storage solution. (0.01 M LiClO<sub>4</sub> in ACN). .... 202

# LIST OF TABLES

<b>Table 1</b> - Example Electroencephalogram Brain Rhythm Bands .....	23
<b>Table 2</b> - Step-by-Step Fabrication Process Flow Summary with X-Sectional Schematics .....	68
<b>Table 3</b> - Material Legend for the Fabrication Process .....	68
<b>Table 4</b> - Average Parylene-C Deposition Layer Thickness .....	77
<b>Table 5</b> - Parylene-C O <sub>2</sub> Etch Rates as Calculated .....	78
<b>Table 6</b> - Average Thicknesses of Sputtered Au-Ti Metallic Layer .....	79
<b>Table 7</b> - Batch 1 and 2 Au-Ti Metallic Layer Resistivity .....	80
<b>Table 8</b> - Averaged Resistivity of the Au-Ti Metallic Layers.....	81
<b>Table 9</b> - Microelectrode Modification ID Codes .....	104
<b>Table 10</b> - Impedance and Phase Angle Values for the Various Sizes and Types of Electrode at a Selection of Relevant Frequencies .....	118
<b>Table 11</b> - Microelectrode Modification (Mod.) Status ID Codes.....	125
<b>Table 12</b> - Cross-Sectional Profile Electrode Interface Depth Averages .....	132
<b>Table 13</b> - Average Mean Interface Depth for Each Microelectrode Type .....	134
<b>Table 14</b> - Summarized Electrode Interface Depth Data Showing Both AFM-Based Analysis Results and the Calculated Average of the Two Methods..	135
<b>Table 15</b> - Electrochemically Deposited Layer Thickness Approximations From Calculations Based on the Average of the AFM Methods Used to Measure Depth .....	137

**Table 16** - Deflection Test Calculated Mass Requirements..... 144

**Table 17** - Results From Deflection Under Pressure Testing of Flexible  $\mu$ ECoG Probes ..... 145

**Table 18** - Physical Modeling Parameters for Parylene-C Thin-Film Devices .. 148

## LIST OF EQUATIONS

### Equation 5.1 -

Electrodeposited Layer Thickness:

$$t_{layer} = d_{initial} - d_{final}$$

### Equation 5.2 -

Deflection Magnitude in a Symmetrical Static Disc:

$$\delta = \frac{3}{4}(1 - \nu^2) \frac{\Delta P \cdot R^4}{E \cdot t^3}$$

### Equation 5.3 -

Pressure Differential Required for Achieving a Specific Deflection Magnitude in a Symmetrical Static Disc:

$$\Delta P = \frac{4 \cdot \delta (E \cdot t^3)}{3(1 - \nu^2)R^4}$$

### Equation B.1 -

Standard Hydrogen Reduction Reaction Potential:



### Equation B.2 -

Standard Silver - Silver Chloride Reduction Reaction Potential:



### Equation B.3 -

Standard Silver - Silver Ion Reduction Reaction Potential:



# DEFINITION OF SYMBOLS

$t_{\text{layer}}$	Electrode Layer Thickness
$d_{\text{initial}}$	Initial Electrode Interface Depth
$d_{\text{final}}$	Final Electrode Interface Depth
$\delta$	Deflection Magnitude
$\nu$	Poisson's Ratio
$\Delta P$	Applied Pressure Differential
$R$	Radius of a Symmetrical Disc
$E$	Young's Modulus
$t$	Thickness of a Symmetrical Disc
Ag	Silver
Au	Gold
$H_2$	Hydrogen Gas
Ti	Titanium
$E^{\circ}$	Standard Reduction Reaction Potential
$V$	Electrical Potential/Voltage
$I$	Electrical Current/Amperage
$R$	Circuit Resistance/Ohmage

# GLOSSARY OF ABBREVIATED TERMS

ACN	Acetonitrile
AD	Analog-to-Digital
AFM	Atomic Force Microscopy
AM	As-Made Electrode Surface
AMP1	As-Made with PEDOT 1
AMP2	As-Made with PEDOT 2
AP	Action Potential
BBB	Blood-Brain Barrier
BCI	Brain-Computer Interface
BOLD	Blood-Oxygen Level Dependent
CA <sub>3</sub>	Hippocampal Neuronal Cluster
CAD	Computer Aided Design
CE	Counter/Auxiliary Electrode
CNT	Carbon Nanotube
CVD	Chemical Vapour Deposition
DAS	Data Acquisition System
DI	Distilled Water
EC	Entorhinal Cortex
ECM	Extracellular Matrix
ECoG	Electrocorticogram
EDOT	3,4-ethylenedioxythiophene
EEG	Electroencephalogram
EIS	Electrochemical Impedance Spectroscopy
EMF	Electromotive Force
ESA	Electrochemical Surface Area
FC	Faraday Cage
FDA	U.S. Food and Drug Administration
fMRI	Functional Magnetic Resonance Imaging
GM	Gold Modified Adhesion Electrode Surface
GMP1	Gold Modified with PEDOT 1
GMP2	Gold Modified with PEDOT 2
GSA	Geometrical Surface Area
HSA	High Surface Area
HPF	High-Pass Filter
IC	Integrated Circuit
ICP	Intrinsically Conductive Polymer
IPA	Isopropyl Alcohol
LC	<i>Locus Coeruleus</i>

LFP	Local Electrical Field Potential
LPF	Low-Pass Filter
MRI	Magnetic Resonance Imaging
NHE	Normal Hydrogen Electrode
OCP	Open Circuit Potential
PBS	Phosphate Buffered Saline
P-C	Parylene-C
PEDOT	Poly(3,4-ethylenedioxythiophene)
PLLA	Poly(L-Lactic acid)
PVD	Physical Vapour Deposition
PVP	Poly(vinylpyrrolidone)
RE	Reference Electrode
RIE	Reactive Ion Etching
RMS	Root-Mean Square
RPM	Revolutions Per Minute
SHE	Standard Hydrogen Electrode
SOP	Standard Operating Procedure
$\mu$ ECOG	Micro-electrocorticogram
VIA	Vertically Integrated Access
VMH	<i>Ventro-Medial Hypothalamus</i>
WE	Working Electrode
ZIF	Zero Insertion Force

---

# **CHAPTER 1 - INTRODUCTION TO BRAIN-** **COMPUTER INTERFACING**

---

# 1.1 - THE INVESTIGATION OF NEURAL PROCESSES

The brain is the most mysterious organ in the human body. Besides housing the mind, with which we consciously perceive and experience our existence, it is also the sub-conscious command-center on which the rest of the body completely depends. Despite the fact that researchers have been trying to scientifically understand the specific mechanisms of cognition within the brain for several centuries now, they know little more than the fact that it does what it does with mysteriously generated cascades of electrical and chemical signals constantly cycling around hundreds of billions of nerve cells, interconnected in a seemingly impossibly-complex three-dimensional network running throughout the entire body (the central nervous system (CNS)).<sup>1-3</sup> A full and complete understanding of the electrochemical mechanisms of conscious and unconscious cognition within the CNS may very well be impossible to accomplish. However, like so many other seemingly-impossible human endeavours, it is a task so awesome and challenging, with such promise of understanding and intellectual growth as a species, that humankind will continue in spite of the odds to figure it out - one step at a time.<sup>4</sup>

Through continued investigation and growth in the fields of *Nanotechnology*, *Cognitive theory*, *Information technology systems* and *Biotechnology*, a crossroads has been reached where the combined efforts and technical expertise of these four main fields (and peripherally related fields), collectively referred to as NCIB, are collaborating in ways that allow researchers to explore past the previous edge into unknown territory and continue expanding the understanding of the enigmatic brain.<sup>4,5</sup> Some of the most exciting products to emerge from the interdisciplinary union of NCIB, and the focus of the experimental technology created for this thesis, are the numerous advanced neural probe implant and prosthetic technologies.<sup>6,7</sup>

With neural probe technologies now capable of recording and/or mimicking the electrical signals of certain neural regions as sampled directly from the CNS, neuroscientists have powerful new research tools for investigating the cognitive mechanisms of the brain being made available at an astounding rate.<sup>8</sup> By combining recent neuroscientific research findings, biocompatible neural implant materials and microprocessor fabrication methods, utilizing the proper electronic hardware and computer software, medical practitioners working with neurologically diseased and disabled patients have new rehabilitative tools in development that have such promising applications that they could change the course of human civilization.<sup>6-9</sup>

With a technological development pattern currently echoing that of the microcomputer processor industry over the past few decades - which successfully pursued the iterative miniaturization and improvement of its electronic components at an exponential rate - advances in neural probe technology are following a similar trend with the continued miniaturization and improved performance of biomedical devices.<sup>4,8,10</sup>

Although many significant advances in neural probe technology have been made, there still remain numerous foreseeable obstacles to their further enhancement that must be overcome before a stable, long-lasting, high-quality brain-computer interface (BCI) can be practically reached. Once proven ethically acceptable and medically safe, these neural probe and BCI implant technologies could transition beyond medical and therapeutic applications into many, many other types of applications, possibly changing the evolution of the human race in ways that have only been dreamt of in science fiction.<sup>11-16</sup>

At this time, being capable of recording signal information with neural probes in which the electrodes are approximately the same size of a nerve cell body, trends in the neural probe development community are mostly shifting towards

enhancing the performance of the probes.<sup>4,8,10,17</sup> Some of these performance enhancement directions include:

- Increasing the number of electrodes (i.e. sampling sites) and electrode density (i.e. spatial resolution or electrode pitch) to acquire higher-resolution data mapping over as much cortical area as possible.<sup>18,19</sup> This includes leveraging advancing fabrication techniques to produce smaller and smaller devices, which can read precisely from smaller and smaller areas;
- Extending the implant lifetime in or on the brain by improving the biocompatibility, to enable safer, more effective, longer-term functional implantations (equal to a human lifetime, ideally);<sup>20</sup>
- And the use of cutting-edge, high-performance, biocompatible electronic materials to improve extracted electrical signal quality and obtain data with the maximum recording fidelity.<sup>21,22</sup>

This thesis work aimed to preliminarily assess a concerning physical limitation that is possibly intrinsic to state-of-the-art thin-film microelectrocorticographic ( $\mu$ ECoG) probe designs, as which becomes more critical as the size of the devices is reduced further and further. This limitation could negatively affect the maximum obtainable signal quality, hindering neuroscientific progress and limiting the effectiveness of  $\mu$ ECoG devices as BCIs. Although my concern will be explained in more detail in Chapter 5, consider here a planar,  $\mu$ ECoG, consisting of a patterned metallic layer containing circular microelectrodes connected by long, thin wires to connector pads sandwiched between two microns-thick layers of flexible substrate material. While the circuitry in the surrounding regions must be insulated from contact with the tissue and brain fluids, the electrically conductive electrode surfaces must be open and exposed to make direct electrical contact with the exterior tissue of the neocortex. Figure 1, on the following page, depicts two cross-sectional

microelectrode openings, Vertically-Integrated-Access-wells (VIA-wells), one with twice the diameter of the other and each with a purple circle (representative of neocortical tissue at its physical limit for mechanically elastic deflection) being placed into the VIA-wells in an attempt to make direct contact with the thin layer of gold at the base of the well. This figure provides a simple, conceptual depiction of the performance limiting VIA-well geometries resulting from the continued reduction of diameter of thin-film  $\mu$ ECoG electrodes, visually demonstrating the eventual loss of contact that is being explored in this thesis.

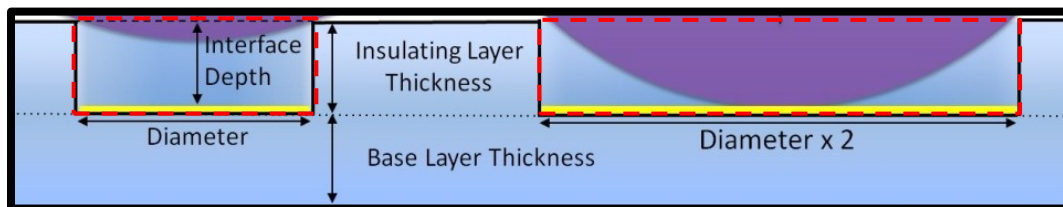


**Figure 1** – Cross-section depicting two VIA-wells (highlighted within dashed red boxes) exposing circular, gold microelectrodes to neural tissue. The truncated sections of identical purple circles, (representing the tissue at its mechanical limit), reach distinctly different depths into the VIA-wells, preventing direct tissue contact with the smaller diameter electrode (on the left).

As is clearly shown, as the microelectrodes of thin-film  $\mu$ ECoG probes are further reduced to smaller diameters, the depth-to-diameter aspect ratio will continue to increase, making it harder and harder for neocortical tissue to deflect to the bottom of the VIA-wells and thereby make direct, ohmic contact with the microelectrode. Past some critical point in the dimensions, although signal detection would continue to occur, any signal detected would have to transmit through a high-impedance ionic channel formed by the fluid-filled VIA-well, attenuating high-frequency signal strength, possibly introducing noise and other signal artefacts and generally reducing the signal fidelity/quality.<sup>23,24</sup> Arguably, without making some adjustments to current thin-film  $\mu$ ECoG probe design and fabrication processes, the quality of signal obtainable through  $\mu$ ECoG technology may not reach its maximum potential.

## 1.2 - THESIS STATEMENT

A fundamental difference has become apparent in the micro-scale probes of today when compared to the mm-scale probes of the previous few decades due to the shift in fabrication methods and the reduced size-scale of new thin-film neural probes.<sup>25</sup> As microelectrode diameters are reduced while the supporting/insulating thin-film material is limited to a minimum required layer thickness to be pinhole free, the electrode diameter to VIA-well depth aspect ratio will eventually inhibit or prevent tissue-electrode contact from being made. Tissue-electrode contact is critical for obtaining the best signal-to-noise ratio (SNR) and therefore the best quality (or most accurate) signal.

In designing a device that will be used for measuring and investigating what is essentially a radically complex, bio-electro-chemical computational system that we understand relatively little about, I believe that acquiring high quality signal data is an essential requirement for effective, meaningful processing and analysis. As I have previously stated, my main concern with these electrode size reductions is that the quality of the recorded signal and therefore the fidelity of the neuronal signalling systems being investigated will suffer from the performance-limiting dimensions of the electrodes themselves by introducing signal artefacts, diminishing the level of high-frequency signal contributions, losing meaningful content that a higher-quality recording would have contained and making the following analyses and interpretations more difficult and possibly futile.

I propose that one solution to this problem is through post-fabrication electrochemical modification of neural probe microelectrodes with additional high-performance electrode material to fill-in the VIA-wells and reduce the electrical impedance simultaneously.

## **1.3 - EXPERIMENTAL PLAN**

To begin to explore this problem, a  $\mu$ ECoG probe that matches state-of-the-art, commercially available probes must be designed based on the physical properties and functional mechanisms of the brain and with knowledge of the safe limits of electrochemical transduction in the brain. Additionally, it must be fabricated using materials that are FDA approved for clinical use and compatible with microprocessor technology fabrication processes.

In this investigation, electrochemical modifications will be performed followed by deflection tests to experimentally explore direct electrode contact at microelectrode diameters of 20 and 30  $\mu\text{m}$  and, with various combinations and quantities of electrochemically deposited electrode material, whether or not that loss can be regained.

The objective of the electrode modifications is the maintenance of the signal-quality obtained using passive, flexible,  $\mu$ ECoG multi-electrode arrays (MEAs) as their circular electrodes are progressively reduced in diameter for enhanced spatial resolution. While it would be possible to immediately jump into the design and fabrication of flexible  $\mu$ ECoG probes, I feel it is important to gain a fundamental understanding of the brain as both a biological system and as an electrochemical system. It seems logical to have a rudimentary understanding of the functionality of neural anatomy, its cellular histology and the signalling mechanisms occurring within the neural network - the actual source of the signals that will eventually be recorded with the neural probe.

So, in Chapter 2, I will be discussing the features of the functional anatomy and cellular structures of the brain along with the cellular signalling mechanisms that are to be recorded. Several types of neural probe systems including non-

invasive and fully-invasive technologies will be discussed with respect to their strengths and weaknesses as BCIs.

In Chapter 3, I go over the details of the considerations, materials and methods used in the design and fabrication processes of the electronic devices used as the passive neural probe system. The design concepts and objectives of the two electronic components: the “front-end” probing device and the “back-end” connecting device and how they interconnect to form a complete neural probe system. The  $\mu$ ECoG design schematics and MEA electrode layouts are detailed followed by descriptions of the fabrication process flow steps for the front-end probe using microfabrication methods. This leaves the fabrication of the back-end connector - the rapid prototyping methods and assembly procedures for the device components. Throughout the fabrication process, investigation into the quality of the fabrication process-steps and the characterization of the various layers and components of devices are carried out to ensure that both the front- and back-end devices are defect-free and functioning properly. Once the neural probe system’s front-end and back-end devices are fabricated and interconnecting to each other properly, the electrochemical testing and modification of the electrodes can begin.

In Chapter 4, I will discuss some of the relevant electrochemistry fundamentals, the details of the electrodeposition procedures used to modify the electrode surfaces and then finally the *in vitro* electrochemical impedance tests performed for each and every electrode size and surface type. Combatting both the loss of direct tissue-contact and the increasing interface impedance associated with reduced electrode area, high-performance bio-electrode materials, such as poly(3,4-ethylenedioxythiophene) (PEDOT) with lithium perchlorate as the counter-ionic salt ( $\text{Li}^+, \text{ClO}_4^-$ ), will be electrochemically deposited onto the microelectrodes to fill in the VIA-wells, effectively reducing the interface depth until deflection limitations no longer

inhibit signal quality. At this point, the probes will have been fabricated and either left un-modified as controls or have been electrochemically modified to try to combat the loss of contact that may occur at the diameters of 20 and 30  $\mu\text{m}$ .

In Chapter 5, I will discuss the use of atomic force microscopy (AFM) methods to measure the depths of the electrode interfaces, enabling average depths for different electrode sizes and modifications. After obtaining the required measurements and taking the required photographs, delamination and deflection tests were performed. One concern with the use of PEDOT as a filler material is that a thick PEDOT deposit may delaminate spontaneously without intervention. To improve the mechanical stability of the PEDOT, an adhesion-enhancing layer of rough gold with high surface area (HSA) will be electrochemically deposited onto as-made gold electrodes before further electrochemical modification with PEDOT. The adhesion tests performed and the results obtained are discussed in this chapter. The deflection tests are based on applying different amounts of pressure onto the backsides of the flexible probes lying face down on a flat sheet of aluminum foil and monitoring the status of the test circuit. Closing the circuit will result in an electrical connection that can be displayed by the multi-meter. A lack of contact is indicated by an "OL". Lastly, I will be going over a mathematical equation that will be used to predict the magnitude of deflection at the centre of the disc - a circular, static-disc deflection equation utilizing the material properties, the dimensions of the disc, and the pressure applied as variables to calculate a peak deflection magnitude at the centre of the disc. I will then explain the outcomes from the models and how effective it was and how useful it was.

In the final chapter, Chapter 6, I will summarize and discuss the outcomes of the experimental work, any conclusions that can be made and provide suggestions for future work.

---

**CHAPTER 2 - THE BRAIN'S STRUCTURES**  
**AND FUNCTIONS, NEURONAL SIGNALS**  
**AND BRAIN-COMPUTER INTERFACING**

---

## **2.1 - INTRODUCTION TO THE BRAIN AND NEURAL PROBES**

The objective of Chapter 2 is to provide a brief summary of background information in each of the relevant neuroscientific fields that have enabled the current state-of-the-art neural probe systems used for investigation into and interaction with the brain. By highlighting the key historical neuroscientific findings from both the macro-scale anatomical perspective and from the cellular-scale structural and organizational perspectives of functional neuroscience, a discipline based in the fundamentals of neuronal signals. Then, by applying current neuroscientific knowledge to the subsequent and ongoing development and design of neural probes, society could further elucidate the mystery of the mind within the brain and maybe one day enable a general theory of cognition to be established.

First, I will examine the functional neural anatomy of the brain as it is currently understood, with emphasis placed on the anatomical components playing most heavily into the development of neural probe technology. Next, I introduce the complex histology of the brain: the cellular diversity, organization and structural arrangement enabling the higher-level functions of cognition and behaviour through basic signalling within the cellular circuitry of the brain.

This is followed by a quick look at the technology that has laid the groundwork for all further study into the brain being done today, such as the methods used to visualize living brains in a completely non-invasive manner, and the corroboration of predictions made about functionality for various macroscopic components that had been made historically.

The non-invasive neural probe technology used to learn about the brain through coarse-grained, low-resolution signals will be discussed. As will, finally, the invasive neural probe technology used at cellular levels to observe fine-grain, highly localized signals. The design limitations of these invasive probes in their current clinical applications and future concept applications as BCIs are also briefly summarized to conclude the chapter.

## **2.2 - FUNCTIONAL NEURAL ANATOMY**

Hidden and protected within the skull's dense bone tissue, the brain is sheathed in a loosely form-fitted sack composed of layers of tough protective tissue called the *dura mater* that exists between the skull and the outermost surface of the brain.<sup>2,3,26,27</sup> Until the computer age began and the magnetic resonance imaging (MRI) scanner was invented in the mid-1900's, the physical structure of brain anatomy was learned through post-mortem dissections with little-to-no clues as to the function within the body's themselves.<sup>1,28</sup> Up to this point, the functionality of these complex structures found within the skull could only be hypothesized about by post-mortem comparisons of relatively healthy individuals to individuals that survived traumatic brain injuries, suffered from certain congenital developmental defects; or lost some sort of physical or behavioral functionality due to the development of a lesion or tumour (assuming careful observation of behavioural changes could be made following the accident and prior to death). Even in the best of these cases arguments were primarily anecdotal and based heavily on supposition.<sup>1,27,28</sup>

With the introduction of MRI as a diagnostic tool in the 1970-80's it became possible to non-invasively obtain detailed visual images of a living individual's brain by oscillating a strong magnetic field in the radio frequency range to excite biological molecules with magnetic properties (such as dipolar water molecules).<sup>29</sup> With this technique, distinguishing between the subtle

differences in the local density of water molecules present in the various soft tissues comprising the brain clearly showed the various structural features; unlike older techniques such as X-ray imaging which requires significant contrast in density between tissues.<sup>28,29</sup>

While this achievement was of Nobel Prize winning significance, neuroscientists discovered rather quickly that each brain is somewhat analogous to a fingerprint; generally similar but always slightly different from patient to patient.<sup>28</sup> They found that large topographical landmarks shared between individuals didn't necessarily share identical functionality due to microstructural differences below the 1 mm<sup>3</sup> limit of spatial resolution achievable through MRI.<sup>28</sup>

However, the brain is highly vascularized with complex networks of arterial and venous pathways transporting blood throughout the various structural modules with relative ease and speed.<sup>1,2,26,28</sup> These pathways and the oxygen-dependent magnetic properties of the hemoglobin molecules in blood have allowed for an indirect measure of neural activity using advanced functional MRI (fMRI) technology to observe “real-time” changes in local concentrations of deoxyhemoglobin (a paramagnetic, iron-containing biomolecule) as individuals perform specific tasks within an fMRI.<sup>28,30</sup> *Blood-Oxygen Level Dependent* (BOLD) correlations between behavior and blood-oxygen concentration changes in certain neural structures have been used to provide further evidence of functionalities of specific structures of the brain.<sup>30</sup> Unfortunately, the spatial resolution of fMRI is only 3 to 5 mm and they have a low temporal resolution of 4s (two orders of magnitude slower than the neural activity causing the change).<sup>28,30,31</sup> MRI and fMRI have become indispensable tools in neurosurgery and neuroscience, have revolutionized cognitive neuroscience and are responsible for much of our knowledge of the structural-functional

relationships of the modules of the brain, although caution is still used when interpreting these results for clinical applications.<sup>28</sup>

Unlike most other organs, the brain is composed of several visibly distinct (though completely interconnected by nerve cells) sections of diverse tissues that have been grouped in terms of their development, histological structuring and functionality into four physical components/modules; In ascending order of their evolution over the past 600 million years, they are: the brainstem, cerebellum, diencephalon and cerebral cortex (shown in various artificial colours in Figure 2, below, illustrating a midsagittal-section of the human brain).<sup>3,26,27</sup>

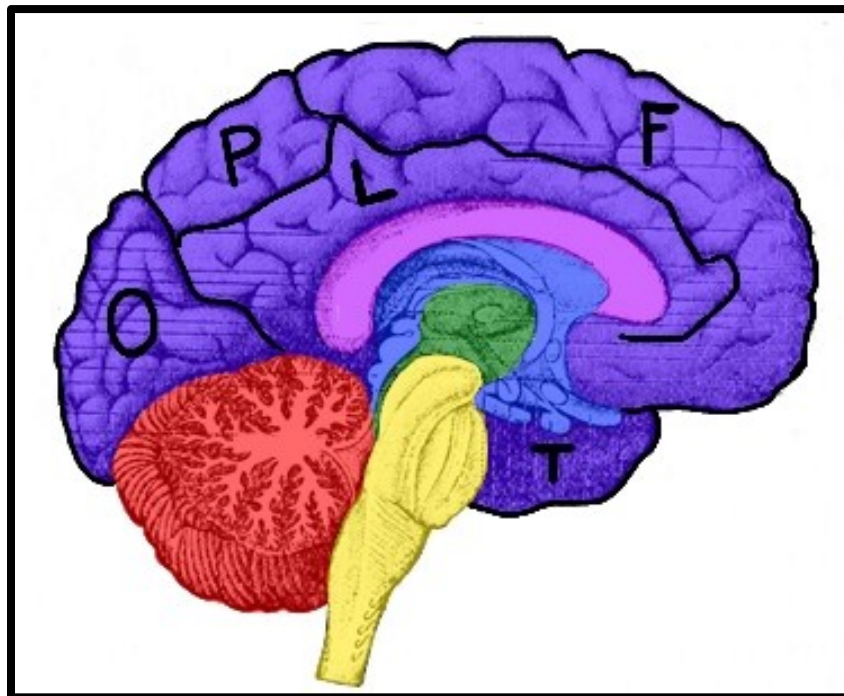


**Figure 2** – An artificially coloured midsagittal section of the human brain showing the medial surface of the left cerebral hemisphere. Yellow: brainstem; Red: cerebellum; Green: diencephalon; Blue: ventricles/other intracerebral components; Pink: corpus callosum; Purple: cerebral cortex (Black: approximate parcellation lines).  
(Labels of cortical lobes: O – Occipital, P – Parietal, L – Limbic, F – Frontal, T – Temporal)

### 2.2.1 THE BRAINSTEM

The first part of the brain to evolve, starting just above where the spinal cord has been truncated off in Figure 2, was the brain stem. The brain stem includes several sub-modules: the *medulla oblongata*, *pons*, and *midbrain*, which are unconscious controllers/moderators of essential bodily functions such as heart rate, respiration rate, and blood pressure. As the most primal, reptilian portion of mammalian brain, it is also involved with the autonomic reflexive reactions to sudden changes in light, gravity or sound.<sup>2,27</sup>

### 2.2.2 THE CEREBELLUM

The cerebellum, or little brain, sits slightly behind the upper portion of the brainstem and is heavily interconnected with both the brain stem and the other higher-level modules.<sup>3,26</sup> Functionally, the cerebellum's cortices are involved with planning movements and motor-coordination, although, as with the brainstem, many input/output connections are established with other nearby modules, allowing for further signal analysis/processing by the next levels of modules which constantly feedbacks into the motor control processes, for example.<sup>2,3,27</sup>

### 2.2.3 THE DIENCEPHALON

Continuing up from the midbrain towards the cerebral cortex, there is an interbrain region called the diencephalon, which contains many functional sub modules, notably, the pituitary gland, the *thalamus* and *hypothalamus*. As with the modules before, numerous interconnections to the cerebral hemispheres of the neo-cortex as well as the cerebellum and brain stem.<sup>2,3,27</sup>

The *thalamus* is the larger of the two, developing in conjunction with the cerebral hemispheres and acting as a signalling gateway to the various cortices

of the cerebral cortex.<sup>27</sup> The *hypothalamus* is smaller and mostly controls the neuroendocrine system through the pituitary gland but also organizes the activity of the autonomic nervous system and has functional connections to the expression of basic drives, regulation of water, and manifestations of emotional behaviour.<sup>27</sup>

## 2.2.4 THE CEREBRAL CORTEX

The cerebral cortex (or the cerebrum or neo-cortex) consists of two cortical hemispheres separated lengthwise by a deep longitudinal fissure but remain interconnected by the *corpus callosum*, a region of tissue enabling communication between the two hemispheres.<sup>2,3,26</sup> Visually, the cerebral cortex appears to be folded in on itself with ridges called *gyri* and valleys called *sulci* - parcellations separating each cortical hemisphere into the five functional lobes are done by deep *sulci* called fissures.<sup>2,3,26</sup> The five functional neocortical stereo lobes are the frontal, temporal, occipital, parietal and limbic lobes. They are all used to varying extents and in various combinations for almost all sensory perceptions and interpretations, actions related to the motor systems, and for consciousness and cognition.<sup>2,3,27</sup>

Due to its volume and the complexity of its connections, the cerebral cortex dominates control over the CNS and even has some ability to override autonomic controllers for most regulatory functions within the body. This dominance over the CNS and the parcellation of each pair of cortical lobes based on the functional specialization makes the neo-cortex the target of choice for acquiring the electrical signals required for an active, controllable interface between computers and the human mind.<sup>2,3,27,32</sup> Quite fortunately, pyramidal nerves of the neocortex cluster together into groups based on the motor and sensory nerve groups that are transmitting or receiving signalled information to the neo-cortex. As a result, all of the nerves of the body, the

hand for example, are localized into a specific area that spreads across a portion of the surface of the neo-cortex.

## 2.2.5 THE VENTRICULAR SYSTEM

Although not technically a structural module of the brain in the sense of those highly organized and functionalized formations of tissue just discussed, there exists a system of ‘negative spaces’ or voids throughout the inner brain that are noteworthy as functional anatomical features.<sup>3,27</sup> The largest type of these void spaces are called ventricles and are fluid-filled reservoirs containing one of the body’s most unique, chemically complex and irreplaceable fluids: cerebrospinal fluid (CSF).<sup>1-3</sup>

The ventricular system is interconnected throughout the interior of the cerebral cortex and surrounds much of the diencephalon.<sup>2,3,27</sup> Permeating throughout all the small gaps and spaces between the neural structures and into the extracellular matrix (ECM) of the brain’s tissues, (as well as throughout the spinal cord), it provides mechanical support and immunological protection to the brain.<sup>2,26</sup> The brain is kept buoyant with CSF, preventing its own weight from cutting off the circulation of blood. It has a complex and highly variable chemical composition due to its many roles including cleansing metabolic waste from the numerous cellular chemical reactions involved in signalling and maintaining the homeostatic regulation of neuroendocrine factors in the CNS.<sup>1-</sup>

<sup>3,26,27</sup>

## 2.3 - NEURAL HISTOLOGY AND FUNCTIONALITY

Each large anatomical module of the brain has demonstrated that it is specialized to carry out specific functionalities within the brain or body (although neuroplasticity can greatly modify the location in which these cognitive functions occur).<sup>1,2,33</sup> The functionalities are achieved through a large variety of specialized tissues rich with specialized sub-modules, or nuclei, working in unison throughout the brain. Every function of the brain is completed using two categories of cell type: neuronal and non-neuronal cells (or nerve and glial cells).<sup>1</sup>

Neurons comprise all of the complex signal pathways running throughout the entire body as various complex, functionally specialized nervous systems, including the CNS, and with the support of non-neuronal glial cells, neurons send and receive specialized electro-chemical signals throughout the brain and the entire body.<sup>1</sup>

Neurons are the fundamental building block for all nervous systems which requires that a great variety of differently capable cell types. However, despite being largely stratified by their size and specialization, all neuronal cells share four structural features: 1) a cell body or, *soma*, made up of the plasma or cell membrane, enclosing a large nucleus and the other organelles within its cytoplasm; 2) a single, long nerve process called an axon extending out from the *soma*; 3) the axon can then branch out and terminate at multiple presynaptic or axonal terminals, forming connections with the axons from other neurons; and in the opposite direction of the axon; and 4) a variable number of branching, tree-like processes called dendrites form a 3-dimensional dendritic field with numerous postsynaptic connections to pair with presynaptic axonal terminals and other critical processing complexes.<sup>1,2,27</sup>

Unfortunately, the use of this nomenclature can be quite ambiguous at times due to the sheer complexity of neuronal circuits, the variety of cell types, as shown in Figure 3, below, for example, and the number of disconnected scientific endeavours around the globe all occurring simultaneously and without governing organizations or a global system like IUPAC in place.

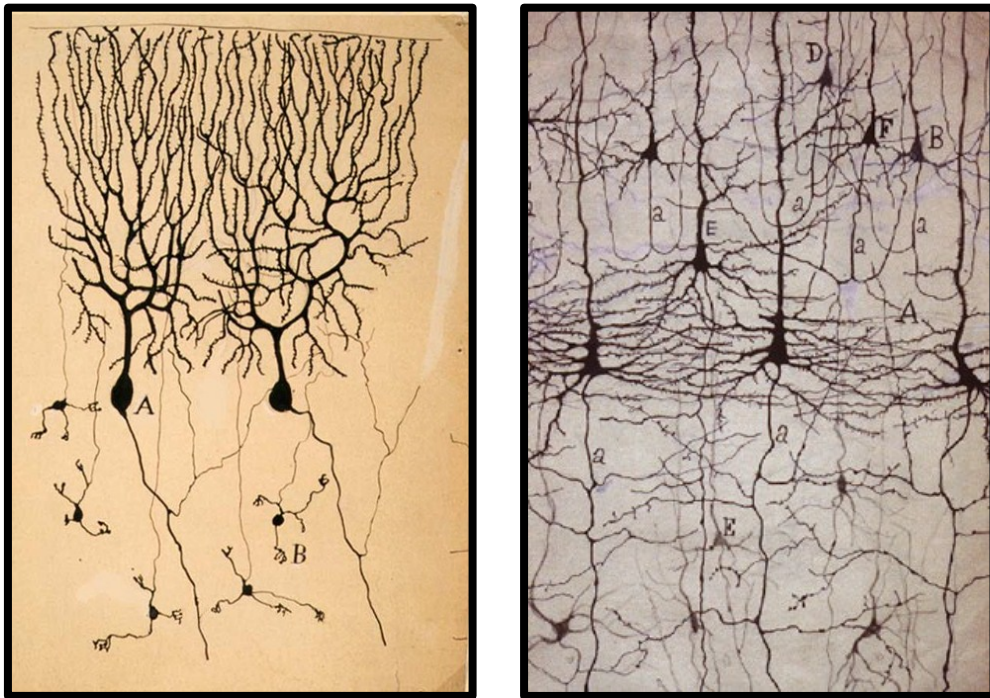


**Figure 3** – Drawings of a few Purkinje neurons from the cerebellum (left) and a small section of networked pyramidal neurons from the cerebral cortex (right) done and first published in "Comparative study of the areas of the human cortex" (1899) by Santiago Ramón y Cajal.

The other types of cells in the CNS that play a more supportive/maintenance role are generally classified as glial cells, although it is a wide classification of cell types and can be further subdivided into several categories: astrocytes (fibrous and protoplasmic), oligodendrocytes, radial glial cells, ependymal cells and microglial cells.<sup>1</sup> Glial cells do not get directly involved with the transmission of signals but they do compose the extracellular matrix that supports the network of nervous cells and play many important roles that enable neural networks to form as they do; such as the myelination of long

signalling-axons, maintaining the blood-brain barrier, and providing any necessary immune response.<sup>1</sup>

### 2.3.1 MICROSTRUCTURAL CELLULAR ORGANIZATION

From a histological perspective, the brain presents an incredible challenge; not only is there a huge variety of neuronal and glial cell types available to compose the various microstructures of the brain's tissues but their heterogeneous distribution is highly controlled and specifically organized depending on the tissue and the function meant to be performed.<sup>1,2</sup> Not only do neurons exist in a variety of sizes and types, every one of the hundreds of billions of neurons within the brain have been organized in highly specific arrangements for each type of tissue.<sup>1,2,26,27</sup>

Glial and nerve cells are approximately equal in number throughout the brain, although they are not evenly distributed: the regions of white tissue (so-called "white matter") are primarily glia while the darker regions of tissue ("grey matter") are dense with nerve cells.<sup>1</sup>

The density of nerve cells is so great that it wasn't until the early 20<sup>th</sup> century when the neuroscientist Santiago Ramón y Cajal applied the Golgi staining method to nervous tissue slices (which dyed only a small portion of the neurons randomly instead of all of them as other staining methods of the time would, allowing for their shapes to be distinguished at last) and famously sketched various neuronal cell types, their complex and variable morphologies, and the complex organizational structures specific to certain nervous tissues throughout the CNS.<sup>1</sup> Shown in Figure 4 is one such sketch by Ramón y Cajal that first illuminated the highly organized tissue of the cerebral cortex and the predominance of pyramidal neuronal types present in the neo-cortex.

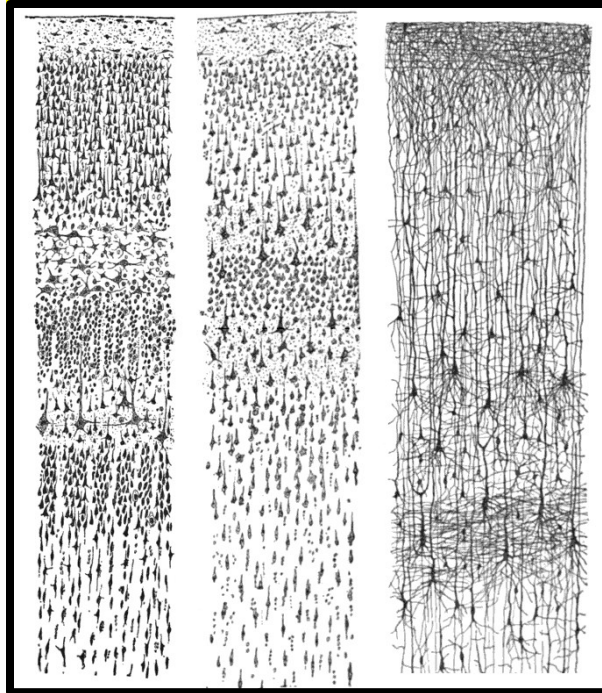


**Figure 4** – Another Ramón y Cajal sketch from "Comparative study of the areas of the human cortex" showing a comparison of the highly organized pyramidal neurons and other neurons as arranged in tissue from various sensory areas of the neo-cortex.

The histological arrangement within the tissues of modules with proven functional purposes, (such as the arrangements in the 3-layer cortex of the cerebellum and the 6-layer cerebral cortex, both of which contain certain nerve cell types specifically organized into distinct but interconnected layers,) suggests a functional dependency of those tissues on these formational arrangements of specific cells.<sup>1,23,34</sup> This need is true even in relatively small groupings of similarly stereotyped neurons that have formed into organized clusters (also known as nuclei or ganglia), each of which performs some sort of functional (perhaps computational) task within the tissue that contributes to the process of cognition.<sup>34</sup> Hopefully this section has effectively demonstrated the need to design neural probes that maintain the natural structural forms of both the neural tissues and the network pathways therein to properly analyse their signalling mechanisms and glean more understanding of the purpose for these complex arrangements.<sup>4,34</sup>

## 2.4 - MODES OF INVESTIGATING NEURONAL SIGNALLING

Due to the volume of the brain, its various evolutionary stages, the diversity of its modular components and the histological and organizational complexity within each specialized tissue, researchers have been working both top-down and bottom-up approaches to build an understanding of both the “high-level” behavioral functionalities of the conscious mind and the “low-level” specifics of cognitive mechanisms within the complex neural networks that interact to allow for such high-level cognition to occur.<sup>23</sup>

One of these top-down approaches is achieved through non-invasive methods that have similarities with what has primarily been discussed so far in this chapter, where the high-level functionality of macroscopic modules of the brain have been observed and experimented with as a type of “black-box.”<sup>23</sup>

### 2.4.1 TOP-DOWN INVESTIGATIVE MODES

In 1929, a German psychiatrist named Hans Berger invented electroencephalography (EEG) with which he reported the presence of small but detectable fluctuations electrical potentials measured with an electrode placed on the scalp of a patient.<sup>28,35</sup> EEG is still one of the most widely used non-invasive techniques for measuring the localized electrical field potential fluctuations at the surface of the neo-cortex.<sup>28</sup> The local field potentials (LFPs) are one of the two foundational modes of measuring and monitoring electrical activity locally within the brain. However the EEG approach to recording these signals is, unfortunately, not without its limitations.

One such limitation is that each EEG electrode channel of an covers approximately 9 cm<sup>2</sup> and thus provides signal information based on the net

average potential resulting from the combination of the myriad neuronal signals occurring within a step of temporal resolution (around 0.001s).<sup>28</sup> This means that the sample populations of neurons being monitored in the cortex need to fire or fluctuate synchronously to generate potentials measurable by this method, making the contributions and firing patterns of individual neurons hard, if not entirely impossible, to discern.<sup>23</sup>

The non-invasive nature of the EEG is wonderfully effective in diagnostic and imaging applications with human patients suffering from many types of neural dysfunctions.<sup>36</sup> However, a major limitation is that it lacks high spatial resolution and it isn't invasive enough to make the observations desired by the neuroscience community trying to understand the basis of cognition from a more intimate perspective.<sup>4</sup>

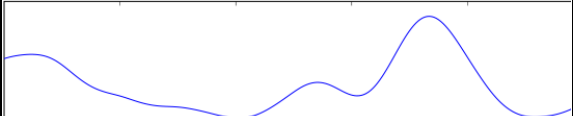
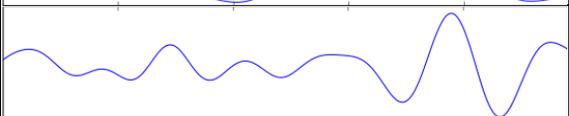
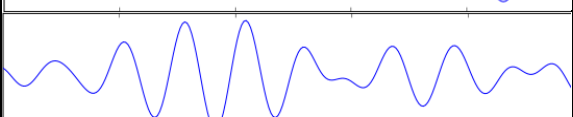
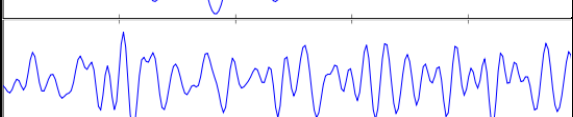
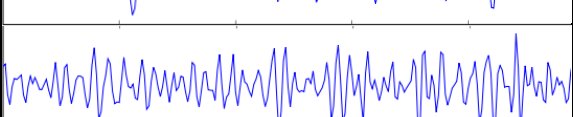
Many significant advancements in EEG technology have improved the quality of the signals obtainable through increasing the number of electrode channels and improved peripheral electronics, yet there are significant limitations in both signal strength and the measurable frequency band due to the distortional and attenuating interference of the various hard and soft tissues between the signal source and the recording sensor (i.e. skin, bone and other tissues).<sup>28</sup> Despite these intrinsic limitations, several distinct “brain-rhythms” or “wave-bands”, such as the alpha-, beta- and gamma-bands, have been related to certain types of brain function or levels of activity.

The frequencies used to define the edges of these wave bands are not firm and depending on the source two individuals could each apply a “standard  $\delta$ -band filter” and still end up with different results. This becomes even more of an issue at higher frequencies in the spectrum.

For example, shown below in Table 1, generic one-second snippets of recorded signal waveforms have been processed using low-pass filters and narrow and

standard band-pass filters to selectively isolate the frequency bands of interest and visually demonstrate the patterns.

**Table 1** – Example Electroencephalogram Brain Rhythm Bands

Frequency Band	Frequency Range	Example: 1 Second of Wave Pattern*
Delta ( $\delta$ )	< 4 Hz	
Theta ( $\theta$ )	$\geq 4 < 8$ Hz	
Alpha ( $\alpha$ )	$\geq 8 < 14$ Hz	
Beta ( $\beta$ )	$\geq 14 - 30$ Hz	
Gamma ( $\gamma$ )	30 - 100 Hz	

\*from [https://en.wikipedia.org/wiki/Electroencephalography#Wave\\_patterns](https://en.wikipedia.org/wiki/Electroencephalography#Wave_patterns)

The other approach to investigating the brain is the bottom-up approach that breaks these large structural components down into smaller and smaller pieces until the neural circuitry within becomes manageable in scope, and some (albeit basic) understanding of simple, low-level behavior and functionality can be obtained.<sup>37,38</sup> With this bottom-up approach starting at the cellular level (or even the molecular level), as more information is obtained, the compilation of these findings as a group and the sharing of these findings with the top-down group, and *vice versa*, allows for another step up in the investigation of the complexity of neural circuitry.<sup>37</sup>

## 2.4.2 BOTTOM-UP INVESTIGATIVE MODES

*In vitro* electrophysiology has been looking at simple cell-to-cell interactions and slowly building up a solid understanding of more and more complex cellular circuits with more cells and the inclusion of multiple cell types.<sup>1,8,39</sup> Similar in many ways to the histological analyses performed to learn about the static organizational regimes found in various neural tissues, these investigations require the direct interrogation of interior brain features.<sup>4</sup> However, the rapid cellular death of neurons upon their excision from their native living tissues creates a significant obstacle in observing their natural dynamic behavior and prevents much of the experimentation required to make effective observations.

Through the use of animal models and the development of complex methodologies, electrophysiological pioneers such as Henry McIlwain, have found a way to maintain the cellular vitality within small portions of nervous networks in the form of thin slices of living tissue *in vitro*.<sup>40</sup> These *ex vivo* experiments are commonplace today in the neural physiological sciences and have enabled neuroscientists to increase their understanding of the mechanisms of neuronal circuits.<sup>41</sup> Detailed information on the procedures and techniques used in brain slice based electrophysiology can be found in Appendices A-1 through 4.

It has been found through these electro-physiological methods that the application of potential to one neuron can initiate a chain-reaction or domino effect in which the excited cell spontaneously “fires” off a signal to its interconnected neighbors which, depending on the cell types and circuitry in question, can also become adequately stimulated and propagate the signal independently further through the neuronal chain.<sup>1,39</sup> With respect to electrical potential as the applied stimulus, it has been found that at specific levels of

applied potential neurons will behave in the predictable and consistent fashion, transmitting a transient potential along through the nervous networks.<sup>1,23,39</sup> The potential applied depends on the cell type and the behaviour is identical to that found within naturally firing nervous networks.<sup>42</sup> This type of signalling mechanism is called an action potential (AP) and is the fundamental mechanism that results in all higher levels of function and cognition, including the previously discussed LFPs.<sup>43</sup>

### 2.4.3 NEURONAL SIGNALLING MECHANISMS

Consciously and unconsciously, the CNS is constantly exchanging and processing an overwhelming sum of information from external sensory stimuli and internal stimuli, all of which is being passed spontaneously throughout the body using transient electrochemical and chemical potential gradients as signals between a distributed network of neurons around 100 to 200 billion strong.<sup>2,4</sup> However, despite the overall number of cells involved and the complexity of the cellular organization within the various tissues, when sufficiently broken down into small enough quantities, neuroscientists researching the signalling pathways of the brain have managed to learn about various nerve cell-assemblies by utilizing animal analogues.<sup>39,44,45</sup> These signals are either chemical or electrochemical and specific detection methods must be used for certain types of signals.<sup>46</sup>

Chemical signals involve a multitude of specialized molecules such as neurotransmitters being selectively transported across cell membranes (by use of highly-specific chemical receptors) and between interconnected neurons at a structural junction known as a synapse.<sup>1,23</sup>

Electrical signals are the result of two separate, but not independent, signal types: a transient ionic current travelling intracellularly along an axon between

neurons, called an action potential (AP), and the local electrical field potential (LFP) generated between two points within the extracellular matrix (ECM) as unequal concentrations of ionic species result due to a myriad of constant intracellular signals.<sup>1,23</sup>

### 2.4.3.1 ACTION POTENTIALS

An action potential (AP) is named as such due to the dynamic pulse of transient electrical potential measured in association with the activation and rapid propagation of a charged neural signal from one neuron to the next.<sup>23,42</sup> APs have a fixed peak-amplitude and duration for a given neuron and in some cases can easily overcome large distances. To activate it, the LFP surpasses a threshold potential value in proximity to the neuron, the AP spikes, rapidly transmits the signal along its axonal fibre to the presynaptic terminal where it is connected to a dendritic arm of the next nerve in the chain, which, given the appropriate conditions in the local surroundings, could then initiate another AP, and so on.<sup>1,42</sup> APs are all-or-nothing, they cannot be stopped partway and they require a rest period before they can send out a signal again. That said, there is a threshold value that exists to ensure that the AP fires as a result of adequate stimulus. See Figure 5 below for a visual schematic of this process.

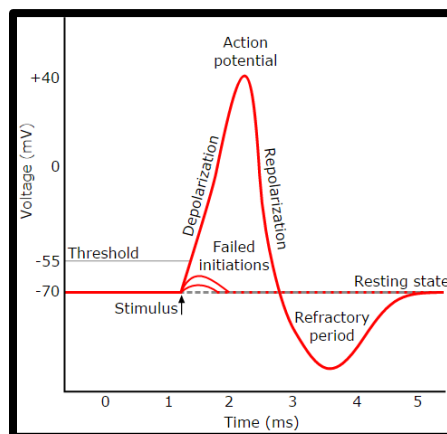


**Figure 5** – Example neuronal action potential. Initially at -70 mV, then +110 mV in 1 ms, then -110 mV in 0.4 ms, then -40 mV in 0.8 ms, then +40 in 1.5 ms and ready to fire again.<sup>42</sup>

The firing frequency of the AP relates to the intensity of the incoming stimulus.<sup>1,42</sup> The amplitude and duration of the AP signal varies only slightly between various neuron types and is consistent across species;

Neuronal firing patterns can vary greatly depending on the quantity and types of nerve cells present in a given neural circuit, allowing for more diversity and complexity in signalling and therefore in information processing as well.<sup>23,42</sup>

#### 2.4.3.2 LOCAL ELECTRICAL FIELD POTENTIALS

Localized increases/decreases in the concentrations of aqueous ionic chemical species, such as  $\text{Ca}^{2+}$  or  $\text{Cl}^-$ , in various regions and the excess/deficit concentration of charge relative to other regions creates an electrical potential gradient called a local field potential (LFP).<sup>1,23,37</sup> LFPs are continuously generated by synaptic signalling responses associated with internal and external stimuli, such as motor functions and sensory processes, as well as all other contributions from any other neuronal signalling processes.<sup>23,36</sup>

### *SYNAPSES*

Synapses are highly specialized and sensitive communication junctions between individual neurons. Numbering into the tens of thousands for a single neuron, they are found throughout the cellular membrane of the tree-like dendrites. These specifically-sensitive branches overlap and interconnect with neighboring neurons of similar type as well as the axons from other neuron types, such as sensory nerve cells.<sup>1</sup>

Each synapse acts as a kind of gate in the membrane of a neuron, responding to specific neurotransmitter molecules in the nearby CSF, which creates a cross-membrane potential that causes the transport of charged molecules into the neuron or out of the neuron into the CSF in the nearby ECM.<sup>1</sup> Although the

general signalling mechanisms themselves are fairly well understood, with such a huge variety of functional and highly-specific receptors that exist, synaptic signalling is incredibly complex.<sup>1</sup>

The continuous in-taking and discharging of charged species into and out all of the neurons spread out spatially throughout the ECM creates non-equilibrium concentrations of charged species between regions of tissue causing local electrical field potentials (LFPs) to develop and dissipate within the CSF throughout the ECM.<sup>1</sup>

LFPs fluctuate throughout the brain at relatively low frequencies (< 500 Hz) due to the continuous transport and/or diffusion of charged species throughout the tissue.<sup>32</sup> The neo-cortex contains measurable LFPs generated within the top layers of the cerebral cortex where a dense forest of dendrites from underlying pyramidal cells exists (refer back to Figure 4).<sup>23</sup>

Due to the organizational structure of the pyramidal cells of the neo cortex, the LFPs across the neocortical surface are much more easily distinguished than in other areas of the brain making it ideal for use in BCI. This is due to the relatively large separations between the signal sources and drains as they move along the “2-D” surface of the cortex through a sea of intertwined dendrites.<sup>1</sup> Many questions remain about the specifics of these signals. A couple big ones are: *Why are these signals being generated? And where are they propagating to (or from)? And how can I use their signals to control my phone?*

## **2.5 - IMPLANTABLE BRAIN-COMPUTER INTERFACES**

Brain-computer interfaces (BCIs) have become a hot topic in both science fiction (sci-fi) and, rather amazingly, in real-world clinical applications these systems have been able to restore sensory function or motor control in an almost sci-fi like manner.<sup>6,14,47-49</sup> The end goal of these technologies is to implant a device capable of providing signalling information from a region of the brain and to do so chronically over a time scale of decades to an entire lifetime.

### **2.5.1 HIGHLY-INVASIVE IMPLANTABLE BCIs**

To acquire the desired signal information the brain is often, though not in all cases, further invaded through the traumatic insertion of a neural probe through the blood-brain barrier (BBB) into the depth of neural tissue, but, unfortunately, as with all injuries, the immune system reacts acutely and aggressively to begin rectifying the unwanted introduction of a foreign body.<sup>10,50,51</sup> This acute reaction, initiated and carried out by glial cells such as astrocytes and microglia, will continue chronically for the next several days or weeks until a myelin seal that fully encompasses and neutralizes the invading body has been created. This scar-forming process is typically called “gliosis” and it is the largest challenge for invasive scanning technology to overcome.

Microwire electrodes, microwire electrode arrays, tetrodes and 2D/3D silicon shanks and arrays are all technologies that been used recently in neuroscientific research as neural probes. As such, their uses, compositions, performance strengths and shortcomings will be briefly covered before moving onto the focus of this experimental work, the flexible  $\mu$ ECoG. These highly-invasive probes are all meant to penetrate deep into the tissue of interest, but

the road to the current generation of neural probes has not been a short and painless one.

### 2.5.1.1 MICROWIRE ELECTRODES, TETRODES AND MICROWIRE ELECTRODE ARRAYS

An array of 80  $\mu\text{m}$  diameter micro-wires made of stainless steel (SS) was first used to monitor the neural activity of living, freely moving rats by Strumwasser in 1958 due to the development of micro-fabrication techniques.<sup>20</sup> Since then the electrode material selection has expanded to include tungsten (W), platinum (Pt), iridium (Ir), platinum-tungsten (Pt-W) alloys and platinum-iridium (Pt-Ir) alloys, although stainless steel and tungsten continue to find use due to their low cost and ability to effectively record signals for timeframes lasting over a year.<sup>20</sup>

Two of the major drawbacks in the use of micro-wire electrode arrays are that the electrodes are only capable of measuring a single neuron at a time, meaning that the volume of tissue displaced upon insertion follows an increasing trend with the number of electrodes being inserted, and that as the diameter is reduced to increase selectivity and reduce tissue displacement, the high aspect ratio micro-wires may deform by bending upon insertion, leading to inconsistent, unpredictable electrode depths.<sup>20</sup>

In addition to the configuring the micro-wires into an array, a common configuration to improve the stiffness while maintaining selectivity is the so-called “tetraode.” Fairly commonly used, tetraodes consist of 4 wires that have been twisted into a micro-wire bundle that is both more mechanically stable and is capable of recording and localizing multiple neuronal signals.<sup>20</sup>

### 2.5.1.2 PLANAR SILICON MULTI-ELECTRODE SHANKS AND ARRAYS

Realizing the limitations of these wire based approaches and with the advent of new modes of fabrication, namely those used in microelectronic production to create integrated circuits (ICs) for microprocessors, thin-film fabrication methods were adapted and applied to create planar, silicon based probes with improved mechanical properties as well as enabling more advanced electronic components to be incorporated into the design of the neural probes.<sup>10</sup>

These stiff, mechanically strong probes could have multiple electrodes patterned along their shaft length and can even be made up of several shafts of controlled length and separation.<sup>10,52</sup> Some of these designs have become commercially available standards for neural probe design, such as the Michigan, Utah and Twente MEA styles. Shown below in Figure 6 is a Michigan style MEA probe, on the left, and a Utah style MEA, on the right.

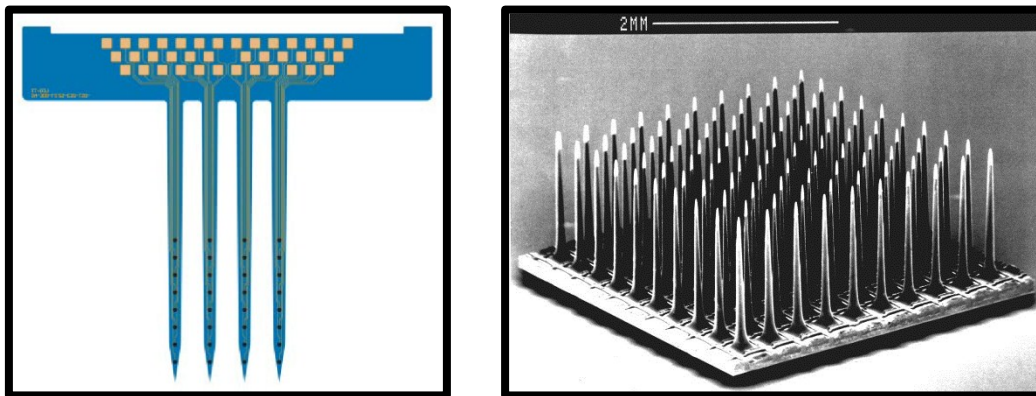


**Figure 6** – Silicon based penetrating neural probes.  
(Michigan style probe on the left<sup>52</sup> – Utah style probe on the right<sup>53</sup>)

Still being further developed today for enhanced performance, these probes have been successfully used as neural implants in human patients as BCIs and have been applied in many ways including treatments for Parkinson's, amputees, blindness, deafness, epilepsy, paraplegia, and computer systems

control, etc.<sup>6</sup> Unfortunately, they are not without severe limitations in their performance lifetimes, surgical costs and legal and ethical complications.<sup>54</sup>

Foreign body response and the required craniotomy have made the experimental implantation of these probes in human subjects quite limited despite their relative success.<sup>32,55-58</sup> The largest factor limiting the application of these probe types is the foreign body or immune response that is triggered by the body upon their implantation as the probe shafts break the blood-brain barrier (BBB) and cause tearing within the tissues into which they are inserted.<sup>10,55</sup>

The acute foreign body response is the inflammation of the surrounding tissue. As time progresses, the glial cells will react to restore the BBB by forming a dense, signal blocking glial scar.<sup>10,50</sup> There is a varying degree of immune system response to these probes depending on several factors, such as the size of the probe, material composition and mechanical trauma to the surrounding tissue.<sup>10</sup> However, any object piercing into the BBB, even those considered biocompatible, will illicit an immune response without more advances in the bio-functionalization of implant materials.<sup>10,59-62</sup>

Currently, the foreign body response to an implanted probe eventually results in encapsulation by glial cells (such as fibroblasts, macrophages, microglia, and astrocytes) - As a result, the line of communication between the electrode and local neurons becomes blocked within a time frame of weeks to months.<sup>63</sup>

## 2.5.2 PARTIALLY-INVASIVE IMPLANTABLE BCIS

There is a type of neural probe that requires a surgical craniotomy procedure to expose the sub-dural cerebral cortex considered to be partially-invasive (despite the required craniotomy), since its placement doesn't acutely disrupt any neural tissue or network connections and the body's rapid response to a

ruptured BBB is eliminated - It does not break through the BBB in the brain but instead just makes intimate contact with the surface is This type of neural probe.<sup>64</sup> However long-term implantations may find a slower immune response that occurs due to the presence of a foreign object over a longer period of time.<sup>65</sup> This type of neural probe is similar in its function and signal acquisition capability to the EEG, however, with its placement being directly onto the cortical surface of the brain, it is called an electrocorticogram (ECoG).

### 2.5.2.1 ELECTROCORTICOGRAPHIC MULTI ELECTRODE ARRAYS

Electrocorticography (ECoG) is, quite simply, the measurement and recording of the electrical neural activity at the cortical surface of the brain through some electrical means. Although the ability to measure this activity, both in humans and other animals, was first discovered in the late 19<sup>th</sup> century, ECoG signals have become the subject of much attention in the past few decades of research in the field of neuroscience.<sup>32</sup> These recent studies using ECoG have primarily been performed through animal studies due to the questionable ethics surrounding recreational craniotomies, although some human studies do still occur when the opportunity presents itself during unrelated neurosurgical procedures for the treatment of intractable epilepsy, tumours and speech disorders.<sup>32</sup>

At the mm-scale, flexible sub-dural ECoG neural probes made with 3 mm diameter platinum (Pt) electrodes supported within a high-density poly(ethylene) (HDPE) matrix (see the left side Figure 7, below) have shown themselves to be effective BCIs because they are: acutely unnoticed by the non-neuronal, “maintenance” cells responsible for gliosis (glial scarring) by being placed between the *dura* and the *arachnoid maters* - not tearing the neo-cortical tissue like penetrating-shank style neural probes;<sup>2,3,4</sup> biologically compatible, utilizing non-toxic matrix and electrode materials;<sup>2,5,6</sup> durable

enough to be handled and used practically, yet flexible enough to conform somewhat to the surface of the neo-cortex;<sup>7,8</sup> and able to record high-fidelity, full-bandwidth signals across a neo-cortical region of interest.<sup>9-11</sup> An example of a commercially available mm-scale ECoG probe with 64 3 mm diameter Pt discs arranged in an 8 x 8 array within a polyethylene matrix is shown on the left of Figure 7, below.

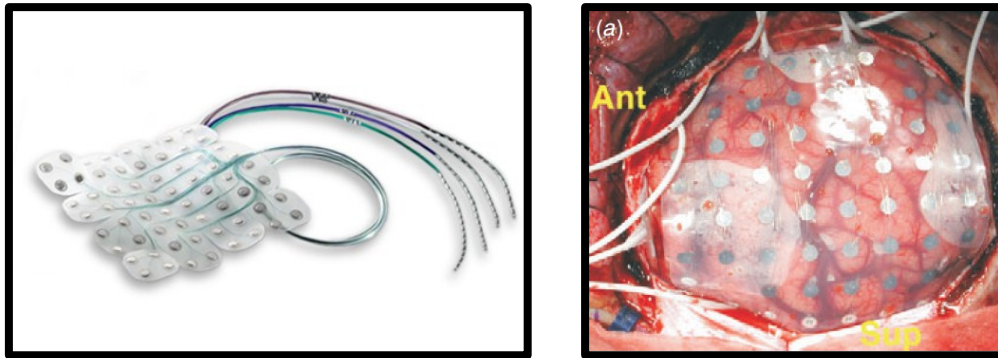


**Figure 7** – Cervello® Elite EcoG with an 8 x 8 array of 3 mm Pt electrodes.<sup>64</sup>

The ongoing advancements in ECoG neural probe technology being made by research groups worldwide have significantly improved: the available matrix materials, number of electrodes, size of the electrodes and the arrangement and spacing of the electrodes.<sup>10</sup>

Due to the immune response elicited by the penetration of neural tissues with rigid silicon probes, the thin-film IC fabrication processes that were initially used to fabricate silicon-based planar, penetrating-shank neural probes and probe arrays have since been adapted and applied to reduce the size of mm-scale ECoG electrode arrays down to the  $\mu\text{m}$ -scale.<sup>66</sup>

Now, flexible  $\mu\text{ECoG}$  probes are currently capable of detecting local electrical field potentials directly from the neo-cortical surface with electrodes the size of pyramidal neuronal cell bodies (10  $\mu\text{m}$ ) and with spatial resolution matching of the neuronal cells arranged in neo-cortical tissue (30  $\mu\text{m}$ ).<sup>67</sup>

To exemplify these advancements, a cutting-edge flexible  $\mu$ ECoG with 360 actively-multiplexed  $300\ \mu\text{m} \times 300\ \mu\text{m}$  Pt electrodes made by Viventi, et al. is shown in Figure 8, below.<sup>68</sup>

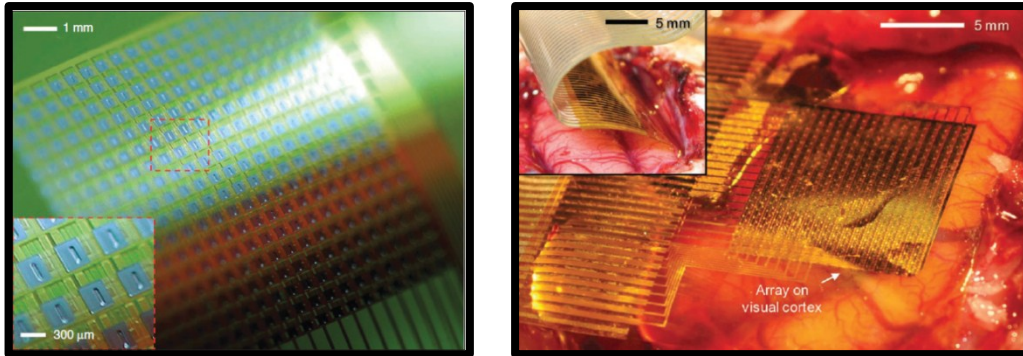


**Figure 8** – A state-of-the-art microfabricated flexible,  $\mu$ ECoG array with 360 actively multiplexed  $300 \times 300\ \mu\text{m}^2$  Pt electrodes on the left and the probe array in use on a visual cortex on the right.<sup>68</sup>

An individual electrode or sensor can only provide information as a single signal representing the averaged sum of all neighbouring sources that they can interact with.<sup>23</sup> By utilizing multiple electrodes or sensors that are arranged and separated by a certain distance, each individual signal can be analyzed relatively to the other nearby electrodes to triangulate specific neurons. The spatial resolution of a device therefore plays directly into the quality of information that can be extracted.<sup>45,69</sup>

Spatial resolution is directly influenced by electrode diameter, electrode spacing and the total number of electrodes. The diameter controls the number of cells interacted with per volume. The electrode spacing defines the unknown mechanisms involved, at least past the  $120\ \mu\text{m}$  radius limit through which some signal can be detected above the noise. Increasing the total number of electrodes provides a larger collection of data sample sets for analysis. By reducing diameter to match the average diameter of a neuron, reducing the separation to the point that there are no gaps and increasing the

number of electrodes to the maximum number possible (theoretically up to a one-to-one pairing with neurons), a clear picture of the mechanisms between neurons as they occur would be achieved.<sup>67,70</sup>

Next, in Chapter 3, I go over designing and the fabrication of the micro-electrocorticogram and the connector device used throughout this work.

---

**CHAPTER 3 - DESIGN AND FABRICATION**  
**OF A MICRO-ELECTROCORTICOGRAPHIC**  
**NEURAL PROBE SYSTEM**

---

## **3.1 - INTRODUCTION TO NEURAL PROBE DESIGN AND FABRICATION**

The signalling functions of the brain occur spontaneously and constantly through rapid electrochemical and chemical cellular interactions between myriad individual neurons spread out and interconnected into an enormous three-dimensional network; the chemical signalling products and reactants of which transport extra-cellularly and are mediated by the cerebrospinal fluid (CSF) saturated extracellular matrix (ECM) of glial cells that surrounds, supports and maintains the organic communication network.<sup>2,26</sup> As discussed in Chapters 1 and 2, the technology available for probing the neural circuitry of the brain has advanced significantly in the past few decades through the adoption of integrated circuit (IC) thin-film fabrication methods and with it our limited ability to probe into and try to understand the cognitive mechanisms of the mind.<sup>20,32,53</sup>

Chapter 3 contains the details of the design and fabrication process for the two devices which comprise the neural probe system used experimentally throughout this work.

First, I discuss the design concepts and objectives of the neural probe system I built, the two components that needed to be designed and fabricated to extract electrical signals from neural tissue and the way in which these devices interconnect. I will then go into more detailed specifics about the designs of the thin-film micro-electrocorticographic ( $\mu$ ECoG) probe and the two multi-electrode array (MEA) layouts that were created and why the layouts are such as they are. Once all the designs and schematics have been reviewed, focus shifts to the fabrication and characterization of the two devices.

The fabrication of the  $\mu$ ECoG probe device - also known as the “front-end,” as will be detailed later - begins with the fabrication of the photomasks used for photolithography, followed by a list of materials and equipment used throughout the various micro-fabrication steps, which is then followed by the steps of the micro-fabrication process flow used in creating the thin-film  $\mu$ ECoG probes are listed in detail and summarized by a table. The micro-fabrication methods used are detailed in Appendix A.1 with respect to their application within this work.

The fabrication and assembly of the other device (a “back-end” connector device, the specifics of which will also be detailed shortly in the coming sections) is then described - showing the pre-assembly preparation of the internal electronic connection pathways and the rapid prototyping 3D printing process used to create a hard-shell casing/body that houses said internal electronics.

Following this, the results from the inspection and characterizations used to investigate the dimensions and quality of the micro-fabricated probes throughout the fabrication process (including: 4-point probe, contact profilometry, and optical microscopy), the post-fabrication inspection for batch yields and results as well as the final results from electrical pathway resistance tests performed on the “back-end” connector device. The characterization methods used are discussed and reviewed in detail in Appendix A.2.

Finally, in the chapter summary, the important outcomes from the work contained in this chapter are summarized and discussed relative to the design and fabrication objectives for the front-end  $\mu$ ECoG neural probe and the back-end connector device.

In the following section we begin with the design concepts and objectives of the neural probe system’s two components.

## **3.2 - NEURAL PROBE SYSTEM DESIGN: DEVICE CONCEPTS AND OBJECTIVES**

Cellular interactions at this scale can seem relatively instantaneous, so to avoid missing any digital data from the brain's analog signal, small temporal resolutions (high sampling-rates, e.g. 22.2, 44.4 kHz) between discrete data points are important.<sup>71</sup> A device for a specified purpose with adequate spatial and temporal resolution, such as observing neuronal signalling over an area of the surface of the cerebral cortex for a BCI application or recording signals from a functional nuclei within an *ex vivo* tissue section, enables researchers to get an honest representation of the signals generated within the brain and their propagation through the neuronal network of interest.<sup>72,73</sup>

The challenge in this is not only how to make an array of tiny electrodes into contact with the neocortical tissue, but in how the signals from each of those tiny electrodes is transmitted and eventually amplified for additional digital signal processing. The simple solution here is to give the flexible device as much length as possible, given fabrication restrictions, and incorporate connector pads opposite the probe-head side of the device that can interface with a component capable of stepping the size-scale of the connectors so that external electronics can be connected and the flexible probes can be used.

This concept was introduced to me by Neuralynx, Inc. when they afforded me the opportunity to use a flexible, Kapton<sup>®</sup>-based  $\mu$ ECoG probe system that used a spring-loaded pin-board back-end device to make contact with the connector pads of the flexible probe. Their system was more specialized than I needed and lacked certain capabilities that would enable a more detailed investigation - it required several lengths of highly specialized wire-bundles and multiple

adapters all to enable a connection with the only proprietary active device controller (the Nano-Z) with which it can connect.

Neuralynx is one of several companies with probe/head-stage systems however most commercial headstages are designed for penetrating Si shank-style probes. Only Neural Nexus (founded by the creators of the Michigan-style probe) also has commercially available cortical-surface probes.

Instead of utilizing a commercial system's back-end, such as the highly-specialized Neuralynx system's back-end connector, I designed a simpler system based on their methods for electrical signal transmission and used a simple back-end connector device that performed the same passive function and enabled more detailed experimentation and investigation than would otherwise be possible by easily connecting to highly-sensitive, specialized electronics. Numerous consumable front-end  $\mu$ ECoG probe devices and the one reusable adaptor back-end connector comprise the "neural probe system" used throughout the experimental work in the following Chapters 4 and 5.

The following section contains the design concepts and objectives for this system, the devices therein and the concepts created or applied to enable their fabrication and proposed eventual use in a neural electrophysiological environment.

### 3.2.1 $\mu$ ECOG PASSIVE NEURAL PROBE SYSTEMS

One device with its design and fabrication described within this chapter is the “front-end” and the other the “back-end.” These two devices make up this passive neural probe system. The nomenclature is based on the concept depicted visually in Figure 9, below.

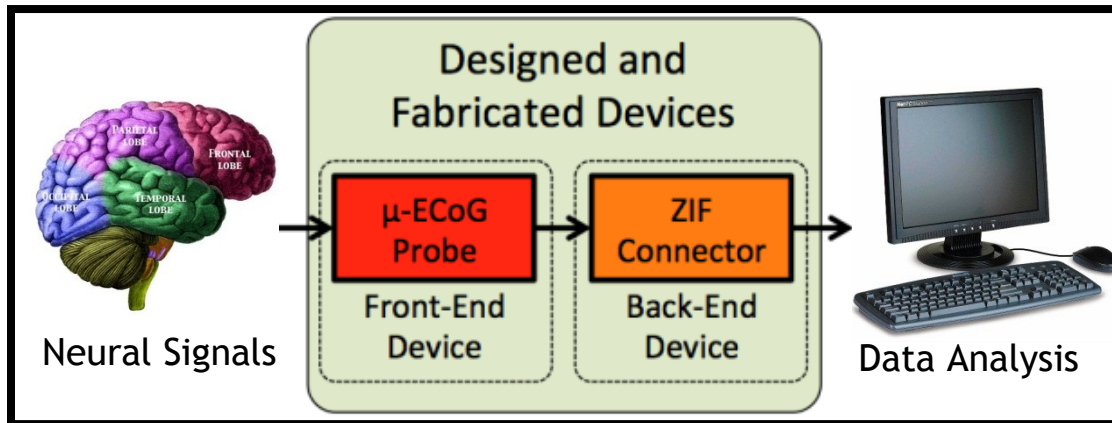


**Figure 9** – A diagram showing the fabricated devices along the signal processing chain.

It shows incoming neural signals being transduced into analog electrical signals by the front-end probe device, which then sends those signals through the interconnections to the back-end, where the multiple output neural signals are converted into and captured as digital data. By collecting the signals digitally numerous methods of analysis through connection to specialized external electronics for multi-channel recording and digital signal processing (DSP) become readily available.

So, once more for the sake of clarity, the “front-end” device refers to the flexible  $\mu$ ECOG probes made using micro-fabrication thin-film methods and the “back-end” device refers to the external connector required to act as an intermediary circuit pathway between the small connector pads of the neural probe and an external electronic data analysis system (DAS).

### 3.2.2 FRONT-END $\mu$ ECOG PROBE DEVICE

The main design concepts and objections for  $\mu$ ECOG probes developed for my research projects are roughly equivalent to those of state-of-the-art or commercially available neural probes. The required properties and capabilities of the  $\mu$ ECOG probe design and fabrication objectives:

- Biocompatible, flexible, and durable matrix material acceptable for use in a microfabrication facility.
- Electrochemically safe metallic circuitry layer as the electrode-tissue interface.
- MEA electrode size and spacing should roughly match the average size of neurons and spacing of neurons in the functional nuclei of interest.
- Probe body made long enough to allow for slack between probe head and connector device.
- An optimized microfabrication process flow; maximizing batch yields of defect-free probes with good conductivity in the deposited metallic layer.
- Connector pads at the probe-tail sized and spaced for a compatible connection to specified zero-insertion force (ZIF) clip connector

### 3.2.3 BACK-END ZIF CONNECTOR DEVICE

A well-functioning back-end connector device is an absolutely essential part of all wired neural probe systems, for all types. Due to the passive recording being performed by this neural probe system, the required properties and capabilities of a passive back-end connector device are quite straightforward and minimal. These are those requirements, along with fabrication objectives and operational considerations for the back-end device:

- Serve as a connection between otherwise inaccessibly small connection pads and external electronic connectors.
- Enable the use of flexible, thin-film probes with a ZIF-clip type connector component.
- Hard-shell casing shape should provide labelled channel-by-channel connections for selectively connecting specific microelectrodes to external electronics.
- Internal wiring should introduce minimal additional DC resistance to the system.
- Utilize fast, cheap 3D printing prototype fabrications methods.
- Utilize software-driven design methods such as AutoCAD 3D modeling to design:
  - a. A hard-shell case capable of providing mechanical protection through strength and rigidity.
  - b. Easily assembled and disassembled when necessary.
  - c. Be re-usable and easily handled.

### 3.2.4 FRONT-END $\mu$ ECoG PROBE DESIGN SCHEMATIC

The front-end  $\mu$ ECoG probes can be divided into 3 general regions: a head, a body, and a tail. For the sake of clarity, notable features within these 3 regions have been labelled, along with other distinguishable features and a few key dimensions, and are shown in Figure 10, below.

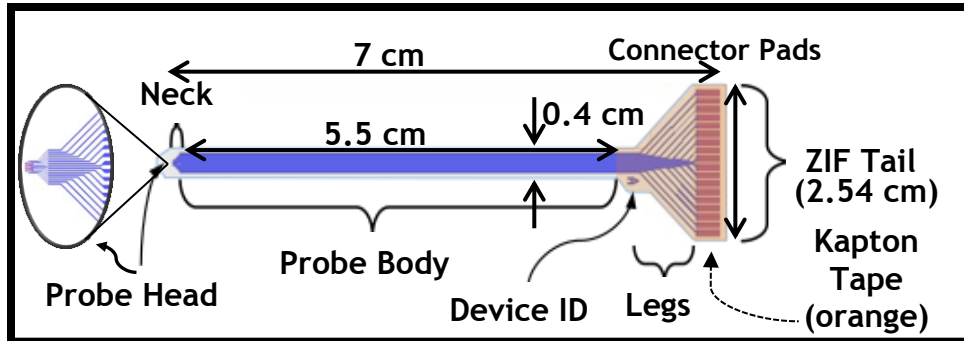


**Figure 10** – A schematic diagram of the  $\mu$ ECoG probe device. From left to right: a magnification of the probe head and neck, then the macroscopic device view showing the probe body, the device ID and finally the legs and connector pads of the ZIF tail (which has been reinforced and thickened with Kapton tape).

The probe body is approximately 5.5 cm long and 4 mm wide with 18  $70\ \mu\text{m}$  circuitry traces with  $70\ \mu\text{m}$  pitch (pitch is the centre-to-centre distance between parallel traces).

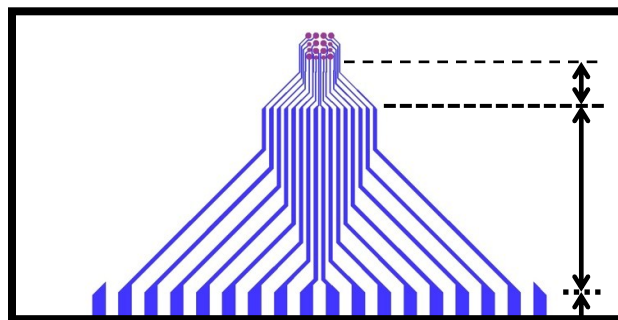


**Figure 11** – Enlarged view of the “neck” and its trace-pitch step-down pattern (pitches to probe head are:  $70\ \mu\text{m} > 20\ \mu\text{m} > 5\ \mu\text{m}$ )

Moving toward the probe head through the ‘neck’ (shown above in Figure 11), the purpose of which is to “step-up” the width and pitch of the interconnecting

metallic circuit traces so that the final trace size matches the trace width and pitch of the electrode-layouts. In Figure 11, above, at the bottom of the figure there are eighteen 70  $\mu\text{m}$  wide traces with 140  $\mu\text{m}$  pitch. The third step-up takes the signals coming from traces with width and minimum pitch 20  $\mu\text{m}$  up to the 70  $\mu\text{m}$  traces of the probe body. The second step-up performs the same task as the others but with an initial trace width and pitch of 5  $\mu\text{m}$ . As the 5  $\mu\text{m}$  traces continue into the probe head, each one will eventually connect to an electrode. (The size and the spacing of the electrodes are specifically described within the MEA layouts detailed in Section 3.3.)

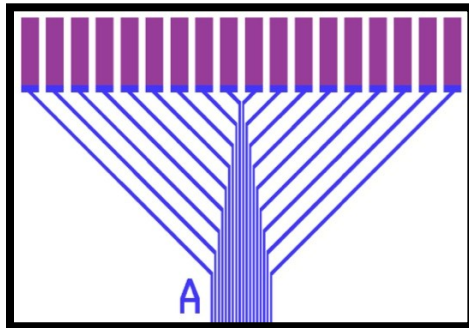


**Figure 12** – CAD image of the ZIF tail, the ‘Legs’ step-up zone, device ID ‘A’, and 18 connector pads (0.7 x 3.0 mm, 1 mm pitch).

Figure 12 shows the opposite end of the front-end probe, the connector pads of the ZIF tail. These 0.7 x 3.0 mm rectangular pads, 1 mm pitch (centre-to-centre) serve as the interface between the flexible probe and the pins in the ZIF-clip of the back-end connector. Each rectangle is connected to angled traces that converge and run parallel to each other - the ‘legs’ of the device. These ZIF tail areas must be reinforced and given the necessary thickness by the layered application of Kapton® tape to the probes backside to enable a strong, secure connection between the two neural probe system devices.

Each probe is also marked with a letter patterned into the metallic layer (see Figure 12, above) that serves as a device ID (A, B, C, D, E) for better tracking

and cataloguing of the fabricated probes. This practice can also prove quite helpful throughout the optimization process for the fabrication process flow.

### 3.2.5 FRONT-END TO BACK-END CONNECTION

In some cases, this can be accomplished by the purchase of a proprietary headstage along with the matching commercial probes - this can be very expensive and low supplies (or high demand) of probes and head-stage availability can severely restrict the rate of experimental progress.<sup>54</sup> However, it was possible to fabricate equivalent probes and a headstage connector, provided the cleanroom facilities and equipment available through either the nanoFAB facility or Ingenuity Lab.

To avoid any of the issues related with purchasing or using proprietary neural probes and headstage systems, such as Neuralynx's Nano-Z flexible  $\mu$ ECoG probe system, I utilized both of the nanoFAB's two cleanrooms and my previous experience in thin-film microfabrication processing to custom make both the front-end probe and back-end connector devices for this work.

For flexible electronic devices, a connection requiring little-to-no insertion force is needed, such as a ZIF clip, since the flexible, polymer matrix would crumple, twist, bend or otherwise deform. ZIF connection components are available in a large variety of shapes and sizes from numerous suppliers. Each clip consists of a series of pins within a casing that opens, into which the end of the probe can gently be inserted and then closes and clamps down upon the connector pads to obtain solid electrical contact. The choice of ZIF-clip will determine the maximum number of electrode channels available and whether the gold contacts within are on the bottom-contact, top-contact, or both.

The ZIF-clip component must have large enough connections so that the  $\mu$ ECoG ZIF tail can be manually inserted easily, repeatedly and attain proper



that region and increase the devices thickness locally to 0.3 mm, the thickness needed for secure contact with the pins of the ZIF-clip.

### 3.2.6 ZIF CONNECTOR HARD-SHELL CASE DESIGN

The combination of components used to create the internal circuitry of the back-end connector device needs to be housed in a case of some kind to provide a protective physical form with some structural strength for end-user ease-of-use.

The dimensions, in Figure 14 on the following page, for the hard-shell case were initially approximated and gradually adjusted as needed until eventually the largest section along each axis became 7.5 cm long by 9.5 cm wide by 0.8 cm thick. The two pieces should click together and it should be possible to connect and disconnect to two halves easily if the tolerances are adequate. Small wings and matching slots on opposing halves have been added to prevent the top half from sliding off of the bottom.

AutoCAD 3D modeling software (Autodesk Inc.; [www.autodesk.com](http://www.autodesk.com)) was used to design customized schematics of two separate pieces of a case that combined to become a hard-shell enclosure that could hold the ZIF-clip in place along with its internal wiring.

The case provides a means to fix the ZIF-clip and its numerous wires into place, securing both components while separating and organizing the wire ends in their place, keeping them easily distinguishable from each other.

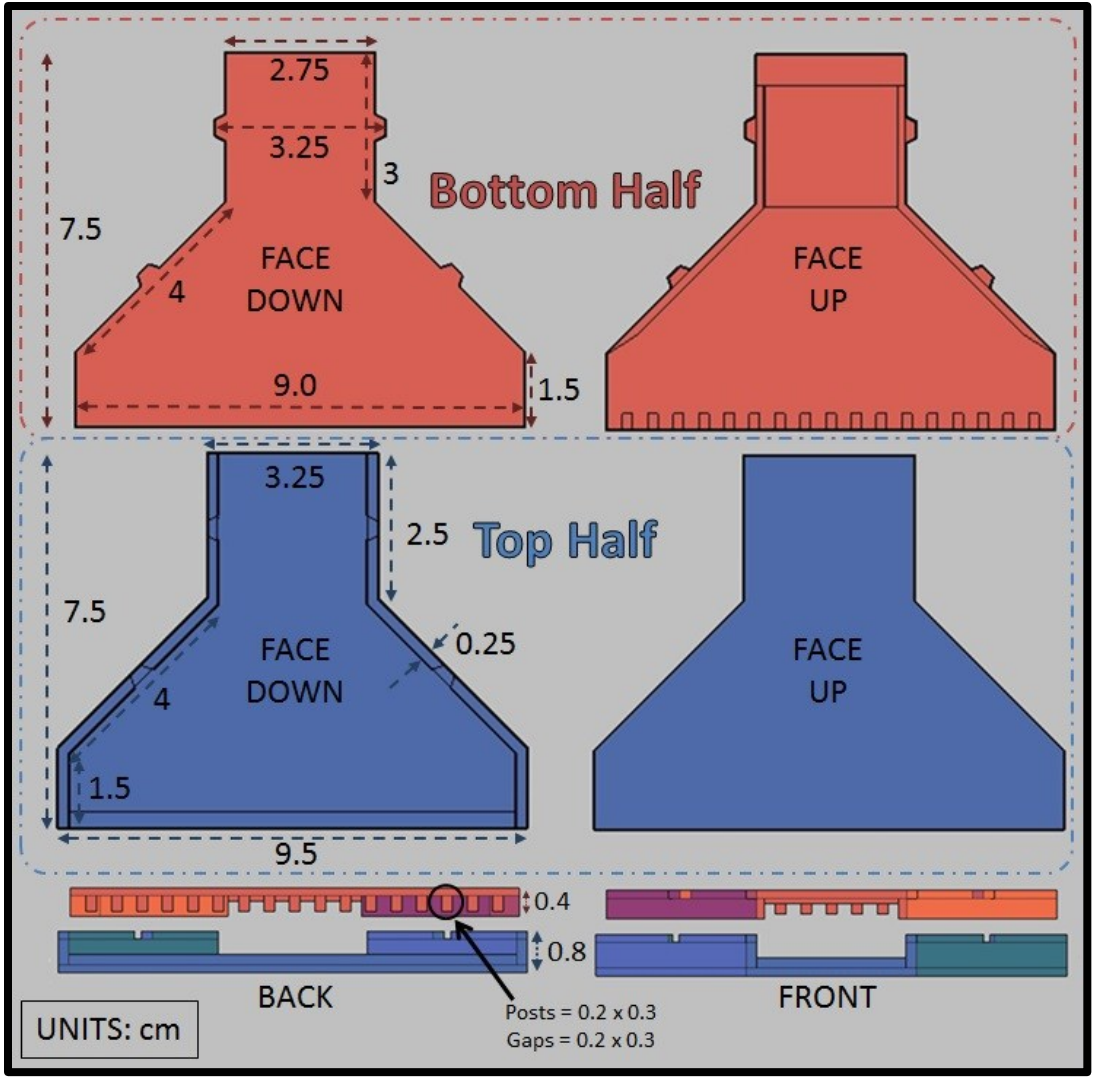


Figure 14 – 2D AutoCAD schematic of a two-piece protective, hard-shell case for the ZIF-connector.

## 3.3 - $\mu$ ECOG FRONT-END MICROELECTRODE ARRAY LAYOUTS

Electrode layouts are a key element in investigative neuroscience. When considering how to measure something across a surface using microelectrode arrays (MEAs), the main considerations are the size of, the spacing between, and the overall number of the electrodes. The objective was to design two MEA layouts that can be used to study specific neural ganglia of interest by controlling the size and spacing of the microelectrodes within the 2D array. The two MEA layouts, each with 16 microelectrodes at relevant diameters and useful spacing's, are described in detail throughout Section 3.3.

### 3.3.1 CONCEPTS BEHIND THE TWO MEA LAYOUTS

Using micrographs provided by Dr. Vladimir Rancic from Dr. Klaus Ballanyi's neuroscience research group from the U of A's Department of Physiology in the Faculty of Medicine and Dentistry, two MEA layouts for *ex vivo* tissue for use in *in vitro* electrophysiological recording experiments were designed and generated with different spatial resolutions and slight electrode size differences:

1. A high-density, small-area MEA layout to investigate into small nuclei in the brain slices of neo-natal rats such as the *locus coeruleus (LC)*. (LC shown in Figure 15.)
2. A medium-density, medium-area MEA layout to monitor the dynamics of LFPs across a nucleus in the brains of neo-natal rats such as the *ventral-medial-hypothalamus (VMH)* (shown in Figure 17), as well as to detect any nearby APs.

### 3.3.2 PHYSIOLOGICAL LAYOUT 1 - HIGH DENSITY

This layout is designed to interface with the neo-cortex and enable recording and analysis of fast AP signals from *ex vivo* samples of 3D neural networks in which there are highly-organized and functionally focused neurons that form a nucleus such as the *hippocampus* or *LC* (nuclei, ganglia, etc.).

It appears that the LC shown below in Figure 15 has a long-axis of about 330  $\mu\text{m}$  and a perpendicular short-axis approximately 270  $\mu\text{m}$  across at its maximum. It can also be roughly approximated that the average neuronal cell body diameter is around 20  $\mu\text{m}$  to 30  $\mu\text{m}$ .

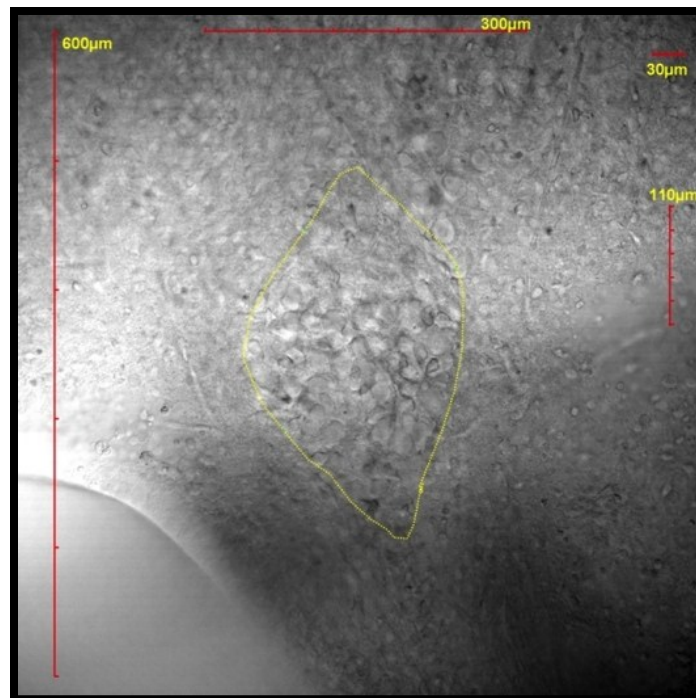


**Figure 15** – Optical micrograph of a horizontal brain slice excised from an actual neo-natal rat. Enclosed within the yellow boundary is the functional neural nucleus of interest: the *LC*. (Image provided by Vladimir Rancic of Dr. Ballanyi’s Lab.)

In this design, two electrode diameters were included to investigate the difference in signal quality between otherwise identical microelectrodes, both at sizes similar to that of the neuronal soma there are to be recording. The

microelectrodes are placed tightly so as to match the neural regions of interest, given fabrication limitations, and the diameters chosen approximate the average nerve cell body diameter. The resulting electrode layout is shown below in Figure 16.

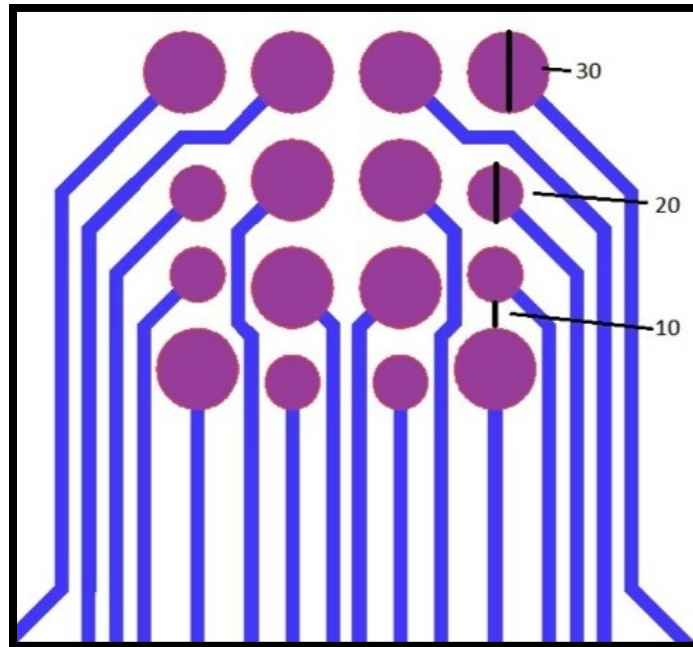


**Figure 16** – CAD design for Physiological Layout 1, the “high-density” electrode layout. Blue is insulated metal; purple regions represent the bare metal of the microelectrodes that is not insulated. (Units are in  $\mu\text{m}$ )

Specifications: 16 x (10 x 30  $\mu\text{m}$  and 6 x 20  $\mu\text{m}$  diameter, specifically) microelectrodes; as little as 10  $\mu\text{m}$  edge-to-edge spacing; 5  $\mu\text{m}$  wide interconnects running in parallel to each other at a minimum pitch of 5  $\mu\text{m}$ ; and covers an area of 150  $\mu\text{m}$  x 150  $\mu\text{m}$  with a spatial resolution ranging from 25 to 40  $\mu\text{m}$ .

This layout will be used to record both APs and LFPs (previously defined Chapter 2 Section 2.4.3).

### 3.3.3 PHYSIOLOGICAL LAYOUT 2 - MEDIUM DENSITY

A medium-density, medium-area electrode layout is intended to monitor the dynamics of wave-propagations of LFPs across a section of a medium-sized nucleus in the brains of neo-natal rats such as the *ventral-medial-hypothalamus* (VMH) as well as to detect any nearby APs.

As previously discussed in Section 2.4.3.2, LFPs are a class of low frequency signals (<300 Hz) resulting from the summation of all the various extracellular by-products from signalling activity in a specific area.<sup>23</sup> Electrodes spread across a certain surface area, all recording simultaneously, allow for the tracking of the propagation of neural oscillations within the neural circuitry of brain tissue.<sup>73</sup> Even with a reduced number of electrodes (3 out of 16 for example) recording simultaneously, the ability to track neural wave propagation still exists.

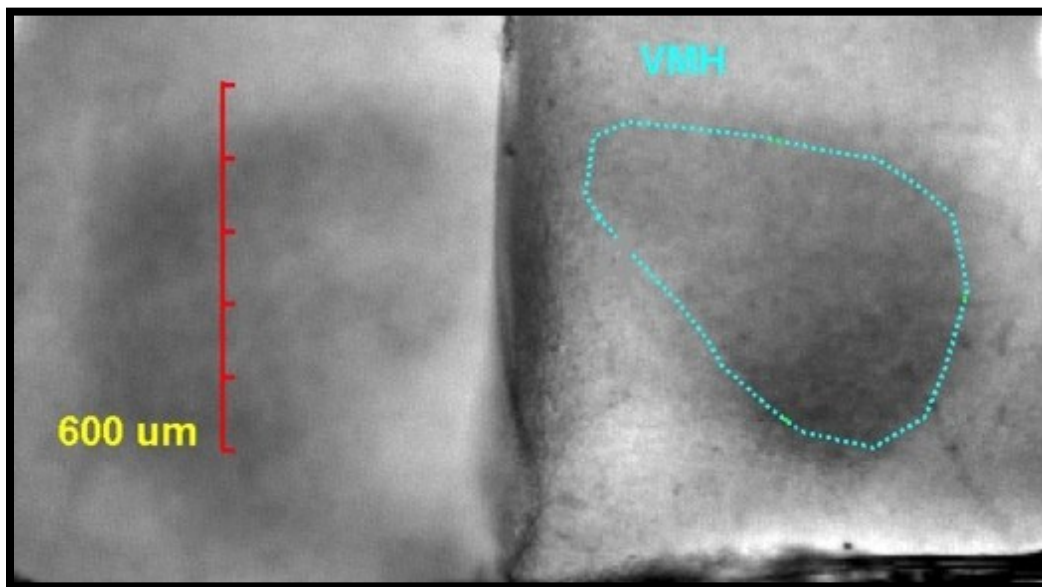


**Figure 17** – One of the neural structures of interest in neo-natal rat brain slices: the VMH.  
(Image provided by Vladimir Rancic of Dr. Ballanyi's Lab.)

In the above image Figure 17, the VMH is shown with a long-axis of 650  $\mu\text{m}$  and a perpendicular maximum width near 400  $\mu\text{m}$  and it also appears that the

average neuronal cell body diameter can be roughly approximated to be 20  $\mu\text{m}$  to 30  $\mu\text{m}$ , as with the previous micrograph. The electrode layout resulting from the desire to track LFP wave propagation as well as fast APs is shown below in Figure 18.

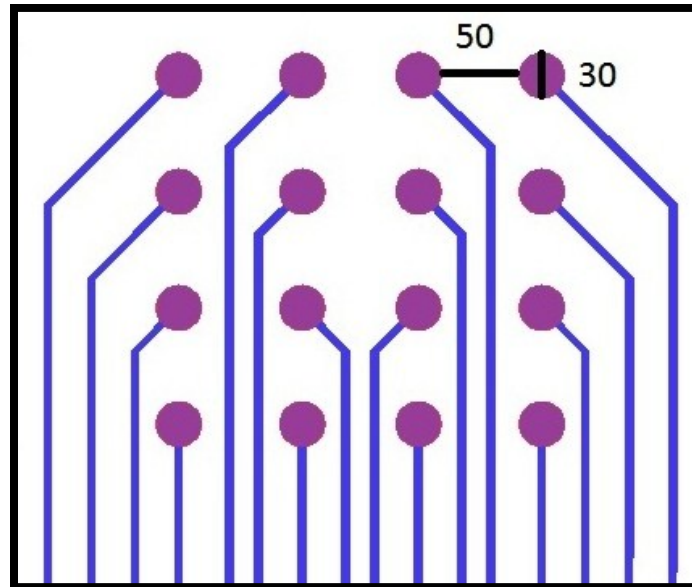


**Figure 18** – Physiological Layout 2, the “medium-density” electrode layout.  
(Units are in  $\mu\text{m}$ )

Specifications: 16 x 30  $\mu\text{m}$  diameter microelectrodes with 50  $\mu\text{m}$  spacing from edge-to-edge; 5  $\mu\text{m}$  wide interconnects running in parallel with a minimum pitch of 25  $\mu\text{m}$ ; and covers an area of 270  $\mu\text{m}$  x 270  $\mu\text{m}$  with a spatial resolution of 65 to 80  $\mu\text{m}$ .

Now that the physiological MEA layouts have been established I am going to describe the fabrication of the front-end thin-film probe device.

## **3.4 - THIN-FILM $\mu$ ECoG PROBE MICRO-FABRICATION MATERIALS AND METHODS**

These thin-film IC fabrication methods and technologies were pioneered and established by the IC industry within expensive, specially built fabrication facilities in which the laboratory space is a cleanroom environment (due to it containing few airborne particulates in the air). This section discusses the fabrication of a flexible,  $\mu$ ECoG neural probe with thin-film IC fabrication methods.

This begins with a description of the microfabrication facility used and its operational parameters. This is followed by the software-aided design and fabrication of the lithographical masks that will be used to obtain the circuitry of the flexible probe. Then a list of the required materials, chemicals, tools and equipment for the fabrication process are provided along with the suppliers when possible. The remainder of this section is made up by the details of the micro-fabrication methods process used to make the probes. These process steps are summarized with a table at the end of this section.

Now I will briefly describe the nanoFAB's cleanroom facility before carrying on as has just been laid out.

### **3.4.1 THE NANOFAB MICROFABRICATION FACILITY**

Due to the immense capital cost associated with operating a cleanroom, purchasing the equipment and keeping it running, for this work, the University of Alberta's nanoFAB facility was used for all micro-fabrication processes (two cleanrooms: a Class 1,000 (1K) and a Class 10,000 (10K)). As a high-end electronics fabrication research lab, the nanoFAB provides access to all of the necessary fabrication processes: chemical vapour deposition (CVD), physical

vapour deposition (PVD), reactive ion etching (RIE) plasma processes and lithography; and materials: Parylene-C (P-C), gold (Au), titanium (Ti).

The micro-fabrication equipment available in the nanoFAB allows the thin-film probe devices to be fabricated completely using 4” wafers. Chemical and vapour deposition processes are carried out in the 10K cleanroom while the lithographical and plasma-based processes are carried out in the 1K cleanroom.

### 3.4.2 $\mu$ ECOG PHOTOMASK FABRICATION

The photolithography mask design for patterning the entire wafer, including the multiple neural probe devices and other utility features required for the fabrication process, were all designed and drawn with Tanner LEDIT CAD. Mask blanks are 5” x 5” square pieces of fused silica glass with high optical transparency, a flat, highly polished surface to minimize light scattering, and an opaque layer of Cr uniformly deposited on one side. Using Tanner L-Edit CAD software, the maximum number of  $\mu$ ECOG devices possible to fit onto one wafer were laid out and arranged at the mask-level of the design with no scaling required.

The designs were done across multiple colour-coded layers, as needed, to assure that the masks printed for each layer are in alignment. In this two masks are needed: a base layer mask for the metallic circuitry (or “traces”), and a second mask for the VIA-well and ZIF tail contact pad etching. The masks are printed using a DWL200 Pattern Generator that selectively removes the regions of the mask with LASER ablation as specified by the CAD file. A typical pair of 5” x 5” wafer-level mask designs made in the L-Edit CAD software - shown separately (one for each lithography process step) and overlapped (or ‘in alignment’) in Figure 19, below.

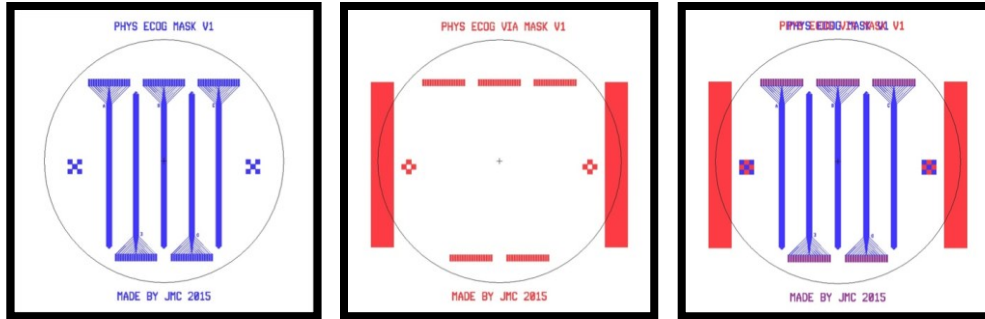


**Figure 19** – Metal pattern layer (Mask #1: left, blue); Insulated VIA-well etching layer (Mask #2: centre, red); And the combined layer stack (right, red/blue).

Mask #1 was printed such that the polygons are left behind as chrome whereas for Mask #2 the polygons are sections of Cr that have become transparent by the removal of Cr with a laser. From the central figure in Figure 19 (above), it can be seen that Mask #2 has few design-related polygonal features, in fact, only the connector pads of the ZIF tail are visible.

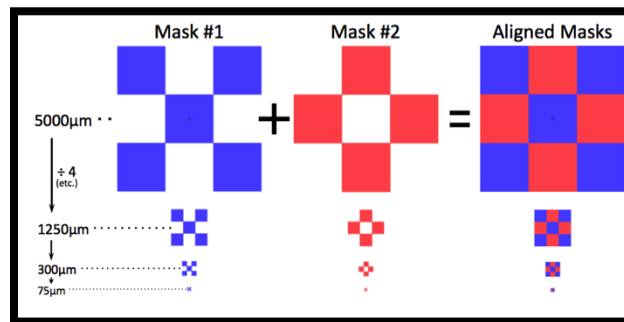


**Figure 20** – Alignment marks (repeated at various sizes) are used to accurately align Mask #2 (centre) with the metallic pattern from Mask #1 (left). Mask #1 & Mask #2 properly aligned (right).

To visually assist in the alignment process “alignment marks” are used to achieve alignment at decreasing size scales, as shown in the above figure, Figure 20. Having perfect alignment is a key aspect of having high microfabrication yields in the IC industry due with the small feature sizes and quantities of masks used for a single device. The alignment of Mask #2 with the metallic pattern made with Mask #1 is crucial.

### 3.4.3 MATERIALS AND SUPPLIERS LIST

- 4" Test Grade Silicon Wafers  
(University Wafers; [www.universitywafer.com](http://www.universitywafer.com))
- DPX-C Parylene-C Precursor  
(Specialty Coating Systems; [www.scscoatings.com](http://www.scscoatings.com))
- UHV Foil (All-Foils, Inc.; [www.allfoils.com](http://www.allfoils.com))
- 1" x 3" Plain Microscopy Slides (Corning; [www.corning.com](http://www.corning.com))
- Polyimide Kapton® Tape (Cole-Parmer; [www.coleparmer.com](http://www.coleparmer.com))
- Titanium (99.995%) Sputtering Target  
(Kurt J. Lesker Company; [www.lesker.com](http://www.lesker.com))
- Gold (99.999%) Sputtering Target  
(Kurt J. Lesker Company; [www.lesker.com](http://www.lesker.com))
- 6" Pyrex® Dishes and Covers (Fisher Scientific; [www.fishersci.ca](http://www.fishersci.ca))
- Conical Centrifuge Tubes (15 mL)  
(ThermoScientific; [www.thermofisher.com](http://www.thermofisher.com))
- AZ® 5214-E Image Reversal Photoresist  
(MicroChemicals; [www.microchemicals.com](http://www.microchemicals.com))
- MicroPosit™ MF 319 Developer Solution  
(Microfabrication Materials Technologies; [www.micromaterialstech.com](http://www.micromaterialstech.com))
- HPR 506 Positive Photoresist (Fujifilm Canada, Inc.; [www.fujifilm.ca](http://www.fujifilm.ca))
- MicroPosit™ M354 Developer Solution  
(Microfabrication Materials Technologies; [www.micromaterialstech.com](http://www.micromaterialstech.com))
- Acetone, ACS Grade (Fisher Chemical; [www.fishersci.ca](http://www.fishersci.ca))
- Isopropyl Alcohol, 70% w/w (Fisher Chemical; [www.fishersci.ca](http://www.fishersci.ca))
- Milli-Q® De-Ionized Water (EMD Millipore; [www.emdmillipore.com](http://www.emdmillipore.com))
- High-Purity Oxygen Gas (Praxair; [www.praxair.com](http://www.praxair.com))
- Ultra High-Purity Nitrogen Gas (Praxair; [www.praxair.com](http://www.praxair.com))
- DWL2000 Pattern Generator (Heidelberg Instruments; [www.himt.de](http://www.himt.de))

- L-Edit CAD Software (Tanner Research; [www.tanner.com](http://www.tanner.com))
- PDS 2010 Parylene Deposition System  
(Specialty Coating Systems, Inc.; [www.scscoatings.com](http://www.scscoatings.com))
- Flexi-cool Cold Trap (SP Scientific; [www.spscientific.com](http://www.spscientific.com))
- VICON Weigh-Scale (Acculab; [www.acculab.ca](http://www.acculab.ca))
- “Bob” Sputtering System:
- Baratron® Capacitance Manometer (MKS Instruments; [www.mksinst.com](http://www.mksinst.com))
- I-100-K Glass Ion Gauge (Duniway Stockroom Corp.; [www.duniway.com](http://www.duniway.com))
- USP540-1U Speed Control Unit  
(Oriental Motor Co. Ltd.; [www.orientalmotor.com](http://www.orientalmotor.com))
- MDX 500 Power Supply (Advanced Energy; [www.advanced-energy.com](http://www.advanced-energy.com))
- Type 247 4 Channel Readout Controller  
(MKS Instruments; [www.mksinst.com](http://www.mksinst.com))
- Multi-Gauge Controller (Kurt J. Lesker Company; [www.lesker.com](http://www.lesker.com))
- CTI-Cryogenics Cryo Pump  
(Oxford Instruments; [www.oxford-instruments.com](http://www.oxford-instruments.com))
- 114 True RMS Multi-Meter (Fluke; [www.fluke.com](http://www.fluke.com))
- MicroEtch Reactive Ion Etcher  
(PlasmaLab; [www.oxford-instruments.com](http://www.oxford-instruments.com))
- ENI Model ACG-3 Power System  
(Electronics & Innovation Ltd.; [www.eandiltd.com](http://www.eandiltd.com))
- Optical Lithography System:
- 5110-C-T Photoresist Spinner (Solitec; [www.solitec-wp.com](http://www.solitec-wp.com))
- SBS-200 Vacuum-Bake Hot-Plate (Solitec; [www.solitec-wp.com](http://www.solitec-wp.com))
- ABM Tabletop Contact-Mode Mask Aligner  
(ABM, Inc.; [www.abmusainc.com](http://www.abmusainc.com))
- 2105C2 Illumination Controller (UV 365 nm/405 nm)  
(ABM, Inc.; [www.abmusainc.com](http://www.abmusainc.com))
- Branson 5510 Ultrasound Bath (Emerson; [www.emerson.com](http://www.emerson.com))

### 3.4.4 $\mu$ ECoG DEVICE FABRICATION PROCESS FLOW

This section covers the clean-room micro-fabrication procedures used to get the front-end thin-film  $\mu$ ECoG devices used in experiments throughout the following chapters. The optimized process flow for the micro-fabrication of the flexible  $\mu$ ECoG probe devices is provided step-wise with detailed descriptions providing all the information needed for the replication of the process. Following this, Table 2 (and the accompanying legend, Table 3,) provides a visual summary of the process flow, containing step-wise cross-sectional wafer illustrations and comments for each step.

Flexible, thin-film  $\mu$ ECoG probes were fabricated in batches of 4 on pristine, test-grade 4" Si wafer substrates using a variety of thin-film processing methods from the microelectronics fabrication industry. All protocols were carried out following a standard operating procedure (SOP) from the nanoFAB and adjusted it as required to optimize to process:

#### 1. PARYLENE-C BASE LAYER DEPOSITION

The first process deposited a uniform, pinhole free base-layer of P-C using a Parylene Deposition System: the PDS 2010. Approximately 50 g of DPX-C precursor was measured into a foil weigh-boat and loaded the PDS 2010 and the system was initialized with the following parameters: furnace set-point temperature at 690°C, the chamber set-point temperature at 135°C, the vaporizer set-point temperature at 175°C, and a base vacuum pressure set-point value of 35 vacuum units (990 units at atmosphere). Once the base P-C layer had been deposited and the wafers were carefully removed from the PDS 2010 deposition platform, each wafer had the P-C surface activated through a brief exposure to oxygen plasma generated within a RIE.

## 2. OXYGEN-PLASMA SURFACE ACTIVATION

Wafers were loaded one at a time into the MicroEtch RIE vacuum chamber and exposed to the oxygen plasma “surface activation” recipe (30 s, 25 sccm O<sub>2</sub>, 500 mTorr and 22.5 W<sub>RF</sub>). Once “activated,” the P-C surface attained a meta-stable hydrophilic state required for the upcoming photoresist coating process, which was carried out immediately after each wafer was activated.

## 3. PHOTORESIST SPIN-COATING AND SOFT-BAKING

Immediately following the surface activation, each of the surface-activated, P-C base-coated wafers were taken, one at a time, placed symmetrically onto the vacuum chuck of the spin-coater and vacuum sealed. Around 5 mL of AZ 5214-E IR PR was poured into the centre of the wafer. The PR on the wafer was then spin-coated evenly across the entire wafer surface with an initial 10 s “spreading” phase at 500 RPM, followed by 40 s “spinning” phase at 4000 RPM to remove all excess PR, leaving a uniformly 1.4 μm thick layer of PR. The spin-coated wafers were then soft-baked for 90 s at 88°C and left to rest and rehydrate for 15 min. This process was repeated until all 4 wafers were resting and rehydrating.

## 4. AZ 5214E PHOTORESIST PATTERNING

Using a table-top contact-mode mask aligner, Mask #1 (containing the metal circuitry patterns for the probe), was loaded chrome-side down onto the lid of the mask aligner and secured with a vacuum seal to prevent any shifting from occurring. The wafers were loaded one at a time onto the aligner’s the self-levelling vacuum chuck which, once holding the wafer firmly in place with vacuum, was then levelled and carefully brought up until the PR layer was in uniform, soft-contact with the photomask. To maximize resolution and prevent loss of small features, the vacuum chuck holding the wafer down was disengaged and another vacuum was used to

press the wafer into hard-contact with Mask #1. Once in hard-contact, each wafer was exposed to a UV light source (65.6 mW/cm<sup>2</sup>) for 9 s.

#### 5. IMAGE REVERSAL OF AZ 5214E

Following this pattern-exposure the wafer was removed from the mask aligner by following the loading procedure in reverse, hard-baked for 27 s at 108°C, and allowed to rest and rehydrate for 15 min. Once rehydrated, Mask #1 was removed from the aligner, each wafer was then “flood exposed” for 60 s by the same UV source, completing the IR of AZ 5214-E.

#### 6. PHOTORESIST PATTERN DEVELOPMENT

Developed by complete immersion in MF 319 developer gently sloshed around the container for 20 to 25 s and rinsed thoroughly with DI to quench the development reaction, the wafers were then blown dry, gently, with nitrogen gas. The lithographic patterns developed in the PR were then inspected under microscope to assess the pattern transfer and development quality - at this point any development that fails a visual inspection was cleaned off with acetone, IPA and DI and the process was repeated from the surface activation step, Step 2.

#### 7. TITANIUM-GOLD SPUTTERING

To acquire the metallic components of the device a vacuum deposition system was used - the sputtering system named “Bob” is capable of holding up to six 4” wafers and one analogue test-slide on its rotating deposition platform. Bob can also load up to three different target materials into each of the three sputtering guns available. Base chamber vacuum pressure near  $8 \times 10^{-7}$  Torr was achieved by using a roughing-pump followed by 90 min of cryo-pumping. Argon gas was added to the chamber for deposition to obtain a chamber pressure of 7 mTorr. Once down to the required vacuum level, the platform holding the samples was rotated slowly (at about 10 RPM) to more uniformly deposit the sputtered target

metal onto the wafers. The first layer was the adhesion layer of Ti and was deposited at a power of 300 W and a chamber pressure of 7 mTorr. Ti in this system typically deposited at an average 7.1 nm/min, requiring only 75 s to acquire an approximately 10 nm thick adhesion layer. The Au layer was sputtered immediately after the Ti adhesion layer by switching the sputtering gun from Ti to Au and reducing the supplied power to 75 W. With Bob the average deposition rate of gold was 6.6 nm/min. 18 min 11 s of deposition time was calculated to deposit an average thickness of 120 nm. The wafers were unloaded and immediately placed into an airtight carrier until the lift-off procedure was carried out.

#### 8. LIFT-OFF

The lift-off process began by immersing a metallized wafer into acetone in a 6" x 1" Pyrex® covered-dish for several hours to let the acetone soak into the underlying PR layer and dissolve it. This was done for 4 hours or longer if desired. (N.B. so long as the acetone level remained above the wafer surface there were no added problems, however the metallic layer was ruined if the PR base is solvated and evaporated away, leaving the excess gold stuck directly to the wafer. When that happened removal was practically impossible.) Once well soaked, the excess metal was broken from the desired metallic pattern by a couple short bursts of ultrasonification (2 x 0.5 s) in a Branson 5510 ultrasound bath. Loose metallic pieces were then sprayed off of the wafer with acetone to prevent unwanted short-circuits and the excess acetone was poured out of the Pyrex dish, filtered and reused for rinsing. Fresh acetone was used to re-submerge the partially-cleared wafer in the Pyrex dish. Due to the mass-transport limited dissolution of the PR, the wafer may require an additional hour or two to migrate to the hardest to reach spots. This is followed by another quick burst of sonication, as before, and a thorough rinsing of the wafer with reclaimed acetone to remove any remaining PR or metallic

flakes. Optical microscopy inspection was performed to confirm that the metal had been removed as desired. Wafers were thoroughly cleaned and rinsed with acetone, IPA, and DI and dried gently with N<sub>2</sub> gas.

9. INSULATING PARYLENE-C LAYER DEPOSITION

A batch of wafers with exposed gold circuitry was then loaded into the PDS 2010 to insulate the metal with a thin 2 μm layer of P-C, which was, reportedly, as thin as possible to avoid any pinhole defects. Re-used the operational parameters from Step 1 and 4.5 g of DPX precursor was loaded in the weigh boat to obtain an insulating layer thickness around 2 μm.

10. OXYGEN-PLASMA SURFACE ACTIVATION

The surface of each wafer P-C insulated wafer was activated with oxygen plasma as previously detailed in Step 2.

11. SPIN COATING AND SOFT-BAKING OF HPR 506

As in Step 3, each wafer was immediately spin-coated once the surface was “activated.” Spin-coating was done as in Step 3 but with 5 mL HPR 506 as PR, resulting in a 2.5 μm thick PR layer that was then soft-baked for 90 s at 115°C. Following the soft-bake the wafers rested for 15 min to rehydrate.

12. MASK ALIGNMENT AND VIA-WELL EXPOSURE

While rehydrating for 15 min, Mask #2 was loaded on the mask aligner with the correct orientation to match the wafer being aligned with. To get the best alignment possible, I started with the naked eye and found it greatly assisted in the following alignment steps. (See Section 3.4.2 for examples of the alignment marks used.) Closed-circuit displays with magnifying lenses were used for the alignment process: the largest alignment mark was first matched up on both sides, followed by the next largest marks on both sides, etc., until all the masks alignment marks were properly aligned with the patterned wafer below. Once confident that the alignment was

good, UV exposure for 3.7 s activated the photochemistry of the HPR 506 and the wafer was developed in MF 354 for 20 to 25 s, rinsed with DI and inspected under microscope for visual confirmation of the PR development.

### 13. OXYGEN-PLASMA VIA-WELL ETCHING

Having properly developed the PR layer with proper alignment of the VIA-wells with the electrodes, a previously tested oxygen-plasma recipe was used to etch through the exposed P-C insulating layer at a rate of  $545 \pm 53$  nm/min. Having measured the P-C insulating layer thickness to be  $25 \pm 0.03$   $\mu\text{m}$  by surface profilometry, an initial etch time 5 min was calculated. Once each etch was completed, the electrodes and connector pads were inspected visually under microscope. The complete loss of P-C was used as the end-point determining method. In this fashion only the desired locations, the 20 or 30  $\mu\text{m}$  microelectrode VIA-wells and ZIF-tail connector pads for the back-end connector were routinely inspected for degree of completeness.

### 14. DEVICE LAYER REMOVAL

Fully micro-fabricated wafers, each with 5 devices on its surface, were then taken with a wafer carriage out of the cleanroom environments into the finishing space. The device layer was removed as a whole, single sheet from the wafer by carefully cutting under the entire P-C sandwich with a straight edge razor blade at an angle nearly parallel to the wafer but also keeping in tight contact with the flat wafers edge. The razor was always positioned so that, when viewed from above, it always cut into the layer from the outside and not from underneath and within. When done successfully the wafer-shaped sheet of P-C containing the  $\mu\text{ECoG}$  devices were processed further and the wafers were processed for reuse.

15. CUT OUT PROBE BODIES FROM DEVICE LAYER

To separate the layer into the individual probe devices, a cutting board, an X-acto knife (or straight-edge razor) and a transparent straight-edge ruler were used to separate each wafer-sheet into 5 individual devices. The probe bodies were cut to match their final shape with the same careful procedure X-acto knife procedure.

16. PREPARE FOR ZIF CONNECTOR

The ZIF tail, legs and a portion of probe body were reinforced and thickened to 0.3 mm using carefully placed Kapton® tape. Once at the required thickness, the ZIF tail was cut carefully to a width of 19 mm; along the long-edge of the ZIF tail was cut down to leave 0.5 - 1 mm of P-C and Kapton® protruding past the connector pad edges.

17. DEVICE STORAGE

The devices needed to be stored in an organized and clean fashion. 15 mL conical centrifuge tubes were used because they met these criteria. Ideally, a planar container or wider-mouthed tube would have been better because the ZIF tails required being curled slightly to fit into the vessel, although this had no apparent impact on the performance of the  $\mu$ ECoG devices. The lids and sides of the storage containers were labelled accurately to match the Batch #, Wafer # and Device ID for each probe that was fabricated.

**Table 2 – Step-by-Step Fabrication Process Flow Summary with X-Sectional Schematics**

#	Cross-Sectional Schematic	Description
-		Clean 4" silicon wafer
1		CVD of Parylene-C base layer (25 μm)
2		RIE 30 s O <sub>2</sub> plasma activation
3		AZ5214e spun & baked 88°C for 90 s
4		15 min rehyd'n – 9 s Mask #1 UV exposure
5a		Image reversal bake at 108°C for 27 s
5b		15 min rehyd'n – 60 s maskless UV exposure
6a		Develop in MF 319 solution for 20-25 s
6b		Clean with acetone, IPA, DI and dry w/ N <sub>2</sub>
7		PVD of Ti (10 nm) and Au (120 nm)
8		Lift-off with acetone – clean and dry
9		CVD insulating Parylene-C layer (2 μm)
10		RIE 30 s O <sub>2</sub> plasma surface activation
11		HPR506 spun & baked for 90 s at 115°C
12a		15 min rehydration - Mask #2 alignment
12b		2.7 s Mask #2 UV exposure
12c		Develop in M354 solution for 20-25 s
13a		RIE O <sub>2</sub> plasma etch electrode-wells
13b		Acetone, IPA and DI rinse and dry with N <sub>2</sub>
14		Separate device-layer using razorblade
15		Separate and shape into individual devices
16		Thicken ZIF tail with Kapton – cut to size
17		Store in 15 mL centrifuge tubes

**Table 3 – Material Legend for the Fabrication Process**

Fabrication Process Material Legend	
Silicon Wafer	
Parylene-C Layers	
AZ5214e or HPR506 Photoresist	
Cr on Quartz Photomask	
Au w/ Ti Adhesion Layer	

## **3.5 - ZIF CONNECTOR DEVICE FABRICATION AND ASSEMBLY**

As established early on with the signal-flow schematics, the back-end device serves as an intermediary connection between the neural probe device and an electronic DAS. In Section 3.5 I will cover the fabrication and assembly of the resulting back-end device: the ZIF connector.

The back-end ZIF connector device consists of 3 main components:

1. Wiring and exposed wire-ends to enable connection to external electronics;
2. A part that connects to the ZIF tail of the flexible neural probe body;
3. A protective, hard-shell case that spreads the wire connections apart and contains and holds the internal circuitry in place.

Once the various components and their purposes have been developed upon, the fabrication and assembly of the back-end ZIF connector device are discussed. This includes a very brief overview of the fabrication methods and the final assembly process of the back-end device ZIF connector.

### **3.5.1 PROTOTYPING A BACK-END HARD-SHELL CASE**

The hard-shell case designed to hold and protect the ZIF connector's internal circuitry was done using AutoCAD 3D modelling software programs (Autodesk, Inc.; [www.autodesk.com](http://www.autodesk.com)). The object design files were not immediately ready to be transferred into the MakerBot 3D printer software (MakerBot Industries, LLC; [www.makerbot.com](http://www.makerbot.com)) from AutoCAD, as shown in Figure 21, and a few steps needed to be taken before printing could commence.

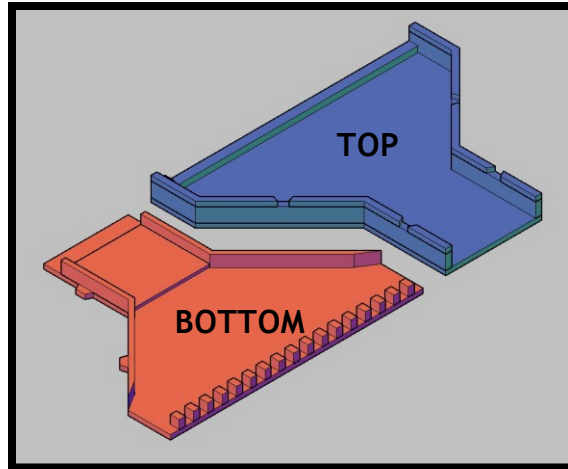


**Figure 21** – AutoCAD 3D Rendering of the bottom-half (red) and top-half (blue) of the hard-shell/protective-case.

First, the 3D CAD file was imported into Meshmixer 3D printer software (Autodesk, Inc.; [www.autodesk.com](http://www.autodesk.com)) - software that allows some small changes to be made to the CAD file to make it more “3D printer friendly.” Once these subtle tweaks to the design were made, the new 3D model file was imported into the MakerBot 3D print software and was printed. The hard-shell case prototype designs were printed out of MakerBot ‘True Color’ poly(L-lactic acid) (PLLA) filament material designed for the 5<sup>th</sup> generation MakerBot Replicator+ 3D printer that was used (MakerBot Industries, LLC; [www.makerbot.com](http://www.makerbot.com)).

By using a 3D printer, the prototyping process was rapid and software made it simple to make necessary fine-tuning adjustments when the parts didn’t quite meet desired tolerances on the first try. Even with very subtle curling the printed housings can bow-up, causing loss of shape, changing the dimensional tolerances and preventing the top and bottom halves from ‘clicking’ together as they were designed too. To prevent the base of the shell from curling slightly off of the printing platform (due to thermal shrinkage along the axis of hot, extruded polymer as it cools and contracts), multiple ‘utility-discs’ were strategically placed around the halves of the device body, as shown in Figure 22.

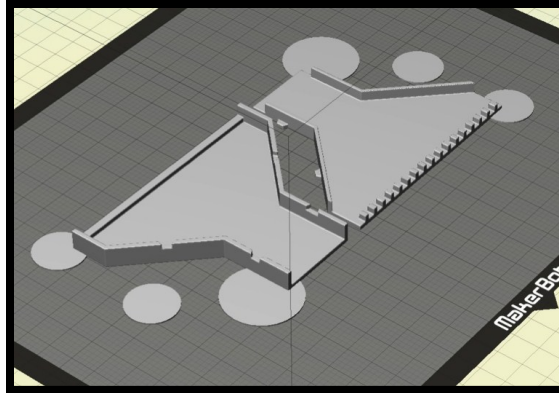


**Figure 22** – The connector housing CAD layout showing a 3D model of the top and bottom halves along with necessary utility-discs, visually indicating the MakerBot® 3D printer’s input data, on a 1 cm x 1 cm grid that represents the physical printing area available.

After a few iterations, each with some slight changes, either to the CAD design or through the addition of ‘utility discs,’ whatever was needed to obtain a curve-free hard-shell ZIF connector case. Figure 23, below shows an early prototype of the printed shell with a Canadian dime as a size reference.



**Figure 23** – An early prototype ZIF connector hard-shell case with a dime for scale.

Eventually, through trial and error, a usable hard-shell case printed properly and no additional hard-shell cases have needed to be printed since the prototype functioned exactly as desired.

### 3.5.2 PRE-ASSEMBLY PROCESSES: ZIF CONNECTOR

The ZIF connector I chose was an 18 channel Molex® with 1 mm separation between the each channel's gold-copper connector pad (Digi-Key Electronics; [www.digikey.ca](http://www.digikey.ca)). The 18 channels of the ZIF-clip were pre-soldered to 18 wires of alternating colour prior to their delivery. Due to the difficulty in avoiding short circuits from forming between neighbouring channels, only 1 mm apart, this vital task was outsourced to an employee at Digi-Key known through Richard Hull. (Thanks again Richard!)

Doing so resulted in obtaining a very high quality product with excellent soldered connections between the ZIF-clip's back-side pins and the wires. Once soldering was completed, the joints and a portion of both the ZIF-clip and the wires were enveloped in epoxy resin to prevent unwanted bending, cracking and failure of the soldered connections. (See Figure 24, below)

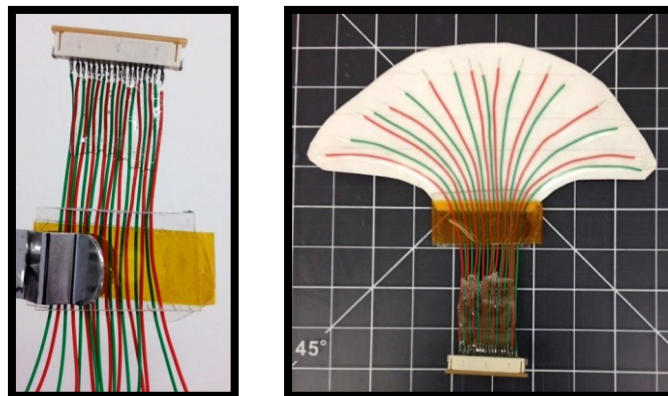


**Figure 24** – The wired ZIF-clip, freshly encapsulated with epoxy (L) and the same connector 24 to 48h later being prepared for placement into the 3D printed housing (R).

Epoxy resin was applied cautiously so as not to glue the ZIF-clip shut but generously enough to engulf from just the very the backside of the wired-ZIF clip to about 3 cm along the wires. After 24 hours the epoxy resin was fully cured and the ZIF could be wired prior to mounting it into the hard-shell case. Those ZIF-clips with wires embedded in cured epoxied had the wires carefully

separated, fanned out and taped onto a sheet of paper, securing them until needed for the assembly process, as shown in Figure 24.

### 3.5.3 BACK-END ZIF CONNECTOR DEVICE ASSEMBLY

In this section I provide an overview of the final assembly of the back-end ZIF connector device. Now that the various components and their purposes have been developed upon, this section covers the next steps: the fabrication and assembly of the back-end device used to interface between the small connection-pads of the flexible, thin-film probe and the larger-scale connections required by most electronic systems, the ZIF connector.

The narrow front-side of the case's bottom-half was designed to house the ZIF-clip with its epoxied wires stretching out and separating toward the back-side of the case. Once the proper alignment and spacing of the ZIF-clip was established (i.e. centred, squared, and with mobility to open and close), strong double-sided Kapton® tape was used to hold the clip securely in place inside the hard-shell casing.

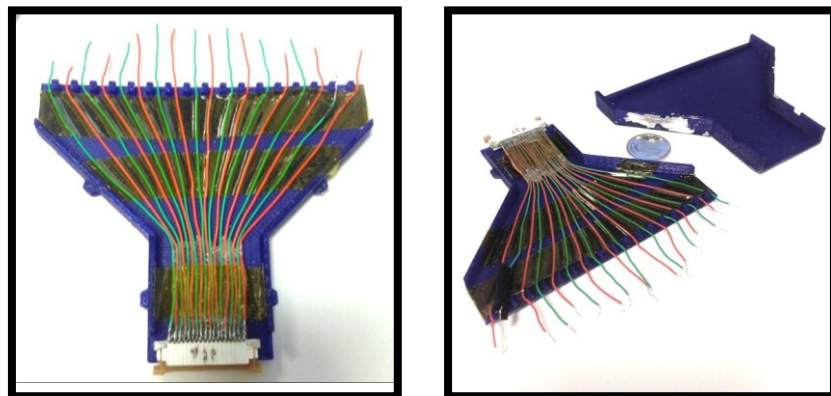


**Figure 25** – On the left, the wired ZIF secured to the topside of the housing's bottom-half. On the right, a perspective angle photo of the same bottom half along with its counterpart with a dime included for scale.

The next step was separating each wire in the correct order from one side to the other across the wide back-side of the bottom-half of the case, spreading

them as far apart as possible so that no wires criss-crossed, and then fixing them into place on the bottom-half of the case with single sided Kapton® tape, as shown in Figure 25, above.

Once the prototype housing was printed and wired satisfactorily, the wired half of the ZIF connector housing and the other are joined snugly together, assembled into the final ZIF connector device. To completely eliminate or at least reduce electromagnetic interference during experimental use the ZIF connector's hard-shell casing was wrapped tightly with aluminum foil held in place with tape - shown in Figure 26, below.

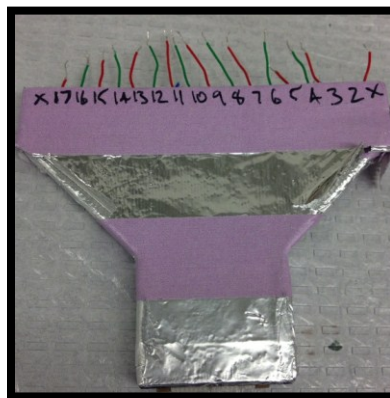


**Figure 26** – An EMR noise resistant ZIF connector device – fully assembled and ready for experimental use.

The electrode channels were carefully labelled with #'s 2 through 17 on both the front- and back-side of the now completed ZIF connector. The outermost channels on either side of the device (channels 1 and 18) were not used in these designs of the probe head and served no purpose for my experiments, although future designs could easily incorporate the 2 channels without requiring a new ZIF connector device to be designed and built.

## **3.6 - DEVICE INSPECTION AND CHARACTERIZATION**

Although there are some characterizations that take place after the fabrication process, the real secret to success when micro-fabricating devices is to ensure that each process step receives a good quality wafer from the previous step and that wafer quality is maintained through each process and into the next. As a result of this mentality, characterization methods are used between specific process steps to make quantitative quality assessments based on expectations either from calculations or previous experiments. This section covers the methods used and summarizes the resulting data.

To enable these tests without damaging or contaminating a wafer, “test-slides” that have been partially masked with multiple lines of Kapton® tape were processed along with each batch. Once each deposition process was completed, its test-slide was characterized with at least one of the follow methods: A 4-point probe to obtain thin-film metallic electrical properties: sheet resistance and resistivity; optical microscopy was used multiple times: after lithography to confirm good alignment or proper pattern development prior to etching or sputtering processes, and at the end of fabrication, prior to the removal of the device layer from its substrate; and contact profilometry to measure the step-heights of the deposited layers.

The fully assembled ZIF connector device had each channel’s pathway resistance measured with a multi-meter and the resulting data is summarized.

### **3.6.1 MICROFABRICATED DEVICE FABRICATION PROCESS QUALITY CHARACTERIZATION**

The characterization results to follow are those from the optical inspections, mid-process fabrication process, then the layer thicknesses measured by

contact profilometry for P-C base and insulating layers followed by the Au-Ti metallic layer. The fully assembled back-end ZIF connector device channel pathway's each had their resistance measured with a multi-meter and the results are summarized.

Finally, the measured and calculated batch yields are shown visually and are given in percentage values.

### 3.6.1.1 MID-PROCESS VISUAL INSPECTION

Throughout the fabrication process wafers were frequently inspected before or after a process step - especially before taking an irreversible step. The process flow has been designed and optimized for high yields but only by doing quick visual checks on developed PR layers can these yield rates be achieved. An example of a poorly executed lithographical process and an example of a properly executed one are shown below in Figure 27.

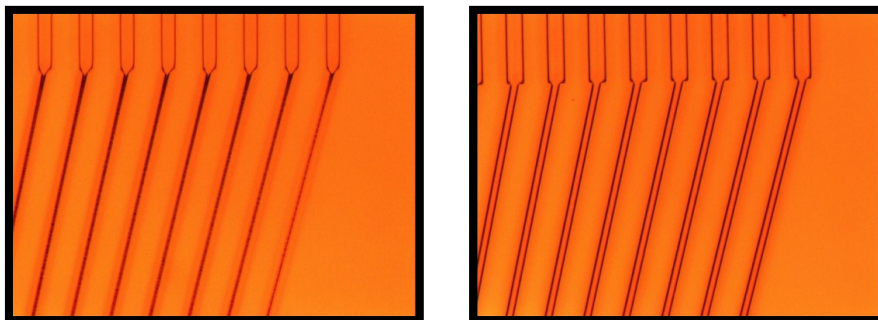


**Figure 27** – Photos post lithography patterning process showing good (right) and bad (left) development.

At this point no permanent/irreversible change has occurred yet; the poorly patterned wafer was cleaned and dried as usual and the lithography process was repeated from the surface activation step in the fabrication process flow until successful. Optical micrographs were taken once the fabrication process was completed.

### 3.6.1.2 DEPOSITED PARYLENE-C LAYER THICKNESSES

Although theoretical thickness values of each material layer were calculated prior to each process based on expected deposition or estimated etching rates, contact profilometry was utilized to measure the actual thickness of the deposited layers. Measuring across the ‘steps’ created by un-masking the test-slides, performed contact profilometry using operational parameters of: 1000  $\mu\text{m}$  scan length; 50  $\mu\text{m/s}$  scan rate; and 14.4 mg stylus force.

The resulting thickness data has been averaged and summarized in Table 4.

**Table 4 – Average Parylene-C Deposition Layer Thickness**

Batch #	Fabrication Process Stage	Precursor Used	Target Thickness	Wafer Placement	Wafer #	Measured Thickness
		g	$\mu\text{m}$		W	$\mu\text{m}$
1	Base Support Layer	50.005	25	Upper Shelf	1, 2	24.7 $\pm$ 0.1
				Lower Shelf	3, 4	23.1 $\pm$ 0.2
1	Top Insulating Layer	4.205	2	Upper Shelf	-	2.3 $\pm$ 0.2
				Lower Shelf	-	N/A
1	Post Electrode-Well Etching	-	-	Upper Shelf	-	1.8 $\pm$ 0.1
				Lower Shelf	-	N/A
2	Base Support Layer	49.990	25	Upper Shelf	5, 6	24.7 $\pm$ 0.2
				Lower Shelf	7, 8	22.8 $\pm$ 0.1
2	Top Insulating Layer	4.514	2	Upper Shelf	7, 8	2.52 $\pm$ 0.03
				Lower Shelf	5, 6	2.52 $\pm$ 0.04
2	Post Electrode-Well Etching	-	-	Upper Shelf	-	1.92 $\pm$ 0.03
				Lower Shelf	-	2.00 $\pm$ 0.03

Obtaining the same exact P-C layer thickness from one batch to the next can be challenging, but the differences between these batches were negligible from a practical perspective.

### 3.6.1.3 PARYLENE-C ETCH RATE DETERMINATION

To obtain actual etching rates, as shown in Table 5, below, the change in thickness of the insulating layer of P-C was measured after 1 min of exposure to the oxygen-plasma etching recipe. Using this recipe (100 sccm O<sub>2</sub>(g), 150 mTorr, 200 W @ 13.56 MHz RF), the average etch rate measured was 545 ± 43 nm/min.

**Table 5** – Parylene-C O<sub>2</sub> Etch Rates as Calculated

Source	Thickness Before Etching (μm)	Thickness After Etching (μm)	Etch Time (min)	Rate (nm/min)
Batch 1	2.3 ± 0.2	1.8 ± 0.1	1	504
Batch 2a	2.52 ± 0.03	1.92 ± 0.03	1	605
Batch 2b	2.52 ± 0.04	1.99 ± 0.03	1	527
Average	2.45 ± 0.07	1.90 ± 0.05	1	545 ± 0.04

This was much faster than the literature value<sup>21</sup>: 200 nm/min. Possibly because their recipe used a lower O<sub>2</sub> flow rate and their power supply frequency was about 500 times slower. Despite this discrepancy with other P-C oxygen-plasma etching recipes in the literature and their related etching rates, the etching of P-C was relatively well controlled from wafer to wafer and batch to batch. The RIE equipment itself can impact the etching rate and its uniformity across the wafer surface. In the case of the fabrication of these devices, the centre of the wafer was etched at a slower rate than the edges, which led to some of the features around the exterior being slightly over-etched. In future P-C etching processes it may be worthwhile to experiment with the plasma recipe parameters to see if a slower etch rate can be achieved and whether this makes a difference with respect to the uniformity of the etching.

3.6.1.4 PHYSICAL VAPOR DEPOSITION OF THE AU-TI CONDUCTING CIRCUITRY LAYERS

Although theoretical thickness values of each material layer were calculated prior to each process based on expected deposition or estimated etching rates, contact profilometry was utilized to measure the actual thickness of the deposited layers. Measuring across the ‘steps’ created by un-masking the test-slides, performed contact profilometry using operational parameters of: 1000 μm scan length; 50 μm/s scan rate; and 14.4 mg stylus force. Table 6, below, contains the resulting measurements.

**Table 6 – Average Thicknesses of Sputtered Au-Ti Metallic Layer**

Batch	Wafer	Process Stage	Target Material	Time (min:sec)	Step Height (nm)
1	1 - 4	Adhesion Layer	Titanium (Ti)	1:15	125 ± 15
		Conducting Layer	Gold (Au)	16:00	
2	5 - 8	Adhesion Layer	Titanium	1:15	134 ± 19
		Conducting Layer	Gold	13:30	

Fairly inexplicably, despite a shorter exposure time in the second batch, an increased amount of gold or titanium was able to eject from the target surfaces and sputter at a higher-than-expected thickness growth rate.

3.6.1.5 THIN-FILM METALLIC LAYER RESISTIVITY

The analogue glass slides that were included in every PVD process were measured with 4 point profilometry (4PP) to empirically obtain the resistivity and sheet resistance of the deposited Au-Ti layers.

Applying a current of 0.1 mA, the sheet resistance and resistivity of the deposited Au-Ti conducting metallic circuitry layers were found to be 0.39 ±

0.03  $\Omega/\square$  and  $5 \times 10^{-6}$   $\Omega\text{-cm}$  for batch 1, respectively, with an average layer thickness of  $134 \pm 19$  nm. For batch 2, an average layer thickness of  $125 \pm 15$  nm, an average sheet resistance of  $1.4 \pm 0.8$   $\Omega/\square$  and a resistivity of  $19 \pm 10 \times 10^{-6}$   $\Omega\text{-cm}$ . Results from the 4PP tests are summarized in Table 7, below. (N = the number of sites sampled on a single slide for a given testing run.)

**Table 7 – Batch 1 and 2 Au-Ti Metallic Layer Resistivity**

<b>Batch 1 – Test #1:</b>	
Avg. Layer Thickness, t (nm):	125 $\pm$ 15
Average Sheet Res., Rs ( $\Omega/\square$ ):	0.39 $\pm$ 0.03
Min - Max ( $\Omega/\square$ ):	0.357391 – 0.440572
Resistivity, $\rho$ ( $\Omega\text{-cm}$ ):	$5 \times 10^{-6}$
# of Sample Sites Tested, N:	8
<b>Batch 1 – Test #2:</b>	
Avg. Layer Thickness, t (nm):	125 $\pm$ 15
Average Sheet Res., Rs ( $\Omega/\square$ ):	0.39 $\pm$ 0.02
Min - Max ( $\Omega/\square$ ):	0.366574 – 0.423737
Resistivity, $\rho$ ( $\Omega\text{-cm}$ ):	$5 \times 10^{-6}$
# of Sample Sites Tested, N:	4
<b>Batch 2 – Test #1:</b>	
Avg. Layer Thickness, t (nm):	134 $\pm$ 19
Average Sheet Res., Rs ( $\Omega/\square$ ):	2.3 $\pm$ 2
Min - Max ( $\Omega/\square$ ):	0.858369 – 5.119325
Resistivity, $\rho$ ( $\Omega\text{-cm}$ ):	$31 \times 10^{-6}$
# of Sample Sites Tested, N:	5
<b>Batch 2 – Test #2:</b>	
Avg. Layer Thickness, t (nm):	134 $\pm$ 19
Average Sheet Res., Rs ( $\Omega/\square$ ):	0.51 $\pm$ 0.05
Min - Max ( $\Omega/\square$ ):	0.421127 – 0.564713
Resistivity, $\rho$ ( $\Omega\text{-cm}$ ):	$7 \times 10^{-6}$
# of Sample Sites Tested, N:	5

The four resulting resistivities from the 4PP test runs done on the two metal-coated glass slide analogues from batch 1 and 2 were then summed and averaged below in Table 8.

**Table 8 – Averaged Resistivity of the Au-Ti Metallic Layers (N = 4)**

Avg. Layer Thickness, t (nm):	130 ± 6
Average Sheet Res., Rs (Ω/□):	0.9 ± 0.4
Min - Max (Ω/□):	0.500865 – 1.637087
Resistivity, ρ (Ω-cm):	12 x10 <sup>-6</sup>
Number of Batches Included:	2
Number of Resistivity Tests Performed (N):	4
Number of Sample Sites Tested:	22

With the exception of Test #1 of batch 2 in which the resistivity of the metal layer was measured to be 31 x10<sup>-6</sup> Ω-cm, the measured resistivities were all lower than or equal to 7 x10<sup>-6</sup> Ω-cm, relatively close to gold’s bulk resistivity of 2.44 x10<sup>-6</sup> Ω-cm, and Test #1 of batch 2 measured 31 x10<sup>-6</sup> Ω-cm, still highly conductive. It is unlikely that electronic conduction in the metallic layer will limit or hinder the performance of the neural probe.

### 3.6.1.6 PROTOTYPE ZIF CONNECTOR DEVICE ELECTRICAL RESISTANCE TESTS

Pathway resistances of the wired and fully assembled ZIF connector device were measured from the gold pin of the ZIF to the exposed end of the adjoining wire using a Fluke 289 True RMS Multi-Meter (Fluke; [www.fluke.com](http://www.fluke.com)). Over the 18 channels of the ZIF the average pathway resistance was 0.32 ± 0.08 Ω, with a range of 0.21 to 0.42 Ω. This was within the expected range and was considered small enough that it was considered a negligible contribution to the circuit resistance.

### 3.6.1.7 FABRICATION YIELDS FOR THIN-FILM $\mu$ ECOG DEVICES

Batch yields are measures of how many successfully fabricated devices were obtained out of the maximum number possible, per wafer and per batch. Once fabrication was complete, to inspect and catalogue the fabricated devices, a micrograph of each device's probe head and electrode array was captured using a VHX-2000 Series digital microscope with a VH-Z250R lens capable of magnifications between 250x and 2500x (Keyence; [www.keyence.com](http://www.keyence.com)). Shown in Figure 28, below, are some of the images captured for the catalogue.

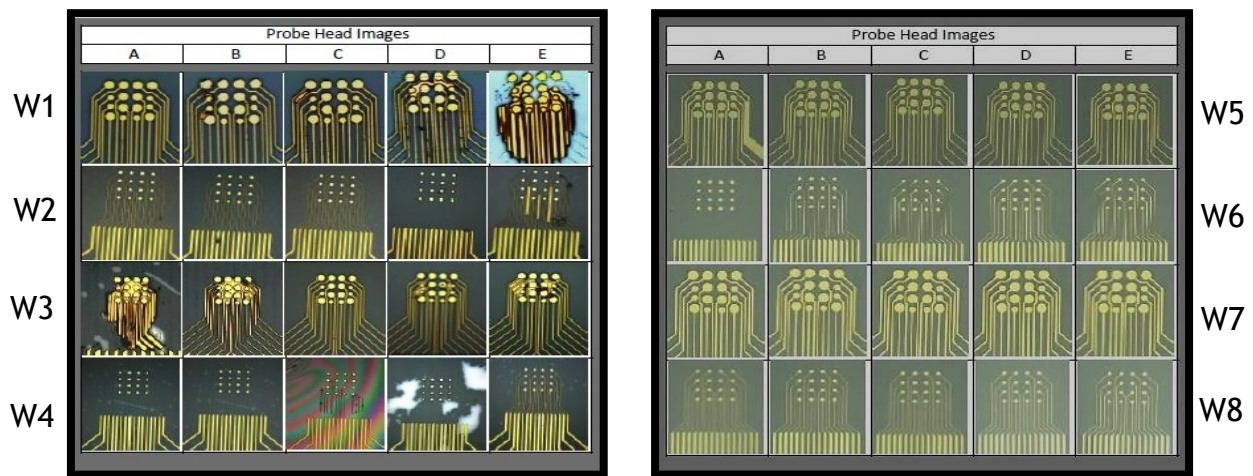


**Figure 28** – Optical micrographs post-fabrication of batch 1 (left) and batch 2 (right). Each row represents a wafer (labelled 'W#') and each column represents a device on the wafer (labelled as 'A, B, C, D, or E').

As is quite visible in the figure, the optimization of the process parameters between the first and second batch of devices made a considerable difference. Between the two batches fabricated, 454 out of 640 usable electrodes were obtained (batch 1: 152, batch 2: 302) resulting in an electrode yield of 70.9%. 6 'perfect' devices from batch 1 (4 Phys. 2, 2 Phys. 1) and 18 from batch 2 (9 each of Phys. 1 and 2) totals at 24 defect-free devices out of 40, resulting in a 60% defect-free device yield overall. The best yield achieved was during the final batch of devices to be fabricated and in this batch a final yield of 94.4% working, defect-free devices.

### 3.7 - SUMMARY OF DESIGN AND FABRICATION

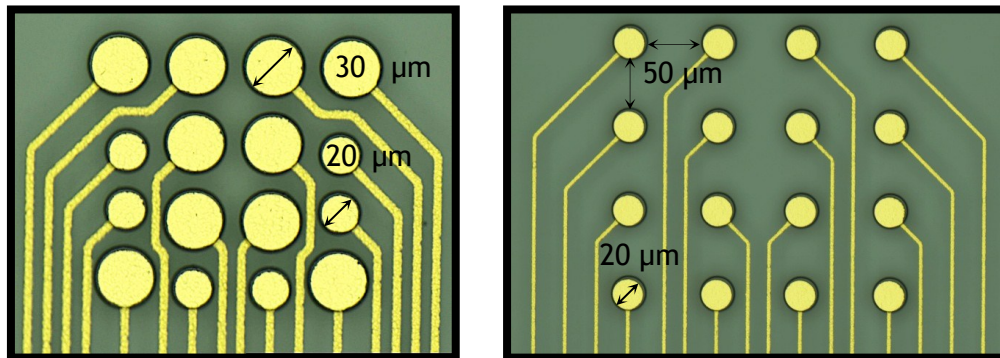
This chapter I focused on the design and fabrication of two electronic devices: 1) a flexible, front-end neural probe device capable of detecting electrical signals from multiple discreet locations, and 2) a back-end ZIF Connector device that connects with ease to the flexible front-end enabling each microelectrode channel to be connected to an external DAS or other electronics.

The fabricated  $\mu$ ECoGs are made of two flexible, biocompatible, layers of P-C, the base layer at 25  $\mu$ m thick for durability plus flexibility and an insulating layer at a thickness of 2  $\mu$ m, sandwiching a thin-film of gold (120 nm) sputtered onto a adhesion layer of titanium (7 nm) and patterned into circuitry using photolithography. A maximum batch yield of 94.4% was obtained, as 18/20 defect-free devices were fabricated in Batch 2 using the established micro-fabrication process flow, see Figure 29.

Fabrication Date	Design Mask	Wafer ID	Device Yield					%	Electrode Yield										%
			A	B	C	D	E		1	2	3	4	5	6	7	8	9	#	
February 20 - Mar 3	Phys 1	W5	14	16	16	16	16	97.5%	[Green]										78
	Phys 2	W6	0	16	16	16	16	80.0%	[Red]										64
	Phys 1	W7	16	16	16	16	16	100.0%	[Green]										80
	Phys 2	W8	16	16	16	16	16	100.0%	[Green]										80
Batch Average								94.4%	Electrodes Made										302

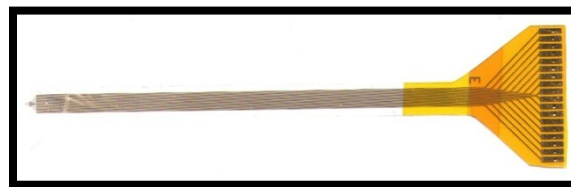
Figure 29 – Batch 2: 94.4% Fabrication Yield Represented Numerically and Visually.

Two electrode layouts with physiologically driven designs were fabricated, both with 16 microelectrodes, as shown below in Figure 30.



**Figure 30** – Phys. Layout 1: High-Density (L) and Phys. Layout 2: Medium Density (R).

Physiological Layout 1, on the left of the figure, is densely packed with ten 30  $\mu\text{m}$  diameter electrodes and six 20  $\mu\text{m}$  diameter electrodes in a square-shaped arrangement that covers 150  $\mu\text{m}$  x 150  $\mu\text{m}$  for investigation into small, functional groupings of neurons in brain slices or small regions of neo-cortical surface. Physiological Layout 2, on the right of the figure, is less densely packed with sixteen 30  $\mu\text{m}$  diameter electrodes in a square-arrangement that covers 270  $\mu\text{m}$  x 270  $\mu\text{m}$  to better enable the detection of the directional vectors of propagating neural oscillations through the extracellular matrix.



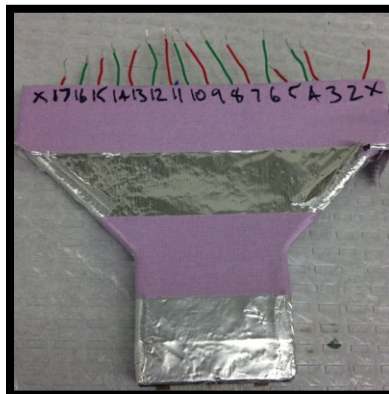
**Figure 31** – Fully fabricated neural probe device, approximately to scale.

Figure 31 shows the flexible neural probe as fabricated, in overall dimensions is over 7 cm long, 2.54 cm wide at its base, 0.5 cm wide along the probe length and relatively flexible with a total thickness of approximately 27  $\mu\text{m}$ . It was first to be designed and fabricated to ensure compatibility and an effortless connection with a back-end ZIF connector device.

Using CAD, a back-end ZIF connector device was designed and prototyped, and housed in a hard-shell casing that protects and secures both the ZIF connector and the necessary wiring for connecting individual electrodes to commercially available external electronic hardware. The front-end probe, with its long flexible probe body eventually fanning out to the proper specifications of 1 mm pitch, the ZIF tail connector pads connect to the pins in the 18-channel, 2.5 cm wide ZIF-clip. Wires alternating in casing color were soldered onto the backside of the ZIF and encapsulated in a bubble of epoxy for rigidity, allow the connection to external electronics. The completed and experimentally ready-to-use ZIF connector is pictured below in Figures 32 and 33.



**Figure 32** – Images of a  $\mu$ ECoG Probe mounted into a ZIF-Connector device taken from two different angles (dimes for scale).



**Figure 33** – Fully assembled and labelled back-end ZIF-connector device.

To confirm that the back-end device was conducting properly the DC resistance of the ZIF connector was measured channel-by-channel. The average measured

resistance being  $0.32 \pm 0.08 \Omega$ , ranging between 0.21 and 0.42  $\Omega$ . A negligible amount of resistance in the impedance characterizations was covered in the following chapter, and therefore was not included in any circuits.

The results and discussion of the electrochemical impedance spectroscopy (EIS) characterizations of the as-made microelectrodes, as well as atomic force microscopy (AFM) data collected from the micro-electrodes, and the electrode-wells surrounding them are included in Chapter 4, in which I focus on the electrochemical characterization and modification of the microelectrodes of fabricated  $\mu$ ECoG probe devices.

---

**CHAPTER 4 - ELECTROCHEMICAL**  
**MODIFICATION OF THIN-FILM  $\mu$ ECOG**  
**ELECTRODES**

---

## 4.1 - INTRODUCTION TO NEURAL ELECTROCHEMISTRY

Electrochemistry is an incredibly powerful science with an enormous number of applications in neuroscience alone; however, much of its strength comes from the sensitivity and precision of the instrumentation and experimental methods. In this chapter I focus on the electrochemical methods and materials I used to modify and characterize the microelectrodes of the  $\mu$ ECoG probes fabricated, as previously detailed in Chapter 3.

The objective of the work I describe throughout Chapter 4 is to obtain  $\mu$ ECoG devices with different electrode modification types to investigate the influence that electrode size and interface material (gold or poly(3,4-ethylenedioxythiophene) (PEDOT)) have on the *in vitro* electrochemical impedance spectroscopy (EIS) of the microelectrodes at various physiologically relevant frequencies. Identically modified probes must also be available deflection testing - discussed in Chapter 5.

I begin Chapter 4 with a brief background on some historic and cutting-edge biocompatible implant electrode materials. Following this the various types of working electrode (WE) used is overviewed along with the other electrodes. Various components of the electrochemical apparatus, the materials, chemicals and equipment that I used, and the details of the electrochemical methods applied - including the compositions of the electrolyte solutions, the process parameters used for both the electrochemical modifications and EIS testing will be outlined. Finally, the chapter concludes with the resulting outcomes from testing and inspection, which are summarized along with related discussion as to whether the objectives of the chapter were met.

## 4.2 - BIOCOMPATIBLE ELECTRODE MATERIALS

Generally, any electrically conductive material can be a WE, but due to the final application of these electrodes involving being used in a highly-sensitive biological environment, such as the brain, only a few materials that are bio-inert, bio-compatible and conductive enough for use in implantation into the human body and brain have been found or developed so far.<sup>74</sup> For example, copper and silver, both common WE materials in general electrochemical applications, have been found to be bio-toxic and are known to cause tissue necrosis in biological applications.<sup>75</sup>

Initially, certain non-noble metals such as stainless steel, tantalum and titanium were used until noble metals (platinum (Pt), gold (Au), iridium (Ir)), alloys (PtIr) and oxides (PtO<sub>x</sub>, IrO<sub>x</sub>) were found to be highly effective as bioelectrodes within implantable neural prostheses.<sup>75-78</sup> However, emerging materials such as carbon nanotubes (CNTs),<sup>20,79</sup> high surface area (HSA) bio-inert materials like titanium nitride (TiN),<sup>17</sup> intrinsically conductive polymers (ICPs) such as polypyrrole (PPy) and PEDOT<sup>20</sup> and composite electrode materials (Au nanoparticles in PEDOT, CNTs in PEDOT)<sup>80,81</sup> have shown equal or better performance compared to the previous generation of materials.<sup>17,20</sup>

PEDOT has been used as the electrode interface material in neural probes at an increasing rate by a growing number of researchers. So, what is PEDOT exactly and why is it effective as a biocompatible electrode material?

## 4.2.1 THE DISCOVERY AND DEVELOPMENT OF PEDOT

Discovered in the late 1980's, poly(3,4-ethylenedioxythiophene), or PEDOT, is an electrically conductive, chemically stable, biocompatible polymer that can be processed by a variety of fabrication methods to obtain electrode interface ideal for the microelectrodes of neural probes.<sup>82,83,84-87</sup>

Intrinsically-conductive polymers (ICPs) are an unusual group of materials, as polymers are typically insulating and non-conductive when compared to metals and semiconductors.<sup>88</sup> PEDOT is a p-type semi-conductor, deficient in the available electrons needed for charge neutrality, which results in vacant orbitals that enable the “hopping” of electrons along the conjugated  $\pi$ -bonds of the molecules carbon-backbone.<sup>82</sup> The p-type nature of PEDOT also results in the need for negatively charged ions/molecules to be present in close-proximity to counter-balance to the intrinsic positive charge of the molecular chain - these are referred to as counter-ions.<sup>89</sup> To better illustrate this concept, a single EDOT monomer and a chain of polymerized PEDOT<sup>+</sup> with a representative counter-ion, A<sup>-</sup>, are shown on the left and the right, respectively, in Figure 34, below.<sup>90</sup>

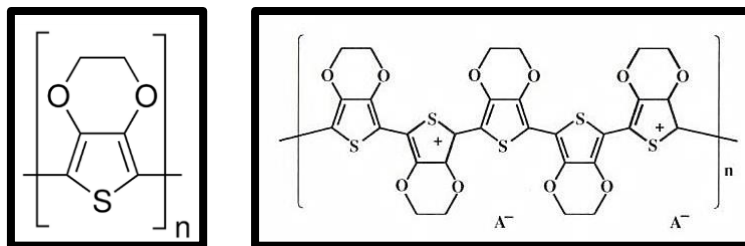


**Figure 34** – The molecular structure of an EDOT monomer (LEFT) and a 5-mer PEDOT<sup>+</sup> chain with a representative counter ion A<sup>-</sup> (RIGHT).<sup>91</sup>

Various methods have been found and developed by chemists and electrochemists over the years for the chemical and electro-chemical polymerization of the 3,4-ethylenedioxythiophene (EDOT) monomer, along with

an appropriate counter-ion, into a conductive, polymeric coating; two such methods are: 1) spin-coating followed by a thermal crosslinking procedure and 2) constant-current electro-deposition from an electrolyte solution.<sup>90</sup>

## **4.3 - EXPERIMENTALLY USED ELECTRODE**

### **MATERIALS**

This experimental work focused on 20  $\mu\text{m}$  and 30  $\mu\text{m}$  diameter gold disc microelectrodes modified with either a thin or a thick layer of PEDOT<sup>+</sup>/ClO<sub>4</sub><sup>-</sup>. These same two PEDOT layer modifications were repeated on versions of the gold disc microelectrodes that were initially electrochemically gold-modified for improved adhesion of the PEDOT. The reasons for these material selections outlined in this section, beginning with the two variations of gold electrode used I will then move on to discuss the two PEDOT layers being applied.

#### **4.3.1 SPUTTERED GOLD AND ELECTROCHEMICALLY DEPOSITED GOLD ELECTRODES**

The two gold working electrodes that I used in all experiments in this work were (1) sputtered, 'as-made' (AM) gold, and (2) gold-modified (GM) electrodes based on (1) that had been electrodeposited with rough, HSA GM adhesion layers. Gold, which is prevalent in the literature for neural interfaces, was selected because it is a noble metal that is biocompatible, has good conductivity and elemental purity.<sup>92</sup> Platinum would have been an equally effective choice, however, there is some belief that sulphur-gold reactivity enhances the adhesion of the PEDOT layer due to the presence of a thiol group in the EDOT monomer - although no strong evidence has been found to support this, it is not uncommon for Pt electrodes to be electrochemically modified with a gold adhesion layer prior to the electrodeposition of PEDOT.<sup>93-96</sup>

Another factor influencing my choice to use a gold adhesion layer was the numerous sources in the literature describing a wide variety of methods to obtain various surface morphologies: fuzzy, dendritic, nano-porous, high aspect ratio nano-pillars, nano-particles, and nano-grains that form nano-petals of a nano-flower.<sup>97-103</sup> For the sake of maximizing adhesion and electrochemical surface area (ESA) and thereby reducing impedance, obtaining a rough, HSA morphology comprised of numerous small grains for a GM WE is feasible to fabricate based on available literature sources. This type of GM was effective experimentally by allowing me to perform adhesion tests on the two thicknesses of deposited PEDOT.

### 4.3.2 ELECTRODES ELECTRO-POLYMERIZED WITH POLY(3,4-ETHYLENEDIOXYTHIOPHENE)

The ideal bioelectrode materials for neural implants are materials that remain stable and bio-inert while implanted over a long period of time without oxidizing at voltages within the operational window of electrode potentials, exhibiting capacitive, non-faradaic polarization and/or reversible faradaic (reduction-oxidation (REDOX)) reactions.<sup>17,75,104</sup> In this section I address my selection of PEDOT as my biocompatible electrode interface material and my reasons for choosing to use an electrochemical polymerization method rather than the spin-coating method.

Due to PEDOT's ionic and electronic conductivity, chemical and electrochemical stability, polymeric mechanical properties and the multiple methods of fabrication available, it has become highly researched and is often used as an electrode material in neural probe applications. PEDOT coatings have been used *in vivo* on the electrodes of devices implanted into or placed onto the brain, such as: silicon and microwire arrays,<sup>86,105</sup> organic transistors;<sup>70</sup> and flexible, ECoG micro-electrode arrays.<sup>67,106-108</sup> The selection of PEDOT as

the bioelectrode material was not only due to the relatively extensive collection of research literature available on it and its general use in electronics, but also because many neurologically-specific studies have been done to test and explore the various factors involved with the polymerization and performance of PEDOT and other ICP coatings on electrodes of various sizes on a variety of neural probe device types.<sup>91,109-111</sup>

Many investigations have been done on the changes in conductivity and morphology of PEDOT coatings resulting from various electrochemical polymerization conditions using a variety of WE materials, electrical parameters, solvents and counter-ions.<sup>94,95,111,112</sup> Other studies have examined the optical and electronic properties of chemically polymerized PEDOT;<sup>113</sup> outlined many of the costs and benefits related to increasing layer thickness;<sup>114</sup> and assessed the biological compatibility of PEDOT.<sup>115,116</sup> Upon reviewing the literature, I was able to make informed decisions regarding the use of electrochemical polymerization methods (and the process parameters therein) instead of spin-coating it and using chemical polymerization methods.

Spin-coating PEDOT/PSS (with the negatively-charged but non-conducting polymer poly(styrenesulfonate) (PSS) acting as counter-ion) is a commonly used fabrication method for obtaining thin films of conductive polymer, although it has been found that both the method used and the counter-ion selected greatly impacts the conductivity, morphology and stability of the resulting coating.<sup>87,109,112,114,117-125</sup> Spin-coated PEDOT/PSS has a reported conductivity in the range of 50-80 S/cm, and morphologically forms a lamellar structure with the polymer chains running parallel to the electrode interface.<sup>90</sup> Due to the fact that PEDOT uses a ‘hopping’ mechanism for conduction of a charge along the polymer backbone, the increased crystallinity of that arrangement of the conductive pathways, resulting from electrodeposition rather than spin-coating, allows the formation of more conductive pathways and causes a more

perpendicular orientation of molecular chains.<sup>90</sup> Improved crystal structures are achieved by electrodeposition of PEDOT utilizing perchlorate ( $\text{ClO}_4^-$ ) ions - or other small and mobile counter-ions - and better electrical performance is achieved by the increased crystallization as demonstrated by morphological changes and differences in surface area.<sup>89,111,126</sup>

To minimize the electrode impedance, electrodeposition was used in this work to form PEDOT coatings charge-balanced with the negatively charged perchlorate ion ( $\text{ClO}_4^-$ ) as counter-ion.<sup>90</sup> The method of electrodeposition has not only demonstrated better electrical performance but the delamination of electrodeposited layers is also less likely to occur.<sup>114</sup> Delamination and chronic failure is an issue - thicker PEDOT layers are more likely to delaminate and cause failure.<sup>91</sup> However, Zhou, et al. have found that gold adhesion layers seem to work but that adhesion could still be improved.<sup>91</sup> And as mentioned in the previous section, a rough HSA GM microelectrode is used to explore this form of device failure.

## **4.4 - ELECTROCHEMICAL APPARATUS AND MATERIALS**

This section I provide a description of the experimental setup used throughout my experimental work, including a summary of materials, chemicals, tools and equipment that were either needed for experimental processes or that comprised the electrochemical apparatus itself. First the instrumentation, the electronic-hardware and computer-software controlling and/or monitoring the voltage and/or current between the electrodes, is described, followed by lists of materials, chemicals, tools and equipment utilized and the supplier used. The electrochemical apparatus consists of multiple components, each of which serves a specific purpose: the cell container, inert gas supply, magnetic stir

plate, and electromagnetic shielding. This is followed by EIS methods and the electrochemical methods used in the deposition process for the microelectrode modifications are provided following a brief description of how the system and electrolytes were prepared for use. Three-electrode cells were used in all experimental procedures carried out in this work and so the principles of three-electrode electrochemical cells are available for reference in Appendix B, should more background information be desired.

#### 4.4.1 ELECTROCHEMICAL INSTRUMENTATION

An electronic hardware system (and the associated software) that simultaneously drives and measures desired electrode reactions or characterization processes is an electrochemical instrument. The overall behaviour of the cell is governed by Ohm's Law (potential ( $E$ ) = current ( $I$ ) x resistance ( $R$ )). These three variables can each be manipulated to achieve a specific amount of voltage or current. An electrochemical instrument differs from a standard power-supply in that it has been designed for the precise execution and sensitive monitoring of electrochemical experiments where, for example, in the case of a potentiostat, the potential ( $E$ ) of the working electrode is held at a static value, despite any real time changes occurring to resistance ( $R$ ) within the cell, while the current ( $I$ ) response is recorded over time.

For my work in this thesis project I used a Gamry Instruments Reference 3000 - Potentiostat/Galvanostat/ZRA as my primary instrumentation in most of the electrochemical experiments. Prior to the first experimental use, and periodically thereafter, I calibrated the Reference 3000 for both AC and DC applications by using the supplied "EIS Dummy Cell" and accompanying instructions.

## 4.4.2 EXPERIMENTAL MATERIALS AND SUPPLIERS LIST

- 10mL Pyrex® Beaker; Teflon-Coated Magnetic Stir Bars, X-Shaped; 1 cm x 7.5 cm Disposable Test Tubes; Assorted Clamps; Bench-Top Laboratory Clamp Stands; 2mL Serological Pipettes; Glass Pasteur Pipettes; 4m Flexible Tubing (9mm O.D. 6mm I.D.); Sparkleen® Glass Cleaner; and Aluminum Foil (Fisher Scientific; [www.fishersci.com](http://www.fishersci.com))
- MF 2079 3-Pack of Aqueous Silver-Silver Chloride (Ag/AgCl) R.E.; MF 1032 Platinum Wire C.E.; MF 2062 Non-Aqueous R.E. Kit [Silver-Silver Ion (Ag/Ag<sup>+</sup>)] (BASi; [www.BASInc.com](http://www.BASInc.com))
- Acetone, Certified ACS Grade (C<sub>3</sub>H<sub>6</sub>O); Isopropyl Alcohol, 70% v/v (IPA), (C<sub>3</sub>H<sub>8</sub>O); Phosphate-Buffered Saline (PBS) 10X Concentrate (Composition in g/L: 80 NaCl, 2 KCl, 14.2 NaPO<sub>4</sub>, and 2.4 KPO<sub>4</sub>); 3, 4-Ethylenedioxythiophene Monomer (EDOT) (C<sub>6</sub>H<sub>6</sub>O<sub>2</sub>S); Acetonitrile, Certified ACS (C<sub>2</sub>H<sub>3</sub>N); Lithium Perchlorate (>98% LiClO<sub>4</sub>); Silver Perchlorate (>99% AgClO<sub>4</sub>); Poly(vinylpyrrolidone) Powder (PVP40) ([C<sub>6</sub>H<sub>9</sub>NO]<sub>n</sub>); Gold(III) Chloride Hydrate (99.999% HAuCl<sub>4</sub> · xH<sub>2</sub>O) (Sigma-Aldrich; [www.sigmaaldrich.com](http://www.sigmaaldrich.com))
- Ultrapure Milli-Q® De-Ionized Water (DI) (Millipore EMD, [www.emdgroup.com](http://www.emdgroup.com))
- Ultra-High Purity Nitrogen Gas (N<sub>2</sub>) (Praxair; [www.praxair.com](http://www.praxair.com))
- Reference 3000 Potentiostat/Galvanostat/ZRA (Gamry Instruments; [www.gamry.com](http://www.gamry.com))
- Corning Stirrer/Hotplate; Branson 5510 Sonication Bath; *Research Plus* Eppendorf Micro-Pipette (Thermo-Scientific; [www.thermofisher.com](http://www.thermofisher.com))
- XP105 DeltaRange® Weigh Scale (Mettler Toledo; [www.mt.com](http://www.mt.com))
- 289 True RMS Multi-Meter (Fluke; [www.fluke.com](http://www.fluke.com))
- Milli-Q® Synergy® UV Ultrapure Water De-Ionization System (Millipore EMD; [www.emdgroup.com](http://www.emdgroup.com))

### 4.4.3 ELECTROCHEMICAL APPARATUS

In this section I provide descriptions of the various auxiliary/support components of the experiment: starting with the heart of the apparatus, the cell container; I then work through the hardware and auxiliary/support components used to control the electrode placement; the inert gas supply; magnetic stir plate; and the electromagnetic shielding used throughout the sensitive electrochemical impedance spectroscopy methods.

#### 4.4.3.1 ELECTROCHEMICAL CELL CONTAINER

The electrolyte container and electrode fixtures are essential components of an electrochemical cell. Both custom-made and commercial cell containers can be used for these processes. One of the main benefits of using a commercial or custom-made cell is that the various associated components “click” together nicely, forming tight seals enabling a high degree of environmental control within the cell. However, that very benefit becomes a restriction that prevents/inhibits the use of specially designed or off-brand electrodes that are built in such a way that their placement in the cell container may be undesirable or even impossible. In this work, a 10 mL beaker is the electrolyte container since it easily accommodates the unusual working electrode (i.e. the thin-film  $\mu$ ECoG neural probe’s microelectrode array’s flexible matrix). To acquire consistent results during the electrochemical processes, repeatable, secure placement of the electrodes is required. To achieve this using a non-commercial cell container, multiple adjustable clamp-arms of varying types were affixed onto a vertical clamp-stand such that the various electrodes would be placed in nearly the same position for every test.

#### 4.4.3.2 INERT GAS SUPPLY

For these electrochemical applications the electrolytes were de-gassed to remove dissolved atmospheric air (~77% N<sub>2</sub> and 23% O<sub>2</sub>) that could otherwise introduce problematic oxygen reactions. To remove as much oxygen as possible, ultra high purity nitrogen gas was bubbled through the electrolyte for ~10 min. The electrolyte was then transferred rapidly by pipette into a cell container with an inert gas pouring on top of the beaker to act as a blanket gas and prevent atmospheric contamination. The flow rate of the inert blanket gas was determined by slowly increasing the line pressure while watching for the onset of visual perturbations at the surface of the electrolyte and then reducing the line pressure gradually, until the perturbation visibly stops but gas is continuing to flow. Done properly, it should not be possible to observe any gas flow. Gas flow checks (accomplished by pinching closed and then quickly releasing the gas supply line so that a burst of gas would visibly hit the electrolyte surface) were performed intermittently throughout the experiment to ensure the gaseous blanket was still present. While the use of nitrogen was acceptable, however the use of argon gas would have been more effective in an electrochemical cell without a lid to physically contain the inert gas because it is heavier than air and would therefore settle into the beaker and form a better blanket.

#### 4.4.3.3 MAGNETICALLY FORCED CONVECTION

To enable forced convection within the electrochemical cell, a Teflon<sup>®</sup>-coated magnetic stir-bar was placed within the electrochemical cell container which is then placed on top of a magnetic stirrer/hotplate. A sheet of aluminum foil was placed between the stirrer and the cell container to enable electromagnetic shielding from below the cell container and reduce the electrical noise introduced into the system.

#### 4.4.3.4 ELECTROMAGNETIC SHIELDING

Due to the extreme sensitivity of microelectrode processes and the extremely small magnitudes of current involved, the electromagnetic noise generated from electronics in the laboratory created interference and had to be blocked out with an electromagnetic radiation (EMR) absorbing shield, typically called a Faraday cage (FC).<sup>1</sup> See Figure 35:

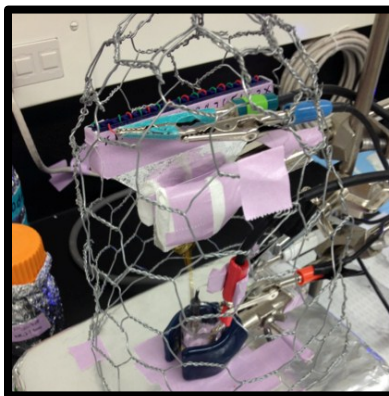


**Figure 35** – The electrochemical cell within the Faraday cage. Apparatus components not shown: Gamry Reference 3000, N<sub>2</sub> gas blanketing tube and stir bar.

## 4.5 - ELECTROCHEMICAL DEPOSITION PROCESSES AND ELECTROLYTES

In this section, the electrochemical method of constant-current deposition and the preparation of the electrolytes and electrochemical apparatus are briefly described followed by the results of the characterization process are then provided with microelectrode images and EIS Bode plots.

The pre-test cleaning and maintenance/calibration required for the electrode-types (working-, counter-, and reference-) is provided in Appendix B.

## 4.5.1 ELECTROCHEMICAL DEPOSITION METHODS

Regarding the electrochemical deposition method, there are multiple methodologies available (including constant current and constant voltage modes), the choice of which affects the material properties.<sup>112</sup>

Constant-current mode is widely used and theoretically allows for a specified amount of charge transfer to occur and therefore a precise amount of deposited material, although small variations in current efficiency may have skewed this in practice.<sup>127</sup> Assuming that the current efficiency is 100%, or at least equal for both the as-made and gold-modified microelectrodes being plated, the quantity of material deposited was precisely controllable by the deposition time.<sup>127</sup>

Since the electrolyte solvent utilized is also important for maximizing performance electrically and coating morphology, the non-aqueous solvent acetonitrile (ACN) was used here due to its reported improved electrical performance.<sup>109</sup>

## 4.5.2 ELECTROLYTE SOLUTIONS

- 25 mM gold (III) tetrachloride hydrate and 20 g/L poly(vinylpyrrolidone) (25 mM  $\text{HAuCl}_4 \cdot x\text{H}_2\text{O}$ , 20 g/L PVP; aqueous)
- 0.01 M 3,4-ethylenedioxythiophene and 0.1 M lithium perchlorate in acetonitrile (0.01 M EDOT, 0.1 M  $\text{LiClO}_4$ ; non-aqueous ACN)
- 1 M phosphate-buffered saline (1 M PBS; aqueous)

## 4.5.3 PREPARING THE ELECTROCHEMICAL CELL

Prior to the experiments, the electrodes, stir bar and electrochemical cell container were cleaned thoroughly to remove any trace contamination. The WEs and CEs were rinsed with acetone and then submerged in a small acetone-

filled test tube. This tube was then sonicated in an ultra sound bath for 2 minutes. The electrodes were then removed from the acetone, rinsed with 70% isopropyl alcohol (IPA) and then placed into an IPA filled test tube for 2 minutes of sonication. Then the electrodes were then rinsed with high purity Milli-Q de-ionized (DI) water and placed into a DI filled test tube for a final 2 minutes of ultrasound sonication. Finally, the electrodes were given one more rinse in DI and were carefully blown dry using compressed air or nitrogen gas. The stir bars were cleaned using the same method as the electrodes but with a larger test tube that accommodated the stir bar. The beaker used as the container was thoroughly scrubbed clean with Sparkleen® and tap water. Once cleaned and rinsed thoroughly this way, the beaker was rinsed successively with acetone, IPA and finally DI water. The beaker was then blown dry with compressed air. To remove the reactive oxygen species from the system, inert nitrogen (N<sub>2</sub>) gas was used to displace dissolved oxygen for 10 min.<sup>92</sup> Once this de-oxygenating procedure had been completed, the electrolyte was then transferred into the electrochemical cell container and continuously blanketed with N<sub>2</sub> gas for the duration of the experiments.

## **4.6 - GOLD ADHESION LAYER MODIFICATION**

### **DEPOSITION**

On some electrodes, a gold adhesion layer was deposited electrochemically to increase the adhesion between the sputtered Au and the subsequent PEDOT layers. Gold deposition was carried out in a 3-electrode cell (Pt wire CE, Ag|AgCl RE and Au microelectrode as WE) blanketed with high-purity N<sub>2</sub> gas inside a Faraday cage to block out unwanted noise interference. The aqueous electrolyte solution used in the gold deposition process was composed of 25 mM gold chloride hydrate (HAuCl<sub>4</sub> • nH<sub>2</sub>O) and 20 g/L polyvinylpyrrolidone (PVP40) in Milli-Q DI water. The electrolyte solution was bubbled with N<sub>2</sub> for 10m to

displace dissolved O<sub>2</sub> before filling the cell container. The plating solution was magnetically stirred with a Teflon® coated stir-bar before and after each deposition to re-distribute and equalize the chemical species concentrations.

#### 4.6.1 ADHESIVE GOLD MODIFICATION

- 100s initial delay (or until <0.1 mV/s instability is reached)
- 5s conditioning step at 0 V
- 5s rest for equilibration
- 5s at pre-deposition current of 0 A
- 1s constant current deposition at -14.14 mA/cm<sup>2</sup>
- 690s constant current deposition at -3.54 mA/cm<sup>2</sup>

The total charge transferred was kept constant at -17.35 and -7.7 μC for 30 and 20 μm diameter electrodes; respectively. These parameters and the use of PVP as a surfactant was with the intention of nucleating numerous small grains of gold to form a rough layer across the electrode surface, vastly increasing the electrochemical surface area available and providing a strong base for the adhesion of PEDOT layers.

### 4.7 - CONSTANT-CURRENT PEDOT MODIFICATIONS

In this section I detail how I acquired two more modification types and two different layer thicknesses for testing PEDOT as a biocompatible microelectrode material in μECoG neural probe systems along with its adhesion/delamination relative to layer thickness. EDOT electrolyte was bubbled with ultra-high purity N<sub>2</sub> gas prior to the deposition process to displace the dissolved oxygen. A Pt wire was used for CE, a non-aqueous Ag|Ag<sup>+</sup> for the RE and an AM or GM WE. N<sub>2</sub> gas blanketed softly onto the cell container inside

of a FC. The electrolyte was stirred for 10 to 30 s before and after every deposition to redistribute and equalize chemical species concentrations. The desired electrode channel was connected VIA alligator-clip to the enumerated ZIF Connector wire of choice and the modification of the microelectrode by electroplating could begin.

#### 4.7.1 THIN PEDOT MODIFICATION P1

- 100 s initial delay (or until  $< 0.1$  mV/s instability is reached)
- 5 s rest - 5 s at pre-deposition current of 0 A
- 24 s constant current deposition at  $0.5 \text{ mA/cm}^2$
- Expected thickness: Approximately 150 nm or  $0.150 \mu\text{m}$

#### 4.7.2 THICK PEDOT MODIFICATION P2

- 100 s initial delay (or until  $< 0.1$  mV/s instability is reached)
- 5 s rest - 5 s at pre-deposition current of 0 A
- 118 s constant current deposition at  $0.5 \text{ mA/cm}^2$
- Expected thickness: Approximately 700 nm or  $0.700 \mu\text{m}$

Many factors influenced the final outcomes of these modifications but, overall these modifications were effective, easy and were easily tweaked as needed.

## 4.8 - RESULTING ELECTRODE MODIFICATIONS

For the sake of clarity, Table 9 provides a summary of the electrode identification (ID) codes used to distinguish one electrode size and type from another.

**Table 9** – Microelectrode Modification ID Codes

Condition of Gold Electrode	PEDOT Mod.	Diameter (μm)	Modification ID Code
As-Made Sputtered Gold <b>AM</b>	N/A	<b>20</b>	<b>AM 20</b>
As-Made Sputtered Gold <b>AM</b>	N/A	<b>30</b>	<b>AM 30</b>
Gold Modification <b>GM</b>	N/A	<b>20</b>	<b>GM 20</b>
Gold Modification <b>GM</b>	N/A	<b>30</b>	<b>GM 30</b>
As-Made Sputtered Gold <b>AM</b>	Thin PEDOT <b>P1</b>	<b>20</b>	<b>AMP1 20</b>
As-Made Sputtered Gold <b>AM</b>	Thin PEDOT <b>P1</b>	<b>30</b>	<b>AMP1 30</b>
As-Made Sputtered Gold <b>AM</b>	Thick PEDOT <b>P2</b>	<b>20</b>	<b>AMP2 20</b>
As-Made Sputtered Gold <b>AM</b>	Thick PEDOT <b>P2</b>	<b>30</b>	<b>AMP2 30</b>
Gold Modification <b>GM</b>	Thin PEDOT <b>P1</b>	<b>20</b>	<b>GMP1 20</b>
Gold Modification <b>GM</b>	Thin PEDOT <b>P1</b>	<b>30</b>	<b>GMP1 30</b>
Gold Modification <b>GM</b>	Thick PEDOT <b>P2</b>	<b>20</b>	<b>GMP2 20</b>
Gold Modification <b>GM</b>	Thick PEDOT <b>P2</b>	<b>30</b>	<b>GMP2 30</b>

As shown in the above table, the different electrode modification types (or electrode surface conditions) are combinations of three variable parameters: 1)

an as-made (AM) or gold-modified (GM) base metallic layer; 2) a thin-PEDOT (P1) or a thick-PEDOT (P2) modified layer; 3) and electrode diameters of 20 or 30  $\mu\text{m}$ .

#### 4.8.1 AVERAGE P1 AND P2 LAYER THICKNESSES:

The average layer thicknesses found through AFM measurements is detailed in Chapter 5, Section 5.3. For the sake of discussion, the rough averages of the PEDOT layers deposited onto AM surfaces and those deposited onto GM electrode surfaces.

For the P1 and P2 layers deposited on AM electrodes, thicknesses were roughly 75 nm and 350 nm for the 20  $\mu\text{m}$  and 30  $\mu\text{m}$  diameter, respectively - only 50% of the expected thicknesses stated in the deposition parameters.

On the rough gold GM electrodes, PEDOT layers were approximated to be roughly 25 nm and 220 nm thick on average, for the 20 and 30  $\mu\text{m}$  diameter electrodes, respectively - thicknesses more than 80% less-thick than predicted previously.

## 4.9 - VISUAL INSPECTION OF MICROELECTRODE SURFACES

In the next section, I have included visual images as recorded with an optical microscope that allow for the inspection of each microelectrode modification type and size.

A Keyence 2000-Series with a Z250R lens was used to take these images of the electrodes. The image capturing was performed with the Keyence software's "Depth-Composition" mode, giving the images more sense of depth by taking multiple captures incrementally along a defined region of the z-axis.

### 4.9.1 AS-MADE MICROELECTRODES (AM)

The as-made (AM) microelectrodes appear to be bright gold/yellow as shown in Figure 36, below. It can be seen that the surface is relatively specular, more so at lower magnifications, such as 20x or 40x, but has a definite texture on the surface when more powerful magnification is used.

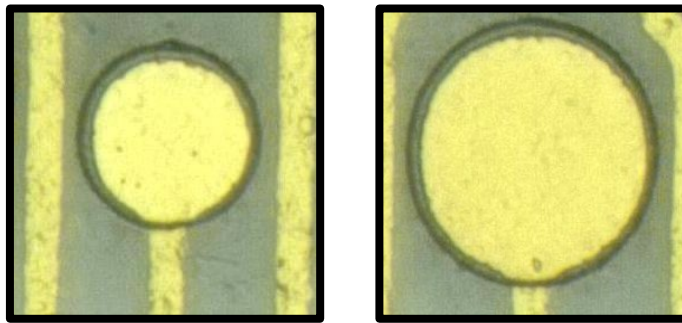


**Figure 36** – 'As-Made' gold microelectrodes at 1500x magnification.  
(Left: 20  $\mu\text{m}$  diameter; Right: 30  $\mu\text{m}$  diameter)

In a highly qualitative way, the surfaces of these sputtered gold electrodes somewhat resemble a crater-pocked surface like that of the moon (which makes sense since they were both bombarded repeatedly by projectiles).

## 4.9.2 GOLD MODIFIED ELECTRODES (GM)

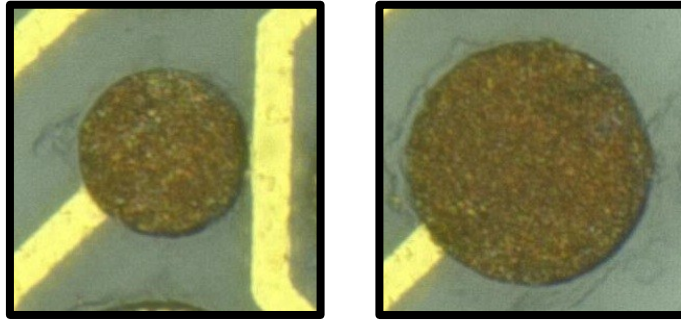


**Figure 37** – 'Gold-Modified' rough-gold microelectrodes at 1500x magnification.  
(Left: 20  $\mu\text{m}$  diameter; Right: 30  $\mu\text{m}$  diameter)

At lower magnifications, these electrodes, shown in Figure 37, appear dark red, nearly black. This is due to the large number of randomly aligned small grains of gold that formed during the deposition process.

Acquiring this ideal adhesion layer and conductive base for PEDOT to be deposited with this exact morphology in an easily repeatable manor was difficult. I believe this difficulty was related to the nucleation and subsequent growth of precipitated gold particles in the electrolyte solution. This was partially controlled by the use of freshly made solutions and the storage of the electrolyte in aluminum foil wrapped containers. Storage of the solution in a refrigerator may be a useful for extending the shelf-life by slowing particle nucleation and growth.

### 4.9.3 PEDOT MODIFICATION 1 ON AS-MADE MICROELECTRODES (AMP1)

This modification is the first to feature PEDOT and is composed of a very thin layer of PEDOT on the specular AM gold electrode surface. On AMP1, shown on the next page in Figure 38, small, bluish-greenish-blackish spots are visible where PEDOT nucleated into nodes that have grown as a cluster.

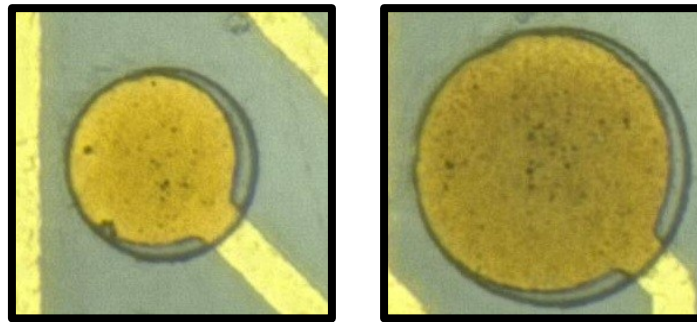


**Figure 38** – ‘As-Made’ & PEDOT Modification 1 microelectrodes at 1500x magnification.  
(Left: 20  $\mu\text{m}$  diameter; Right: 30  $\mu\text{m}$  diameter)

It seems that these grew at point defects across the surface of the electrodes somewhat randomly - the centre, the edges or corners - and relatively, but obviously not entirely, uniformly. There are definitely clusters of PEDOT that have grown to be much larger than others. I believe this to most likely to be due to the presence of a pre-existing defect or imperfection in the AM gold layer sputtered during the micro-fabrication process. The electrode surfaces have a slightly-tinted, brown appearance compared to the protected gold traces, which means that the thin-film of PEDOT has been deposited across the entire electrode surface.

A key feature of these modifications for good biocompatibility is the full and complete coverage of the electrode. Not only would incomplete coverage diminish the electrode’s biocompatibility from an electrode material interface perspective, but from an electrochemistry perspective the presence of two

dissimilar conductive materials within an aqueous, biological saline solution is likely to impact the effective lifetime of an electrode negatively by causing corrosion and serving as a possible initiation-point for the eventual delamination of the PEDOT layer.

#### 4.9.4 PEDOT MODIFICATION 2 ON AS-MADE MICROELECTRODES (AMP2)

While the nodes previously scattered across the AMP1 mods are still slightly evident in Figure 39, below, it appears as though the clusters formed in the first 24 s of deposition (the deposition time for the P1 layer) grew into larger islands that eventually formed a layer of PEDOT at a relatively uniform thickness.

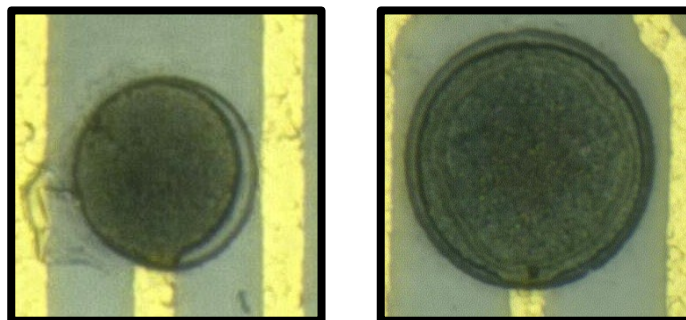


**Figure 39** – 'As-Made' & PEDOT Modification 2 (AMP2) microelectrodes at 1500x magnification. (Left: 20 µm diameter; Right: 30 µm diameter)

As is visible in the above figure, AMP2 layers present with a medium-dark blue-green hue. This colour change from AMP1's brown appearance is due to the thickness of the deposit and the anisotropy of the PEDOT molecules.

Also visible in the above 30 µm micrograph (right hand side) something caused a ring of PEDOT to build up. This may be explained by the electrode edge "hoarding" monomers as they transport in to the surface for the polymerization process.

#### 4.9.5 PEDOT MODIFICATION 1 ON GOLD MODIFIED MICROELECTRODES (GMP1)

GMP1 is darker than AMP1, not only because of GM layer underneath (which is independently darker than the AM or AMP1 modifications), but due to the higher electrochemical surface area, which may have improved current efficiency and caused more PEDOT deposition than expected. In Figure 40, below, PEDOT growth is visibly more formed around the edges at either microelectrode size, but the 30  $\mu\text{m}$  seems to have formed a darker deposition than the 20  $\mu\text{m}$ .

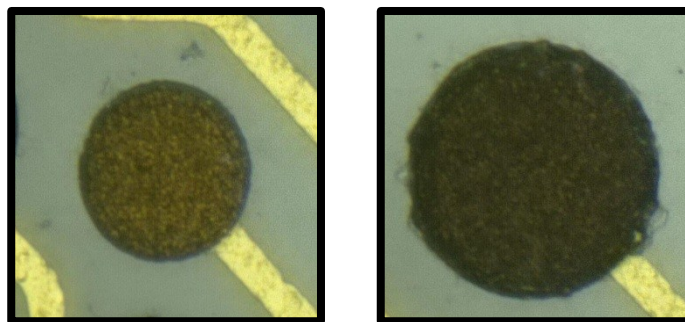


**Figure 40** – Gold Modified & PEDOT Modification 1 microelectrodes at 1500x magnification.  
(Left: 20  $\mu\text{m}$  diameter; Right: 30  $\mu\text{m}$  diameter)

As mentioned above, the current efficiency may have been affected by the increase in “real” surface area of the GM electrodes. This increased area would have reduced the current density across the surface while maintaining the same amount of charge transferred. Additionally, this increase in area could also have affected the mass transfer rate of the electro-active species in the electrolyte by forming a thinner diffuse-layer for the molecules to transport through to and from the electrode surface.

#### 4.9.6 PEDOT MODIFICATION 2 ON GOLD MODIFIED MICROELECTRODES (GMP2)

The thick PEDOT deposits on the GM electrodes makes the dark blue PEDOT layers look even more dark-blue/black. They are by far the darkest of all the electrode modifications in this work (as shown below in Figure 41).

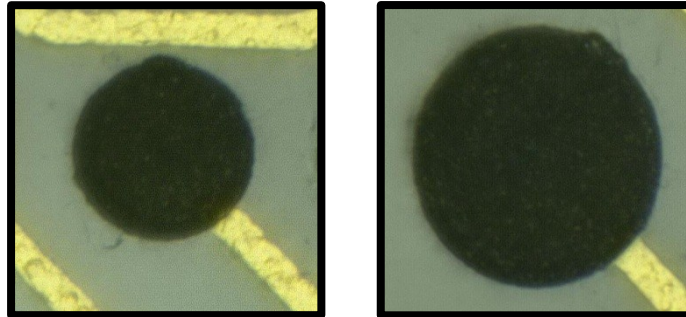


**Figure 41** – Gold-Modified & PEDOT Modification 2 microelectrodes at 1500x magnification (Left: 20 µm diameter; Right: 30 µm diameter)

This modification appears very dark, implying that the deposited PEDOT layer has structural qualities that prevent the reflection of visible light and has an almost furry looking quality to it. The dark appearance of the microelectrode would result from an extremely high electrochemical surface area layer that would be consistent with the expectation of continued growth of the PEDOT nodes into a more cauliflower-like morphology, as found by other investigators who used similar microelectrode electrodeposition processes.<sup>112,122</sup> A more densely deposited PEDOT layer or a thicker P2 deposit (resulting from a lower current-density due to the high surface area of the GM deposition) would also reduce the likelihood for visible light to escape. The GMP2 modified electrodes were found to have multiple outgrowths that could be a strong factor in the success of the deflection tests discussed in the next chapter.

## 4.10 - IN VITRO ELECTROCHEMICAL IMPEDANCE SPECTROSCOPY (EIS) CHARACTERIZATION METHODS AND RESULTS

The purpose of *in vitro* characterization of the devices by electrochemical impedance spectroscopy (EIS) was to observe the performance of the electrodes interface with an electrolyte, to gain insight into the mechanisms of its performance, (such as mass transport, across a spectrum of frequencies) and to quantify the impedance and phase angle of each microelectrode across said spectrum. Due to the influence of the electrolyte on performance, the most appropriate solutions for obtaining insight into the possible *in vivo* performance are those where the ionic conductivity and composition are analogous to fluids in the body.

For EIS testing, the electrolyte solution, 1 M phosphate-buffered saline (PBS), was used at ambient room temperature ranging from 22-25°C with pH 7.4. Immediately prior to being transferred into the electrochemical cell container for the tests, much of the dissolved oxygen in the solution was removed by softly bubbling ultra-high purity N<sub>2</sub> gas through the PBS solution for 10 minutes. To help maintain this de-oxygenated state, a soft flow of pure N<sub>2</sub> gas was used to blanket the electrolyte within the cell container during the testing processes.

EIS was performed one microelectrode at a time by connecting an alligator clip designated for the WE to the ZIF connector wire for the desired microelectrode while the WE device matrix rested against the glass beaker wall. An Ag|AgCl RE and a Pt wire CE were then connected to their respective alligator clips and set into place within the cell container (refer to Appendix B for details). To remove background noise, the FC was connected to the Gamry system's

floating ground and its access-door was closed for the duration of the test. Set on the “low noise” mode in the Gamry software process parameters, the microelectrodes were each characterized from  $10^5$  to 0.1 Hz with an RMS AC potential of 10 mV after being held at open-circuit potential (OCP) for up to 100s to allow for stabilization. If the fluctuations fell below  $\pm 0.1$  mV/s prior to reaching 100s, I assumed adequate stability was attained and automatically began the EIS process immediately.

#### 4.10.1 BODE-PLOT RESULTS FROM *IN VITRO* EIS TESTING OF MICROELECTRODES

The electrochemical performance characteristics of the 20  $\mu\text{m}$  and 30  $\mu\text{m}$  electrodes are shown in Figures 42 and 43 as Bode plots. Bode plots represent two variables on two y-axes: the impedance and the phase angle, as functions of frequency (the x-axis). The impedance (solid lines) and phase angle curves (dotted lines), and were almost entirely consistent with expectations. On the left y-axis, the impedance, all the curves clearly show a decreasing trend as they are followed along the x-axis from the left-hand side to the right-hand side, representing increasing AC frequency. Even at 1 kHz (the frequency at which values are typically reported in the literature) the trend remains intact. All modifications appear to have increased the electrochemical surface area of their respective electrode interfaces compared to the GSA that was initially available. This is evident because all microelectrode modification types for both 20  $\mu\text{m}$  and 30  $\mu\text{m}$  disc diameters ( $GSA_{20} = 314.16 \mu\text{m}^2$ ,  $GSA_{30} = 706.86 \mu\text{m}^2$ ) reduced the impedance at the electrode-interface relative to the ‘as-made’ (AM) condition impedance (the solid yellow lines). The phase angle (in degrees) ranges from  $+90^\circ$  to  $0^\circ$  to  $-90^\circ$  and represents how much of the AC current is real and how much is imaginary. At  $0^\circ$  the impedance is ‘real’ and resistive. As the angle moves to  $-90^\circ$  out of phase, the current is capacitive and as it shifts to  $+90^\circ$  out of phase with the voltage the current is inductive.

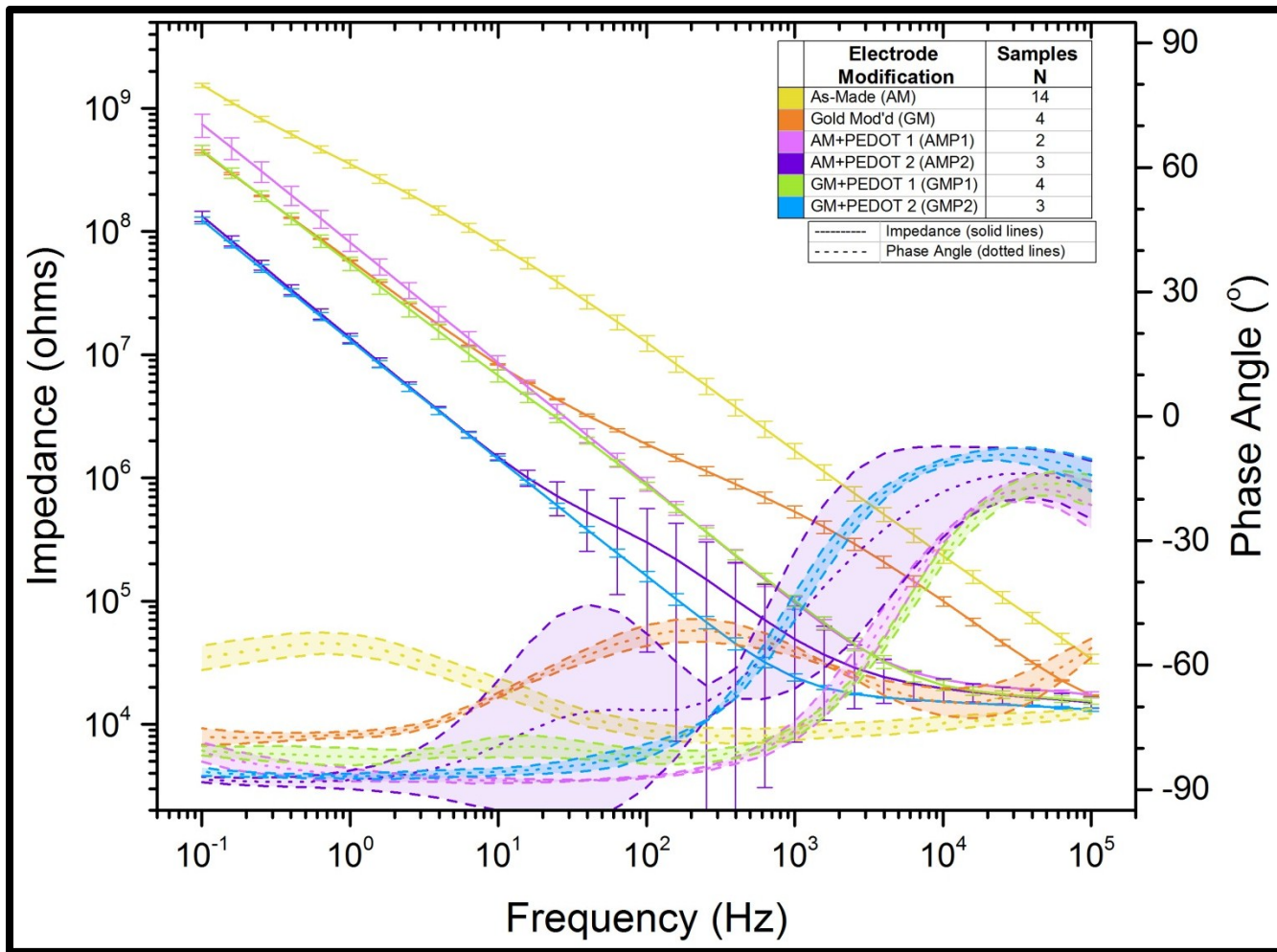


**Figure 42** – Average impedance and phase angle vs. frequency curves for each modification type from the ‘N’ single-test measurements of individual 20  $\mu\text{m}$  electrodes of that type. Error bars represent standard deviation within the sample set. (0.1 to 100,000 Hz at 10 mV<sub>RMS</sub> AC in 1M PBS at room temperature in low noise mode)

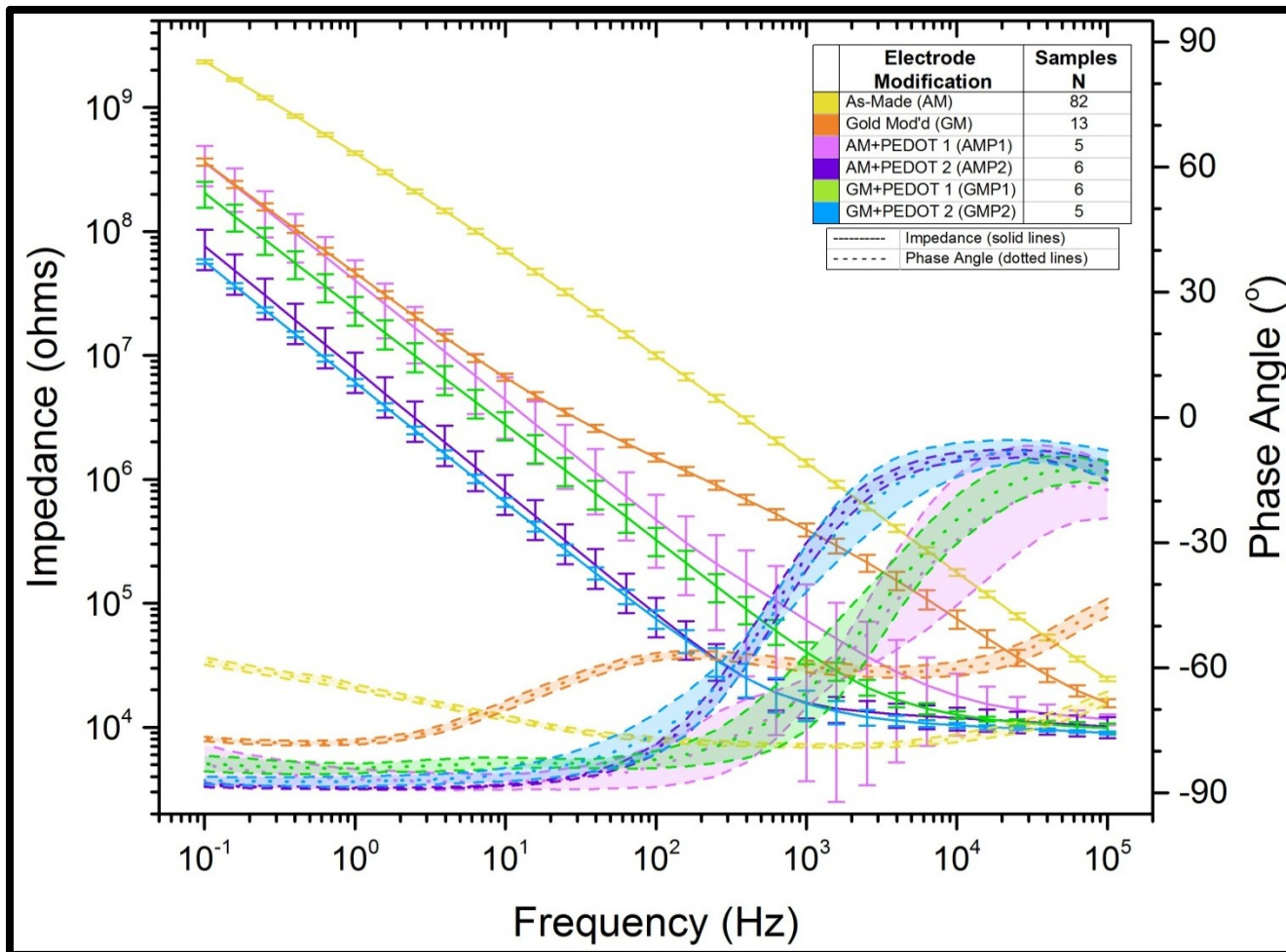


**Figure 43** – Average impedance and phase angle vs. frequency curves for each modification type from the ‘N’ single-test measurements of individual 30  $\mu\text{m}$  electrodes of that type. Error bars represent standard deviation within the sample set. (0.1 to 100,000 Hz at 10  $\text{mV}_{\text{RMS}}$  AC in 1M PBS at room temperature in low noise mode)

The modified electrodes underwent the lowest reduction in impedance reduction were GM and the AMP1 electrodes. In the case of 30  $\mu\text{m}$  diameter disc microelectrodes, the GMP1 modification slightly outperforms both the GM and AMP1 modifications by having the lowest impedance across the entire range of the frequency spectrum measured. The AMP1 modification type shows higher impedance than either the GM or GMP1 at frequencies around or below 20 Hz and both GMP1 and AMP1 outperform the GM electrodes at frequencies above 20 Hz. In the 20  $\mu\text{m}$  and 30  $\mu\text{m}$  cases P2 lowered the electrode impedance the most on AM or GM electrodes. For 30  $\mu\text{m}$  electrodes, however, the GMP2 modification impedance measured lower or matched the impedance to the AMP2 modified electrodes across the whole frequency spectrum. Interestingly, the 20  $\mu\text{m}$  electrode AMP2 and GMP2 modifications converge and are essentially equivalent below a frequency of 20 Hz. However, above 20 Hz the impedance of the GMP2 is lowest.

Regarding the phase angle curves, both the AM 20 and AM 30 electrodes start at  $< -70^\circ$  at a frequency of  $10^5$  Hz indicating that the impedance is two thirds capacitive and one third real resistance. As the frequency is reduced below 10 Hz, the phase angle trends up as oppositely charged ions in hydration sheaths begin having enough time to undergo, or at least start to undergo, mass transport due to the electromotive force (EMF), and then as the polarization switches the mass transport reverses itself. As the frequency approaches DC the resistance in the solution due to mass transport and the phase angle becomes less capacitive and more resistive with a phase angle around  $-60^\circ$ .

GM 20 and GM 30 both exhibit similar shapes with their phase angle curves, with a peak phase angle around  $-50^\circ$  around the frequency range of 200-300 Hz where the impedance included the most real resistance, possibly in a fashion similar to that of the AM electrodes but much more proximally to the GM

interface since the electric field is alternating too quickly for the ions to transport away a significant amount.

Interestingly, with the addition of even the thinnest PEDOT layer, P1, all four PEDOT modified electrode types exhibit phase angles in the range of  $-10^\circ$  to  $-20^\circ$  at the highest frequency ( $10^5$  Hz), indicative of real resistance being the primary contribution to impedance and capacitance making up the remainder. This is likely due to the PEDOT modifications' high electrochemical surface area and the small counter-ion ( $\text{ClO}_4^-$ ) being mobile enough to manoeuvre in and out of the space-charged regions around the PEDOT, allowing resistive, ohmic charge transfer to occur along with some capacitance. As the frequency is lowered into the LFP range, all 4 PEDOT modified electrodes of both sizes seem to have their phase angles drop down to very near  $-90^\circ$ , (indicative of purely capacitive impedance) and remains there as frequency is reduced from around 100-200 to 0.1 Hz. The 20  $\mu\text{m}$  diameter electrodes don't reach a phase angle of  $-90^\circ$ ; however I suspect that this is another example of mass transport limitations creating solution resistance around the electrode.

In Table 9, below, the logarithm of impedance ( $\log_{10}(Z)$ ) and the phase angle (between  $-90^\circ$  and  $+90^\circ$ ) for all the electrode sizes and modifications at the frequencies 1000, 100, 10, 1 and 0.1 Hz are provided. These frequencies were selected because they are roughly related to the detection frequency for APs (1000 Hz) and LFP rhythm bands ( $\gamma$ ,  $\alpha$ ,  $\theta$ ,  $\delta$ , respectively).

**Table 10** – Impedance and Phase Angle Values for the Various Sizes and Types of Electrode at a Selection of Relevant Frequencies

Freq. (Hz)	EIS Result	AM	GM	AMP1	GMP1	AMP2	GMP2
		20 $\mu\text{m}$					
1k (AP)	$\log_{10}Z (\Omega)$	6.223 $\pm$ 5.8	5.726 $\pm$ 4.8	4.986 $\pm$ 4.1	5.002 $\pm$ 4.0	4.692 $\pm$ 4.6	4.380 $\pm$ 3.2
	P ( $^{\circ}$ )	-76.38 $\pm$ 1.8	-56.66 $\pm$ 1.3	-75.80 $\pm$ 2.3	-76.20 $\pm$ 1.3	-49.23 $\pm$ 16	-45.85 $\pm$ 3.4
100 ( $\gamma$ )	$\log_{10}Z (\Omega)$	7.096 $\pm$ 6.3	6.272 $\pm$ 4.9	5.952 $\pm$ 5.0	5.937 $\pm$ 4.8	5.477 $\pm$ 5.4	5.202 $\pm$ 4.2
	P ( $^{\circ}$ )	-75.70 $\pm$ 1.2	-52.85 $\pm$ 2.5	-86.97 $\pm$ 0.3	-82.03 $\pm$ 1.7	-70.88 $\pm$ 19	-80.67 $\pm$ 1.7
10 ( $\alpha/\beta$ )	$\log_{10}Z (\Omega)$	7.890 $\pm$ 6.9	6.921 $\pm$ 5.0	6.939 $\pm$ 6.1	6.832 $\pm$ 5.9	6.172 $\pm$ 5.0	6.158 $\pm$ 4.9
	P ( $^{\circ}$ )	-65.31 $\pm$ 2.9	-67.28 $\pm$ 0.6	-87.81 $\pm$ 0.6	-79.74 $\pm$ 2.5	-79.37 $\pm$ 16	-85.67 $\pm$ 0.9
1 ( $\delta$ )	$\log_{10}Z (\Omega)$	8.549 $\pm$ 7.4	7.766 $\pm$ 5.7	7.912 $\pm$ 7.1	7.740 $\pm$ 6.8	7.136 $\pm$ 6.1	7.119 $\pm$ 6.0
	P ( $^{\circ}$ )	-55.00 $\pm$ 1.9	-76.73 $\pm$ 0.8	-86.43 $\pm$ 1.6	-82.03 $\pm$ 2.1	-87.67 $\pm$ 2.2	-86.76 $\pm$ 0.6
0.1 ( $\theta$ )	$\log_{10}Z (\Omega)$	9.187 $\pm$ 7.8	8.650 $\pm$ 7.1	8.870 $\pm$ 8.2	8.661 $\pm$ 7.6	8.124 $\pm$ 7.1	8.090 $\pm$ 7.0
	P ( $^{\circ}$ )	-58.22 $\pm$ 1.7	-77.22 $\pm$ 2.0	-80.93 $\pm$ 2.3	-80.62 $\pm$ 1.2	-87.57 $\pm$ 0.7	-85.72 $\pm$ 1.0
		30 $\mu\text{m}$					
1k (AP)	$\log_{10}Z (\Omega)$	6.134 $\pm$ 5.0	5.594 $\pm$ 4.7	4.862 $\pm$ 4.8	4.607 $\pm$ 3.9	4.199 $\pm$ 3.6	4.189 $\pm$ 3.6
	P ( $^{\circ}$ )	-78.66 $\pm$ 0.4	-59.61 $\pm$ 1.4	-66.15 $\pm$ 3.4	-65.97 $\pm$ 9.2	-33.29 $\pm$ 3.3	-36.18 $\pm$ 5.6
100 ( $\gamma$ )	$\log_{10}Z (\Omega)$	6.999 $\pm$ 5.8	6.177 $\pm$ 5.1	5.674 $\pm$ 5.5	5.510 $\pm$ 4.9	4.914 $\pm$ 4.5	4.874 $\pm$ 4.1
	P ( $^{\circ}$ )	-77.12 $\pm$ 0.6	-57.31 $\pm$ 0.9	-83.48 $\pm$ 5.1	-82.01 $\pm$ 2.1	-79.48 $\pm$ 1.2	-75.80 $\pm$ 4.9
10 ( $\alpha/\beta$ )	$\log_{10}Z (\Omega)$	7.843 $\pm$ 6.5	6.825 $\pm$ 5.7	6.642 $\pm$ 6.4	6.443 $\pm$ 5.9	5.902 $\pm$ 5.5	5.816 $\pm$ 4.7
	P ( $^{\circ}$ )	-71.99 $\pm$ 0.6	-69.18 $\pm$ 1.2	-87.31 $\pm$ 1.9	-82.86 $\pm$ 1.4	-88.16 $\pm$ 0.2	-85.61 $\pm$ 1.6
1 ( $\delta$ )	$\log_{10}Z (\Omega)$	8.633 $\pm$ 7.2	7.667 $\pm$ 6.5	7.606 $\pm$ 7.3	7.369 $\pm$ 6.8	6.891 $\pm$ 6.5	6.782 $\pm$ 5.6
	P ( $^{\circ}$ )	-64.73 $\pm$ 0.7	-77.79 $\pm$ 0.6	-86.70 $\pm$ 2.5	-84.11 $\pm$ 1.2	-88.91 $\pm$ 0.2	-87.26 $\pm$ 1.2
0.1 ( $\theta$ )	$\log_{10}Z (\Omega)$	9.370 $\pm$ 7.9	8.562 $\pm$ 7.4	8.558 $\pm$ 8.1	8.309 $\pm$ 7.7	7.881 $\pm$ 7.5	7.758 $\pm$ 6.4
	P ( $^{\circ}$ )	-58.34 $\pm$ 0.9	-77.06 $\pm$ 0.5	-83.31 $\pm$ 4.8	-83.00 $\pm$ 1.9	-88.12 $\pm$ 0.5	-87.02 $\pm$ 0.9

## 4.11 - SUMMARY OF WORK

One of my primary experimental objectives in Chapter 4 was to take the  $\mu$ ECoG neural probes fabricated in Chapter 3 and electrochemically modify both the 20  $\mu\text{m}$  and 30  $\mu\text{m}$  diameter microelectrode sizes. These modifications were made by electrochemically depositing one of two thicknesses of PEDOT<sup>+</sup>/ClO<sub>4</sub><sup>-</sup>, P1 or P2, onto either AM electrodes or GM electrodes pre-modified with an electrodeposited adhesion layer of rough, polycrystalline gold.

Rough gold was electrochemically deposited onto approximately half of the total microelectrodes to explore the impact on the adhesion of the subsequent PEDOT<sup>+</sup>/ClO<sub>4</sub><sup>-</sup> layers. Gold was deposited from an aqueous, de-oxygenated, 25 mM HAuCl<sub>4</sub> • nH<sub>2</sub>O and 20 g/L PVP 40 electrolyte solution by transferring a set amount of charge, -17.35 and -7.7  $\mu\text{C}$  for 30 and 20  $\mu\text{m}$  electrodes, respectively, to obtain consistent layer thickness between the two electrode diameters. A 690 s long constant-current deposition at a current-density -3.54 mA/cm<sup>2</sup> was performed in a 3-electrode cell using an Ag|AgCl RE and a Pt wire CE.

PEDOT<sup>+</sup>/ClO<sub>4</sub><sup>-</sup> microelectrodes were electrochemically deposited from a non-aqueous ACN electrolyte solution with a composition of 0.01 M EDOT and 0.1 M LiClO<sub>4</sub> in a 3-electrode cell using a non-aqueous Ag|Ag<sup>+</sup> RE and a Pt wire CE. One of two layer thicknesses of PEDOT was deposited onto each microelectrode at a constant current-density of 0.5 mA/cm<sup>2</sup> for either 24s or 118s for the thin or thick deposit; respectively. As with the gold layer, the layer thickness was controlled by controlling the quantity of charge transferred during the constant-current process.

The final microelectrode interfaces obtained for both the 20 and 30  $\mu\text{m}$  electrodes were: AM, GM, AMP1, AMP2, GMP1 and GMP2. Cleaned by consecutive 2 min ultrasound baths in acetone, IPA and DI, the  $\mu$ ECoG probes

were then carefully blown dry with pure N<sub>2</sub> gas and visually inspected with optical microscopy.

The electrode-electrolyte interface impedances of the various modified and unmodified electrodes were performance-tested by EIS (10<sup>-1</sup> to 10<sup>5</sup> Hz, 10 mV<sub>RMS</sub> AC, 5 mV steps) within the pseudo-biological medium of 1 M PBS. Cleaned and blown dry again, the devices were then placed back into their respective storage containers to await further experimental use.

Based on the results of the EIS testing performed:

- I found AM electrodes have the highest impedance values relative to otherwise modified electrodes. This is most likely due to the AM electrode type having the lowest electrochemical surface area.
- My expectation was that 20 μm electrodes would always have higher impedance than 30 μm electrodes of the same type. However, the 30 μm AM electrode performed worse at 0.1 Hz and 1 Hz than the 20 μm AM electrodes. Otherwise, the AM electrode impedance is higher in the case of 20 μm electrodes at frequencies greater than 1 Hz.
- Quantity of PEDOT deposited made a big difference in lowering impedance regardless of adhesion layer deposited or not.
- I found slightly lower impedance across the board with the GM adhesion layer. (Not a significant amount.)
- Rather impressively, although not necessarily useful evidence, GMP2 went from a phase angle of nearly -90° (purely capacitive charge transfer) at 0.1 Hz to -10° at 100 kHz (0° is indicative of ohmic charge transfer).

In the next chapter, the physical properties of the modified and unmodified electrodes will be characterized in more detail, in order to gauge their suitability for use as neural interfaces.

---

**CHAPTER 5 - DEFLECTION MODELING**  
**AND TESTING OF MODIFIED AND**  
**UNMODIFIED  $\mu$ ECOG ELECTRODES**

---

## 5.1 - INTRODUCTION

In Chapter 5 I will concentrate on the investigation into Chapter 4's electrochemical modifications to the microelectrodes of the flexible  $\mu$ ECoG probes designed and fabricated for this experimental work as detailed in Chapter 3. This includes the measurement and analysis of the physical dimensions of the microelectrode features; the likelihood of delamination of the PEDOT layer based on: 1) the PEDOT layer thickness, 2) presence of an adhesion layer and 3) electrode diameter; the magnitude of deflection required for direct electrode contact measured through experimental testing; and lastly, a mathematical model that predicts the magnitude of deflection required for direct electrode contact, allowing for evaluation of the model for accuracy by comparison of the predictions to the deflection testing results.

Imagine if two flexible, unmodified  $\mu$ ECoG neural probes made using P-C as the structural matrix were placed gently into sub-dural contact with the human cerebral cortex and one of the probes had a base layer significantly thicker than the other (e.g. 25  $\mu\text{m}$  and 2  $\mu\text{m}$ ), the thinner probe would be more flexible, and would therefore conform better to the surface.<sup>81,106,107,128</sup> Good conformity of the probe to the tissue is the first step necessary to minimize the distance between the array of recording electrodes and the signal sources, thereby maximizing the fidelity (or signal quality) of the recorded signal for the devices electrode interface depths.<sup>67</sup>

The minimum thickness for pinhole-free P-C has been reported to be 2  $\mu\text{m}$ .<sup>67</sup> Fabricating flexible  $\mu$ ECoG's at this minimal thickness, leading  $\mu$ ECoG development teams, such as the NeuroGrid research team, for example, have shown excellent conformity with their 4  $\mu\text{m}$  thick P-C  $\mu$ ECoG probe (2  $\mu\text{m}$  base layer and 2  $\mu\text{m}$  insulating layer thicknesses).<sup>67</sup> Once conformed to the undulating of sulci and gyri of the brain's tissue as best as they can, given the limitation imposed by the 2  $\mu\text{m}$  minimum thickness of the insulating P-C layer,

an open space still remains between the microelectrodes and the tissue. These open spaces are a necessity of  $\mu$ ECoG probe design and were created by plasma etching in the fabrication process to expose the electrode surfaces (these have been referred to as VIA-wells throughout this work).<sup>129</sup>

The VIA-wells in the  $\mu$ ECoG design within this work have cylindrical dimensions based on the insulating layer thickness and the microelectrode disc diameter. As the size of and spacing between the microelectrodes is decreased, if the insulating material (P-C in this case) has a limited minimum layer thickness value, there will eventually be a set of critical dimensions that prevents direct contact between the microelectrode and the tissue below. Figure 44, below has been provided to visually demonstrate this concept with two circles (representing the neural tissue) of equal radius lowered as much as possible into two VIA-wells of different diameters and equal interface depths.

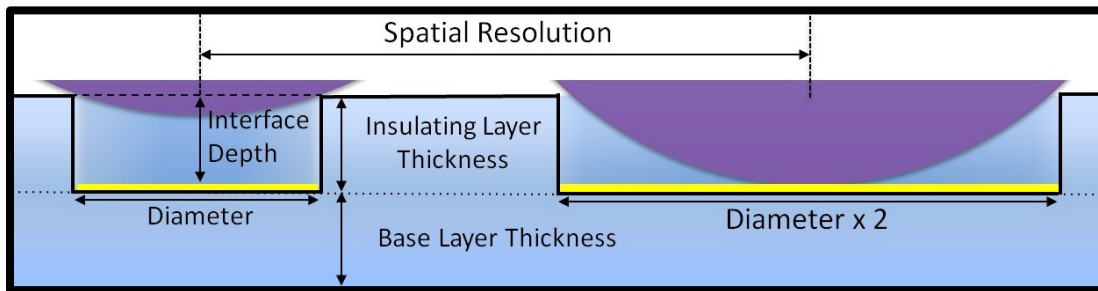


**Figure 44** – An illustration qualitatively demonstrating the existence of “limiting dimensions” for VIA-wells in  $\mu$ ECoG probes. Shown are two identical purple circles trying to make contact with the two gold microelectrodes at the bottoms of their respective VIA-wells. The smaller diameter VIA-well has prevented direct contact while one twice its diameter has allowed it.

The main concern and purpose of this research, is exploring whether the microelectrode diameters currently being fabricated ( $\leq 30 \mu\text{m}$ ) by the leaders in neural probe technology have crossed that critical threshold for their VIA-wells. If so, this could indicate a requirement of some additional means for overcoming this physical gap that reduces the fidelity of the acquired signals and therefore permanently limits the overall device performance.<sup>1,64,67,130,131</sup>

The issue concerning the critical dimensions of neural probes has been raised and investigated previously by Prohasaka, et al., regarding rigid, planar, Si-based, shank-type intracortical probes.<sup>66</sup> The investigators found that insulating layer thickness, conducting pathway width and electrode size all contribute to limiting the performance of the device once certain size scales are reached.<sup>66</sup> To my knowledge, the critical dimensions of VIA-wells for direct electrode-tissue contact, beyond which the insufficient deflection prevents direct contact, have yet to be raised as concerns or considerations for the performance of future generations of  $\mu$ ECoG probes in recent fabrication publications. However, it is my belief that this issue is very important to consider, especially with fabrication efforts trending towards fabricating smaller diameter microelectrodes in much greater number at high densities in order to facilitate higher spatial resolution devices with as many recording sites as possible.<sup>64,68,132,133</sup> As electrode diameters continue to decrease, without ensuring direct tissue-electrode contact is being made, state-of-the-art  $\mu$ ECoG probe performance may be unknowingly limited and unable to record from the neo-cortex with the maximum signal-to-noise ratio (SNR) or full signal bandwidth.<sup>23,68,134</sup>

Proposed in the thesis of this experimental work, one solution to this tissue-electrode contact problem is the reduction of interface depth through the electrochemical deposition of the performance enhancing electrode material PEDOT (as was described in Chapter 4). In addition to modifying the electrical properties of the electrodes, the intention was to fill the VIA-wells in using these PEDOT deposits and reduce the effective interface depth from the plane of the insulation layer (which would be in complete contact with the surface due to its excellent conformity) to an effective height (as predicted mathematically or found empirically).

PEDOT was the material of choice because it's often used as an electrode coating in new neural probes, due to its high ionic and electronic conductivity

and biocompatibility.<sup>95,105</sup> However, PEDOT has been reported to delaminate from microelectrode surfaces as the thickness of the layer increases, especially with small-area microelectrodes.<sup>97,114</sup> Mechanical delamination occurs when the thin-film layer's thickness passes a point where the internal stresses within the film exceed the adhesive force holding it to the electrode surface.<sup>129,135</sup> Through the addition of a pre-deposited gold adhesion layer (or LASER micro-patterning or otherwise roughening the electrode surface) the maximum PEDOT layer achievable without mechanical delamination increases, enabling adhesion of thicker depositions.<sup>97,135</sup> To explore the necessity and efficacy of a gold adhesion layer, one of two thicknesses of PEDOT was electrochemically deposited directly onto the gold microelectrodes described in Chapter 4; (1) as-made (AM) (sputtered) gold electrodes or (2) gold-modified (GM) electrodes with electrochemically deposited gold adhesion layers. (See Table 11, below)

**Table 11** – Microelectrode Modification (Mod.) Status ID Codes

<b>Condition of Gold Electrode</b>	<b>PEDOT Mod.</b>	<b>Diameter (μm)</b>	<b>Mod. ID Code</b>
As-Made Sputtered <b>AM</b>	N/A	<b>20</b>	<b>AM 20</b>
As-Made Sputtered <b>AM</b>	N/A	<b>30</b>	<b>AM 30</b>
Gold Adhesion Mod. <b>GM</b>	N/A	<b>20</b>	<b>GM 20</b>
Gold Adhesion Mod. <b>GM</b>	N/A	<b>30</b>	<b>GM 30</b>
As-Made Sputtered <b>AM</b>	Thin PEDOT <b>P1</b>	<b>20</b>	<b>AMP1 20</b>
As-Made Sputtered <b>AM</b>	Thin PEDOT <b>P1</b>	<b>30</b>	<b>AMP1 30</b>
As-Made Sputtered <b>AM</b>	Thick PEDOT <b>P2</b>	<b>20</b>	<b>AMP2 20</b>
As-Made Sputtered <b>AM</b>	Thick PEDOT <b>P2</b>	<b>30</b>	<b>AMP2 30</b>
Gold Adhesion Mod. <b>GM</b>	Thin PEDOT <b>P1</b>	<b>20</b>	<b>GMP1 20</b>
Gold Adhesion Mod. <b>GM</b>	Thin PEDOT <b>P1</b>	<b>30</b>	<b>GMP1 30</b>
Gold Adhesion Mod. <b>GM</b>	Thick PEDOT <b>P2</b>	<b>20</b>	<b>GMP2 20</b>
Gold Adhesion Mod. <b>GM</b>	Thick PEDOT <b>P2</b>	<b>30</b>	<b>GMP2 30</b>

To examine the effect filling the VIA-wells had on the various aspects of microelectrode performance, precise measurements of the interface depths

were first required. Atomic force microscopy (AFM) was used to examine both the as-made and electrochemically-modified  $\mu$ ECoG electrodes, determining the physical dimensions of the VIA-wells and the surface quality of the microelectrodes they enclose.

AFM data on the electrode interface depths was collected at all stages of modification for all electrode types and both diameters, the layer thickness of the gold and PEDOT depositions were calculated prior to the adhesion testing that was performed.

AFM data was then imported into analysis software which was used to obtain cross-sectional profiles and pixel-population depth histograms from both microelectrode diameters and each type of modification. These two methods, cross-sectional profiling and histograms, were used to obtain the average physical dimensions of the various electrode types of the devices used in the experimental adhesion and deflection tests that follow. The results were then compared and the difference between them was calculated to roughly check the consistency and validity of the measurements.

Despite the fact that the application of pressure to the brain in an unacceptable means to create tissue-electrode contact, to explore the idea of detecting sufficient deflection for direct electrode contact, deflection tests involving the application of pressure were performed under dry conditions without the ionic charge carriers within electrochemical circuits that would pre-emptively demonstrate an electrical connection in this test. The deflection tests were carried out by applying pressure to a modified  $\mu$ ECoG probe head, deflecting the various microelectrodes to some degree, in some cases into physical contact with underlying metal. Upon achieving contact at a certain pressure, the electrical circuit is completed (monitored by a multi-meter); thus demonstrating that sufficient deflection for physical contact has been achieved. The measured deflection magnitude required for electrode contact and the applied pressure under which this deflection was achieved

were then compared to deflection magnitudes and pressures predicted by a mathematical model.

To mathematically explore the probe deflection problem, an equation that predicts the central deflection magnitude in symmetrically bending circular discs when put under pressure was used as a model for predicting the deflection magnitude expected from  $\mu\text{m}$ -scale VIA-wells when various amounts of pressure are applied. The models resulting figures were then compared to the results of the deflection tests.

Finally, the results from this chapter's tests are brought together and summarized. Some discussion is made about the future work and ways of improving the types of tests in the future.

## **5.2 - ATOMIC FORCE MICROSCOPY**

### **MICROELECTRODE SURFACE CHARACTERIZATIONS**

Atomic force microscopy (AFM) is a physical characterization method that uses microscopic cantilevers to intimately interrogate surfaces and structures of interest, obtaining datasets of three-dimensional coordinates that are processed by AFM software and used to visually represent the resulting scans. The purpose of this section is to become acquainted with the physical structure and dimensions of the  $\mu$ ECoG microelectrodes that were fabricated as discussed in Chapter 3 and electrochemically modified as covered in Chapter 4.

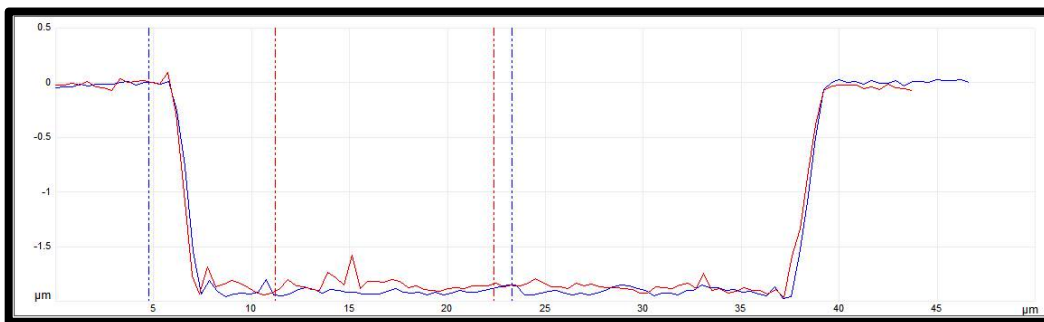
The depth of each type of electrode interface was measured relative to the surface plane of the insulating layer of matrix material (i.e. the VIA-well) and, by using multiple software analysis techniques, quantitatively approximated for the calculations of layer thicknesses needed for delamination tests, deflection tests and deflection modeling parameters.

Cross-sectional surface profiles of the VIA-wells and mean interface depths of the electrodes were obtained through investigation with AFM followed by software processing and analysis.

The characterization measurements were performed with a Dimension Edge AFM (Bruker; [www.bruker.com](http://www.bruker.com)) in tapping-mode using POINTPROBE® non-contact mode silicon SPM-sensor cantilever tips (NanoWorld; [www.nanoworld.com](http://www.nanoworld.com)). The acquired data files were digitally processed and analyzed using NanoScope Analysis v1.5 software (Bruker; [www.bruker.com](http://www.bruker.com)).

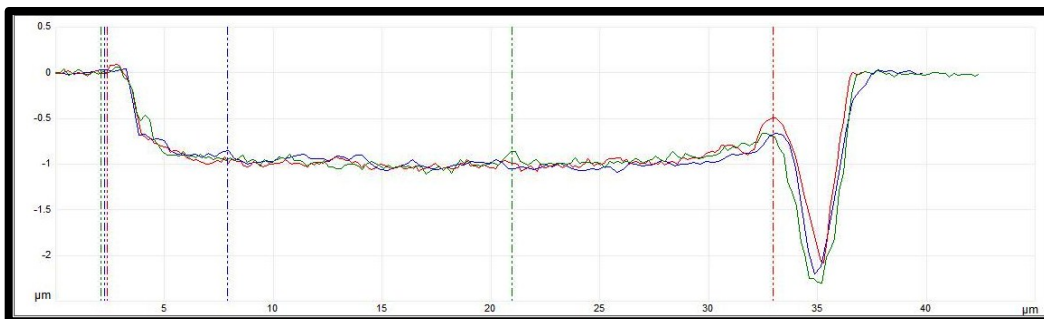
## 5.2.1 CROSS-SECTIONAL MICROELECTRODE PROFILE DEPTHS

The resulting cross-sectional profile scans representative of each of the electrode modification types are shown in Figures 45 to 50 below. Finally, the averaged results from these two investigative software-based methods, the average mean, minimum and maximum interface depths for each of the various electrode modification combinations, are combined and listed in Table 12.



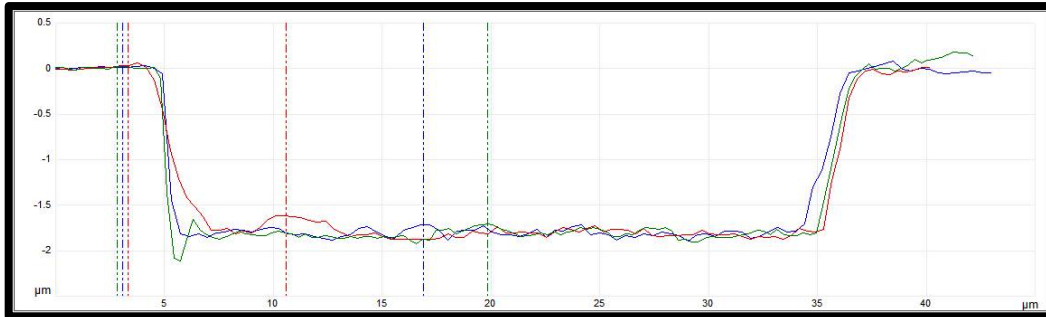
**Figure 45** – Cross-sectional VIA-well profiles of a 30  $\mu\text{m}$  'As-Made' electrode (AM) obtained through AFM.

Figure 45 indicates an average measured depth of 1.859  $\mu\text{m}$  for two 30  $\mu\text{m}$  As-Made (AM) electrodes. The electrodes overlapped in the previous figure indicate a good level of consistency between electrodes. The surface is fairly rough, qualitatively, with a few small sharp peaks but mostly long flat slopes remaining fairly horizontal.



**Figure 46** – Cross-sectional VIA-well profiles of a 30  $\mu\text{m}$  'Gold-Modified' electrode (GM) obtained through AFM.

The gold-modified (GM) microelectrode cross-section profile Figure 46, above, measures an average depth of  $0.879\ \mu\text{m}$  between the 3 marked points. The qualitative surface roughness of the GM electrode is similar to that of Figure 52, the AM electrode, but with smaller, more refined peaks and valleys, suggesting a larger number of smaller grains which would increase the surface area significantly.



**Figure 47** – Cross-sectional VIA-well profiles for a  $30\ \mu\text{m}$  AM electrode with a thin PEDOT coating (AMP1) obtained through AFM.

Figure 47 shows the VIA-well profile of an AM electrode that has been modified additionally with the thin PEDOT (P1) deposition process. From this AMP1 modified electrode, the average depth between the three markers is  $1.906\ \mu\text{m}$ . Relative to the semi-jagged AM surface, the PEDOT seems to have smoothed the surface while raising the interface slightly.

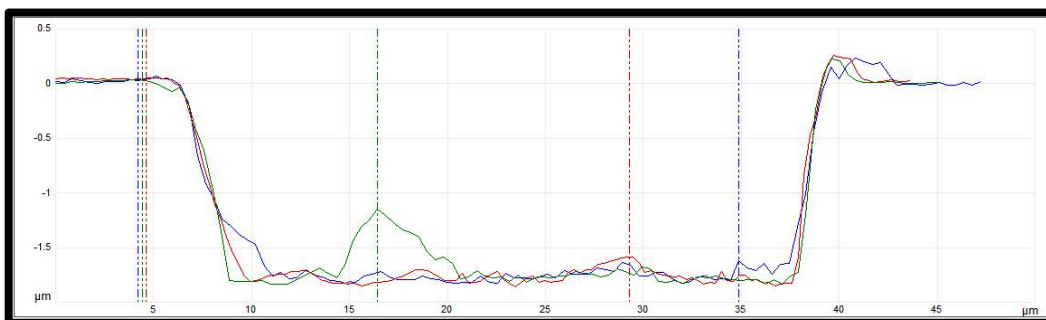


**Figure 48** – Cross-sectional VIA-well profiles of a  $30\ \mu\text{m}$  AM electrode modified with a thick PEDOT coating (AMP2) obtained through AFM.

Figure 48 shows the resulting cross-sectional profile for AM electrodes coated with the thick PEDOT layer. The average depth measured  $1.884\ \mu\text{m}$  and a high-point (shown on the green trace) that closes the gap to about  $1.175\ \mu\text{m}$ . This

modification is similar in surface quality to AMP1 electrodes but with a thicker deposition of nodular outgrowths.

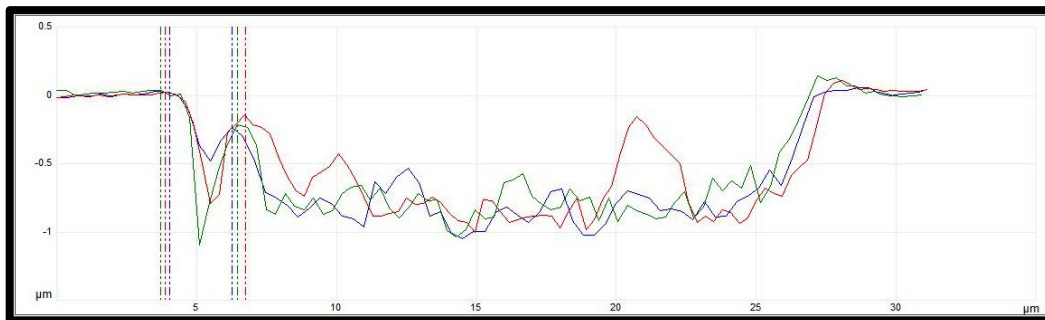


**Figure 49** – Cross-sectional VIA-well profiles of a 20  $\mu\text{m}$  GM microelectrode coated with an additional thin layer of PEDOT (GMP1) obtained through AFM.

Figure 49 shows a GM electrode subsequently modified with a thin PEDOT coating. There are large and small hill-like formations of PEDOT; some of which nearly break the plane of the insulating layer. The average maximum depth found for this electrode is 1.073  $\mu\text{m}$ , but at the tallest formations the depth is 0.161  $\mu\text{m}$ . It seems like the increased ESA from the GM has enabled more nucleation sites for PEDOT clusters to polymerize and grow upward towards the insulation surface plane.

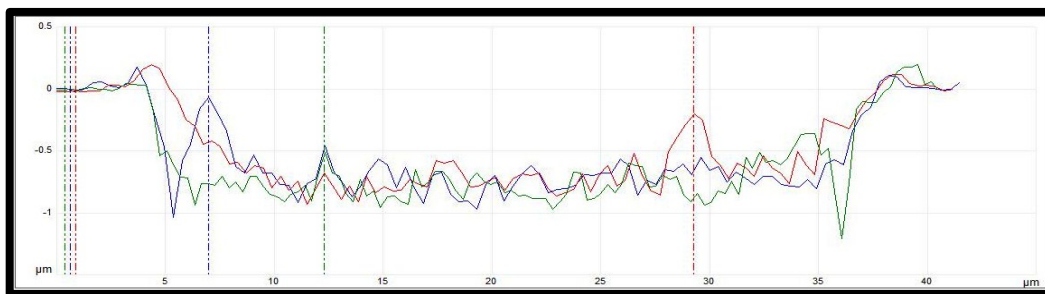


**Figure 50** – Cross-sectional VIA-well profiles of the electrode modification with the most material deposited, GM and thick PEDOT (GMP2) obtained through AFM. Red, green and blue markers placed at electrode surface peaks (i.e. points of minimal depth) measuring 0.184, 0.503 and 0.051  $\mu\text{m}$  while the maximum depth was measured to be 0.940  $\mu\text{m}$ .

The final electrode modification to be tested, GMP2, shown above in Figure 50, is visually similar to the GMP1 type of modification but has a larger number of sharp peaks and outgrowths reaching up to and sometimes past the insulating surface plane, implying reduced electrical impedance through increased

surface area and greater likelihood for tissue-electrode contact. The average interface depths for the various electrode sizes and modification types as found using the cross-sectional method of investigation are listed in Table 12, below. (N = number of electrodes measured using the cross-sectional method)

**Table 12** – Cross-Sectional Profile Electrode Interface Depth Averages

<b>Electrode Modification ID</b>	<b>Cross-Sectional Profile Interface Depth (<math>\mu\text{m}</math>)</b>	<b>N</b>
<b>AM 20</b>	1.90 $\pm$ 0.08	3
<b>AM 30</b>	1.87 $\pm$ 0.09	5
<b>GM 20</b>	0.9 $\pm$ 0.3	2
<b>GM 30</b>	1.0 $\pm$ 0.3	4
<b>AMP1 20</b>	1.7 $\pm$ 0.2	4
<b>AMP1 30</b>	1.8 $\pm$ 0.2	8
<b>AMP2 20</b>	1.61 $\pm$ 0.08	5
<b>AMP2 30</b>	1.6 $\pm$ 0.2	5
<b>GMP1 20</b>	0.9 $\pm$ 0.2	5
<b>GMP1 30</b>	1.0 $\pm$ 0.2	4
<b>GMP2 20</b>	0.8 $\pm$ 0.1	4
<b>GMP2 30</b>	0.7 $\pm$ 0.2	5

These measurements seem to demonstrate a good degree of similarity of depth between the 20 and 30  $\mu\text{m}$  electrodes modified with the same method. The gold modified electrodes have the most relative error. PEDOT modifications onto GM electrodes apparently compensate somewhat for this variability in electrode interface depth.

### 5.2.2 HISTOGRAM MEAN DEPTHS FROM VIA-WELLS

To confirm the accuracy of VIA-well depth approximations obtained through cross-sectional examination of electrode profiles, a second style of software analysis was performed: analysis of VIA-wells' pixel population histogram.

Initially represented visually by the analysis software, as shown in Figure 51, below, an array of colorized pixels can be seen indicating their relative depths through the pixel brightness.

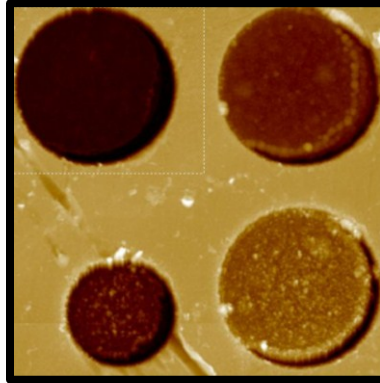


**Figure 51** – Visualization from the height sensor AFM data within a 75  $\mu\text{m}$  by 75  $\mu\text{m}$  scan area; showing 4 electrodes surrounded by a P-C matrix with interfaces at varying depths, as darker areas are relatively deeper than brighter areas.

In this approach to measuring depth, a selected subset of the AFM data was reprocessed into a histogram based on the pixel population (or populations). Relative height values (represented by each pixel's brightness in the above figure) within a selected region is represented visually as shown in Figure 52, below.

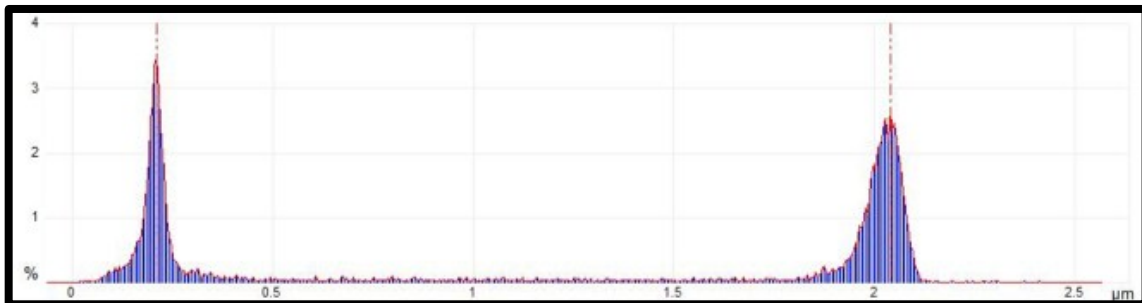


**Figure 52** – Histograms of the AFM image's pixel-population showing two distinct population sets. The relative separation between population-means is considered as the interface depth. (e.g. 'As-Made' interface depth of 1.828  $\mu\text{m}$ )

With large percentages of pixels sharing the same or similar depths, the data points tend to form into two large clusters: one representing the top-plane of the P-C and the other representing the electrode plane. The separation was

then calculated by placing markers between the means of the two peaks and this value was taken as the mean interface depth.

It was important for accurate measurements that the matrix material surrounding the electrodes be planar (appears homogenous or uniform in colour) because the narrow distributions can become skewed or broadly distributed, making the placement of the red marker lines difficult and introducing much more uncertainty into the resulting data. This method was used to on each microelectrode type on multiple probes to obtain an average mean interfacial depth for each microelectrode type (see Table 13, below). (N = number of electrodes measured using the pixel population mean separation method.)

**Table 13** – Average Pixel Population Mean Interface Depth for Each Microelectrode Type

<b>Electrode Mod. ID</b>	<b>Average Pixel Population Mean Interfacial Depth (µm)</b>			<b>N</b>
<b>AM 20</b>	1.88	±	0.07	6
<b>AM 30</b>	1.85	±	0.07	10
<b>GM 20</b>	0.9	±	0.2	6
<b>GM 30</b>	0.9	±	0.2	9
<b>AMP1 20</b>	1.76	±	0.09	2
<b>AMP1 30</b>	1.76	±	0.04	4
<b>AMP2 20</b>	1.53	±	0.08	2
<b>AMP2 30</b>	1.45	±	0.02	4
<b>GMP1 20</b>	0.86	±	0.07	3
<b>GMP1 30</b>	0.91	±	0.08	5
<b>GMP2 20</b>	0.6	±	0.1	2
<b>GMP2 30</b>	0.54	±	0.07	4

The results from this method indicate that the objective of obtaining varying interface depths has been successful and the diameter hasn't significantly

affected the equality and comparability of modification layer thicknesses between electrode sizes.

### 5.2.3 COMPARISON OF CROSS-SECTIONAL PROFILE AND HISTOGRAM MEAN DEPTHS

Comparing the two software methods used to see what level of similarity they had in their outcomes allowed for validation of the calculated values from the two methods. Similarity in measured values could also be argued to imply accuracy of the measurements. The cross-sectional profile interface depths and the mean interface depth from the histogram method were averaged across the ‘N’ electrodes measured by AFM and are listed by electrode size and type below in Table 14. (N1, N2 = number of electrodes measured by cross-sectional profile inspection and by separation of pixel population means, resp.)

**Table 14** – Summarized Electrode Interface Depth Data Showing Both AFM-Based Analysis Results and the Calculated Average of the Two Methods

Mod. Type ID	Cross-Sectional Profile Depth (μm)	N1	Pixel Population Mean Interface Depth (μm)	N2	Average Interface Depth (μm) (N = 2)
AM 20	1.90 ± 0.08	3	1.88 ± 0.07	6	1.89 ± 0.08
AM 30	1.87 ± 0.09	5	1.85 ± 0.07	10	1.86 ± 0.08
GM 20	0.9 ± 0.3	2	0.9 ± 0.2	6	0.9 ± 0.3
GM 30	1.0 ± 0.3	4	0.9 ± 0.2	9	1.0 ± 0.3
AMP1 20	1.7 ± 0.2	4	1.76 ± 0.09	2	1.7 ± 0.1
AMP1 30	1.8 ± 0.2	8	1.76 ± 0.04	4	1.8 ± 0.1
AMP2 20	1.61 ± 0.08	5	1.53 ± 0.08	2	1.57 ± 0.08
AMP2 30	1.6 ± 0.2	5	1.45 ± 0.02	4	1.5 ± 0.1
GMP1 20	0.9 ± 0.2	5	0.86 ± 0.07	3	0.9 ± 0.1
GMP1 30	1.0 ± 0.2	4	0.91 ± 0.08	5	0.9 ± 0.1
GMP2 20	0.8 ± 0.1	4	0.6 ± 0.1	2	0.7 ± 0.1
GMP2 30	0.7 ± 0.2	5	0.54 ± 0.07	4	0.6 ± 0.1

As expected, there was generally fairly good agreement between depth measurements collected using the two different methods, which validated the assumption that the profile and histogram methods were both fairly accurate.

The difference between the measurements could be due to inconsistencies in the interface surface itself, such as the roughness and presence of non-uniform outgrowths. Alternatively, the difference could be due to skewing and broadening of the histogram peak that represents the electrode plane due to surface roughness, making the placement of the right-hand marker very difficult, causing slightly more or less depth to be calculated.

### **5.3 - PEDOT DELAMINATION STUDIES**

In this section, the thicknesses of the deposited layers were roughly estimated by subtractive before-and-after AFM measurements of modified electrode surfaces. Resulting thickness estimates for each layer of electrodeposited material were then used to predict delamination since the thicker the PEDOT layer, the more likely it is to delaminate spontaneously.<sup>114</sup> The likelihood of the modified probes' layers delaminating was then investigated through destructively testing the modified probes using a "tape-test" method of testing thin-film layer adhesion.

The purpose of this section is to gain insight into the effectiveness of a rough, gold adhesion layer and the influence the PEDOT layer thickness has on that effectiveness. With the knowledge of the various interface depth values, the thickness of both the gold and PEDOT modification layer thicknesses are calculated to correlate to any delamination observed during the tests.

### 5.3.1 RESULTS AND DISCUSSION: MODIFICATION LAYER THICKNESSES

The initial and final depths of each electrode type were collected from numerous devices and electrodes, as approximated through the AFM methods detailed previously, and averaged by size and type. The two values,  $d_{initial}$  and  $d_{final}$ , allowed for the calculation of deposition layer thickness ( $t_{layer}$ ) using Equation 5.1 (below).

$$t_{layer} = d_{initial} - d_{final} \quad [5.1]$$

The average deposition thickness for each microelectrode size and type was calculated and listed below in Table 15. (N = the number of depth measurements of individual electrodes that were used in the calculation.)

**Table 15** – Electrochemically Deposited Layer Thickness Approximations From Calculations Based on the Average of the AFM Methods Used to Measure Depth

Electrode Mod. ID	Approximated Layer Thickness ( $\mu\text{m}$ )	N
GM-20	0.99 $\pm$ 0.08	6
GM-30	0.97 $\pm$ 0.08	9
AMP1-20	0.07 $\pm$ 0.04	10
AMP1-30	0.08 $\pm$ 0.02	18
AMP2-20	0.32 $\pm$ 0.03	10
AMP2-30	0.37 $\pm$ 0.05	19
GMP1-20	1.0 $\pm$ 0.1	6
GMP1-30	1.0 $\pm$ 0.1	9
GMP2-20	1.2 $\pm$ 0.1	5
GMP2-30	1.2 $\pm$ 0.1	10

### 5.3.1.1 GOLD ADHESION LAYER THICKNESSES

Since the total coulombic transfer of charge was specified, controlled and charge transfer density was kept equal between the 20  $\mu\text{m}$  and the 30  $\mu\text{m}$  electrodes, I expected to get roughly comparable layer thicknesses for both sizes. Obviously the 20  $\mu\text{m}$  layer thicknesses aren't exactly equal to the 30  $\mu\text{m}$  but the closeness of the values to each other and the small standard deviation leads me to believe that the methods used to acquire these coatings (see Chapter 4) are repeatable and consistent. I was expecting the 20  $\mu\text{m}$  layers to be slightly thicker than the 30  $\mu\text{m}$  layers but there does not appear to be any trend discernible with respect to the smaller electrodes discs' coatings being thicker than their slightly larger AM counterparts, nor the GM or the PEDOT modified electrodes.

### 5.3.1.2 PEDOT LAYER THICKNESSES

The thin PEDOT modification layer (P1) thicknesses on as-made (AM) gold electrodes were found to be  $0.07 \pm 0.04 \mu\text{m}$  and  $0.08 \pm 0.02 \mu\text{m}$  for the 20 and 30  $\mu\text{m}$  diameter electrodes, respectively. The thicker PEDOT modification layer (P2) thicknesses on AM gold electrodes were found to be  $0.32 \pm 0.03 \mu\text{m}$  and  $0.37 \pm 0.05 \mu\text{m}$  for the 20 and 30  $\mu\text{m}$  diameter electrodes, respectively. At average thicknesses of roughly 75 nm and 350 nm (20  $\mu\text{m}$  and 30  $\mu\text{m}$ , respectively,) the thicknesses achieved were both 50% of the expected thicknesses stated in the deposition parameters.

The thin PEDOT modification layer (P1) thicknesses on the surface-roughened gold-modified (GM) electrodes were found to be  $0.01 \pm 0.02 \mu\text{m}$  and  $0.03 \pm 0.02 \mu\text{m}$  for the 20 and 30  $\mu\text{m}$  diameter electrodes, respectively. The thicker PEDOT modification layer (P2) thicknesses on GM electrodes were found to be  $0.21 \pm 0.02 \mu\text{m}$  and  $0.23 \pm 0.02 \mu\text{m}$  for the 20 and 30  $\mu\text{m}$  diameter electrodes, respectively. With average thicknesses of roughly 25 nm and 220 nm, both these layer thicknesses were over 80% less thick than predicted previously.

### 5.3.1.3 COMBINED LAYER THICKNESSES

For the combined layer thicknesses, i.e. the GMP1 and GMP2 electrodes, both the 20 and 30  $\mu\text{m}$  diameters were calculated based on the AFM measurements to be  $1.0 \pm 0.1 \mu\text{m}$  and  $1.2 \pm 0.1 \mu\text{m}$ , respectively. The apparent decrease in PEDOT layer thickness, when compared to the GM layer thicknesses and the AMP1 and AMP2 PEDOT layer thicknesses listed in Table 14, above, is likely due to the high surface roughness and inconsistently or poorly chosen points from which the depth measurements were made in the AFM software. It is possible that with increased ESA from the gold modification, the thickness of PEDOT deposited decreased due to a reduced flux of charge as the constant current depositions had the desired current calculated based on the GSA of the microelectrodes, and did not account for the actual increase in ESA that had occurred during the gold modification process. Another possible explanation for this apparent decrease is human error in the selection of the points from which depth measurements were taken on both the GM and GMP1/GMP2 AFM profiles due to the high surface roughness.

## 5.3.2 MATERIALS AND METHODS: DELAMINATION

### TESTING

The thicker a PEDOT layer is, the more likely it is to delaminate from its base electrode spontaneously or due to some impetus providing the needed ‘activation’ energy to the internal film stresses that increase with layer thickness.<sup>114</sup> Delamination testing on the  $\mu\text{ECoG}$  probes fabricated and subsequently modified electrochemically as described in previous chapters was performed to observe any evidence that PEDOT delamination can be prevented or inhibited by an adhesion layer. The microelectrode VIA-wells were carefully measured by AFM after the fabrication and before and after each electrochemical modification since delamination testing is destructive and irreversible.

Before and after testing was performed, a microscope image of the  $\mu$ ECoG probe heads were captured using a VHX-2000 series Keyence digital microscope equipped with a Z250R lens (Keyence Corporation; [www.keyence.ca](http://www.keyence.ca)). Scotch® tape was then fixed sticky side up onto a 1" x 2.5" microscopy slide. The tape-slide was then placed onto a weigh-scale with an operating range from 0.1 - 5 kg. A small circle (0.5 cm diameter) was drawn onto the sticky tape-slide to aid in localizing any delaminated layers after the test was completed. The probe of interest was then aligned so that it was approximately centred in the drawn circle and gently placed onto the sticky surface of the tape. Once placed properly, pressure was applied to the backside of the neural probe with the tip of my index finger for a count of 5s, keeping the downward force constant on the weigh scale at 1 kg. After letting it rest for 1m the probe was peeled carefully from the tape and inspected under microscope along with the encircled area on the tape-slide.

### 5.3.3 RESULTS AND DISCUSSION: DELAMINATION STUDIES

The before and after images of the tested  $\mu$ ECoG device with 3x 20  $\mu$ m diameter and 5x 30  $\mu$ m diameter electrodes that had been modified as AMP1 or AMP2 and 3x 20  $\mu$ m diameter and 5x 30  $\mu$ m diameter electrodes that had been modified as GMP1 or GMP2 were used to visually determine whether delamination had occurred.

An example of the visual comparison carried out between the “before” (left hand side) and the “after” (right hand side) images of one of the tested devices are shown below in Figure 55. The 8 electrodes on the left side were modified with a thin layer of PEDOT (P1) and the other 8 on the right were modified with a thicker PEDOT layer (P2).

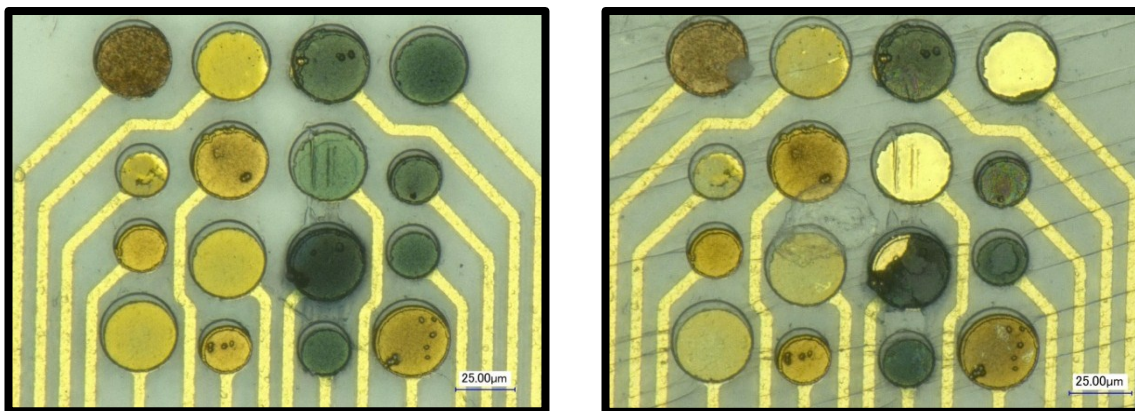


**Figure 53** – 1500x magnification micrographs of a  $\mu$ ECoG probe head before (left) and after delamination tape-tests (right).

No delamination was observed for AMP1 electrodes of both diameters, the 20  $\mu$ m GMP1 or GMP2 electrodes, although partial delamination was evident on some of the 30  $\mu$ m diameter GMP1 or GMP2 electrode types. Delamination was observed in over 70% of the 30  $\mu$ m AMP2 electrode modification type, a significant amount of modification loss within the small population of devices that were tested. Interestingly, the 20  $\mu$ m AMP2 electrodes seemed to be completely unaffected by the tape test, not even being partially delaminated, possibly due to insufficient deflection as limited by the small diameter, preventing contact from being made between the tape and the electrode.

The number of repetitions performed here was not large enough to make any strong claims, but despite that the initial findings indicate that 30  $\mu$ m diameter as-made electrodes need to be kept under a close watch. With a delamination rate just above 70%, AMP2 30 electrodes, the thick PEDOT deposition combined with a diameter of 30  $\mu$ m indicates some issue with adhesion.

The fact that no PEDOT layers completely delaminated from a gold-modified electrode (although there were a few partial losses of material), whether 20 or 30  $\mu$ m in diameter, implies that the use of an electrochemically deposited gold adhesion layer could enable thicker PEDOT layers without sacrificing adhesion, although more testing is required for more certainty.

## **5.4 - DEFLECTION UNDER PRESSURE**

This section summarizes the testing done to investigate the achievable amounts of deflection from a flexible Parylene-C  $\mu$ ECoG probe composed of a 23  $\mu\text{m}$  base layer, 120 nm thick gold-titanium (Au-Ti) metallic layer, a 1.8  $\mu\text{m}$  insulating layer and 20  $\mu\text{m}$  and 30  $\mu\text{m}$  diameter electrodes. In the previous chapter, the methods of electrochemical modification and resulting electrode types were described. As stated in the previous chapter, and demonstrated by the AFM profilometry, the various modifications have resulted in different interfacial depths for each modification type.

The applicability and accuracy of the deflection model described at the beginning of the chapter was experimentally tested with a dry electrode-electrode contact experiment in which various amounts of pressure are applied to a probe and the evidence of contact is the closure of an electrical circuit. This test was not done electrochemically, because the absence of an electrolyte through which the charge could transfer allowed for a more clear indication that sufficient deflection has occurred by the sudden formation of a closed-circuit upon contact.

The application of pressure to the brain is not a clinically acceptable solution to this problem and has only been used to demonstrate the establishment of contact in a dry environment. Upon making contact by applying pressure, the implication is that deflection caused by the application of pressure, which initiated contact. Therefore, if the amount of pressure required for contact can be reduced by filling the VIA-well by the post-fabrication addition of PEDOT and gold electrode material, then, at some point, pressure need not be applied.

## 5.4.1 MATERIALS AND METHODS: DEFLECTION TESTS

The deflection test was performed using a multi-meter with one of its leads connected to one microelectrode channel (at a time) on the ZIF-connector and the other lead connected to aluminum foil laid flat across a smooth, hard surface and held in place by tape. The  $\mu$ ECoG probe of interest is then laid face-down on top of the foil layer and the multi-meter is set to measure resistance, displaying “OL” (shorthand for “overload”) meaning that the circuit is open and no current is flowing. A force-distribution plate with a known contact area,  $A$ , to transfer the mass placed on top of it evenly across the contact surface of the plate was carefully placed on top of the backside of the  $\mu$ ECoG, as shown below in Figure 56.

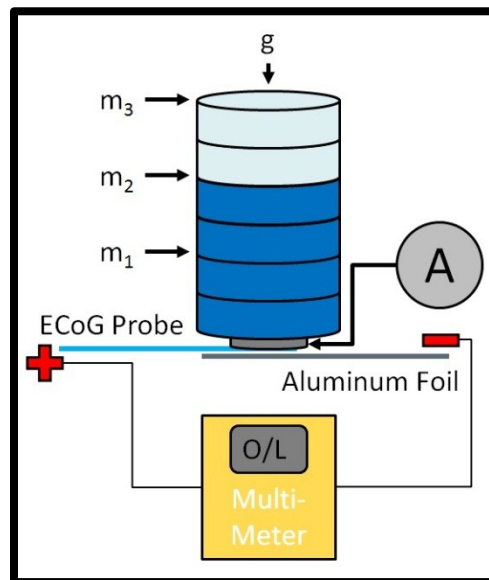


**Figure 54** - An illustration of the pressure-induced deflection testing apparatus.

As depicted in the above figure is an empty 8 L container that was then centered exactly on top of a chunk of acrylic. The mass was then incrementally increased (and with it the  $\Delta P$ ) with room temperature water (density assumed to be  $= 1 \text{ g/cm}^3$ ) as shown in Table 15, next page.

**Table 16** – Deflection Test Calculated Mass Requirements

<b>Contact Area A (m<sup>2</sup>)</b>	<b>Applied Mass (kg)</b>	<b>F<sub>g</sub> (N)</b>	<b>Pressure (kPa)</b>
7.85 x 10 <sup>-5</sup>	m <sub>1</sub> = 1	9.81	125
	m <sub>2</sub> = 5	49.05	625
	m <sub>3</sub> = 10	98.1	1250

The multi-meter display was continuously monitored for its readout to switch from “OL” (meaning overload) to some amount of electrical resistance “\_\_Ω” (because this signified current had begun flowing). As stated before, the change in display on the multi-meter was recorded as evidence of whether contact between two solid conductors had been made, making the assumption that the connection was due to the pressure being applied causing sufficient deflection. All variations of electrode modification and size were tested in this manner and the results are summarized and discussed in the next section.

## 5.4.2 RESULTS AND DISCUSSION: DEFLECTION TESTS

The deflection test results for every modification type and size of electrode are listed below in Table 17. (N = the number of single-test measurements made on individual electrodes.)

**Table 17** – Results From Deflection Under Pressure Testing of Flexible  $\mu$ ECOG Probes

Electrode Modification Type	Diameter	Average Interface Depth	# of Electrodes Tested	Contact at 125 kPa?	Contact at 625 kPa?	Contact at 1250 kPa?	Protrusion From Layer?
	$\mu\text{m}$	$\mu\text{m}$	N	%	%	%	(Y/N)
AM	20	1.879	6	0%	0%	0%	N
AM	30	1.854	10	0%	0%	0%	N
AMP1	20	1.617	3	0%	0%	0%	N
AMP1	30	1.661	5	0%	0%	0%	N
AMP2	20	1.578	3	0%	0%	0%	N
AMP2	30	1.507	5	0%	0%	20%	N
GMP1	20	0.805	3	0%	33%	67%	Y
GMP1	30	0.71	5	0%	60%	80%	Y
GMP2	20	0.564	3	33%	100%	100%	Y
GMP2	30	0.582	5	80%	80%	100%	Y

Contact-percentages represent the number of times contact was made for an electrode modification size and type out of the total number of those electrodes tested. (RED: no contact made at any point; GREEN: definite contact made; OTHERS: contact sometimes made, inconsistent between various tests).

No connection to any AM or AMP1 electrode was made under any amount of applied pressure, which conforms to the hypothesis of this work. There was a fairly clear tendency for ohmic contact to occur with shallowest interfaces under the least amount of applied pressure, which also conforms to the hypothesis of this work. GMP1 or GMP2 modified electrode's measured interface depth was shallower than any AMP1 or AMP2 deposits by a difference of roughly 1  $\mu\text{m}$ .

It was the thicker P2 deposits (AM and GM) that tended to have heterogeneous outgrowths or protrusions in highly localized regions of the electrode surface or around the edges of the VIA-well. A major concern with these outgrowths was that they could have caused false-positives regarding magnitude of deflection required for ohmic electrode contact to be made. The precise reason for these outgrowths is uncertain but one possibility is that they were enabled by the use of  $\text{LiClO}_4$  in the electrolyte solution and the small size of the perchlorate ion enabling increased mass transport during the electrodeposition procedures.

## **5.5 - MATHEMATICAL MODELING OF SYMMETRICAL DEFLECTION OF A STATIC DISC**

This section is concerned with predicting the possible deflection magnitudes expected from the P-C based devices with defined physical dimensions, such as electrode diameter, using an equation that uses the radius, thickness of a static disc and the discs material properties to calculate deflection magnitudes under uniform, symmetrical bending under pressure.

There has been a large amount of work put into investigating the bending of plates for the sake of civil and mechanical engineering projects. One such collection of theories on plates was published by Timoshenko and Woinowsky-Krieger in 1959<sup>136</sup>. However, the size-scales of the plate systems studied and theorized about by Timoshenko *et al.* are several orders of magnitude larger than that of a flexible  $\mu\text{ECoG}$  probe being investigated and so their complex mathematical theories were not selected and a simpler model was utilized instead.

The modeling equation was not expected to predict the real-world performance of flexible  $\mu\text{ECoG}$  neural probes accurately, but to explore the use of mathematical modeling as a tool in future probe design processes and perhaps demonstrate an investigative starting point for a given matrix material,

regarding the microelectrode VIA-well physical dimensions (depth and radius). Depending on the physical dimensions of the VIA-well and microelectrode interface depth, especially as the electrode diameters begin to reach below the size-range of a single nerve cell, the prospect of losing physical contact with the tissue it is meant to be monitoring becomes a very real possibility. When a probe is oriented face-down, above each cylindrical VIA-well opening there is an unsupported cylinder of ‘base’ material (Parylene-C) that is capable of deflecting symmetrically downwards to some extent due to gravity or externally applied pressure. Due to the complex microstructures of the brain and the large number of unknowns and assumptions being made, the equation selected to explore this deflection was not the most rigorous or complicated deflection, but serves only as a first approximation. Considering the circular shape of the electrodes and assuming that the electrodes are “simply supported” in the X-Y plane, the “static-disc symmetrical deflection equation,” **Equation 5.2**, shown below, was selected from Ashby’s *Material Selection in Mechanical Design - Appendix B.7*.<sup>137</sup>

$$\delta = \frac{3}{4}(1 - \nu^2) \frac{\Delta P \cdot R^4}{E \cdot t^3} \quad [5.2]$$

Where:  $\delta$  is deflection magnitude (in m) at the disc’s central point;  $\nu$  is the disc material’s Poisson’s ratio;  $\Delta P$  is the pressure differential (in Pa) being applied uniformly across the static disc;  $R$  is radius (in m) circular microelectrode VIA-well;  $E$  is the Young’s modulus (in Pa) of the disc material; and  $t$  is thickness (in m) of the disc being deflected. See Figure 57, below, for visual representations of the equations parameters.

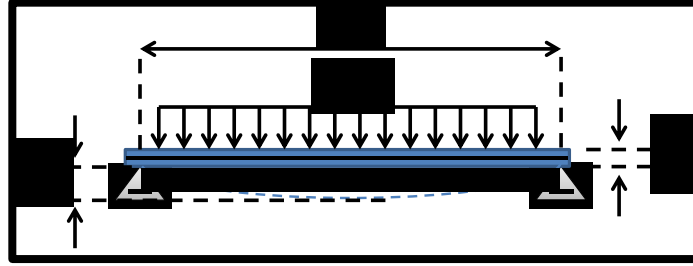


**Figure 55** – Schematic Model for the Static-Disk Symmetrical Deflection Equation.<sup>137</sup>

To allow for comparison between the experimental deflection testing results and the mathematical predictions of the model, **Equation 5.2** was rearranged to solve for the pressure required for a certain amount of deflection; expressed with **Equation 5.3**.

$$\Delta P = \frac{4 \cdot \delta (E \cdot t^3)}{3 (1 - \nu^2) R^4} \quad [5.3]$$

By predicting the pressure differential required to achieve a known magnitude of deflection, the experimental deflection pressures applied can be calculated and evaluated prior to testing for the applicability of flexible  $\mu$ ECoG probes in the end-user application that have been made with a certain material with known physical and mechanical properties.

### 5.5.1 METHODS: PHYSICAL MODELING PARAMETERS

The mechanical properties of polymers, such as P-C in this case, are quite uniform, predictable and easily obtainable from publications and supplier information sheets.<sup>138,139</sup> To develop the models into more meaningful and informative graphics, a selected range of VIA-well diameters and depths were used.

The physical modeling parameters used were chosen based on documented material properties,  $\mu$ ECoG device and electrode dimension and are listed below in Table 18.

**Table 18** – Physical Modeling Parameters for Parylene-C Thin-Film Devices

<b>Young's Modulus (GPa)</b>	2.8
<b>Poisson's Ratio</b>	0.4
<b>Base P-C Thickness Range (<math>\mu\text{m}</math>)</b>	2 – 25
<b>Max. VIA-Well Depth Range (<math>\mu\text{m}</math>)</b>	0.5 – 2
<b>VIA-Well Radii (<math>\mu\text{m}</math>)</b>	5, 10, 15, ... 195, 200
<b>Applied Pressures (kPa)</b>	125, 600, 1250, 2500, 5000

Unfortunately, due to the wide variety of neural tissues and the complex organization of the cells that compose them, the mechanical properties of nervous tissue need to be empirically studied *ad hoc*. Due to the interconnectivity between nerve cells and the anisotropic nature of the neuronal arrangement in the neo-cortex, I made the assumption that the neural surface is relatively flat and deflects a negligible amount into VIA-wells with diameters less than 50  $\mu\text{m}$ .

### 5.5.2 RESULTS AND DISCUSSION: MODELING PREDICTIONS

The first set of exploratory modeling results, shown on the next page in Figure 58, is the predicted deflection magnitudes achieved at pressure differentials of 125, 600, 1250, 2500 and 5000 kPa for base layer P-C thicknesses of 2 and 25  $\mu\text{m}$ .

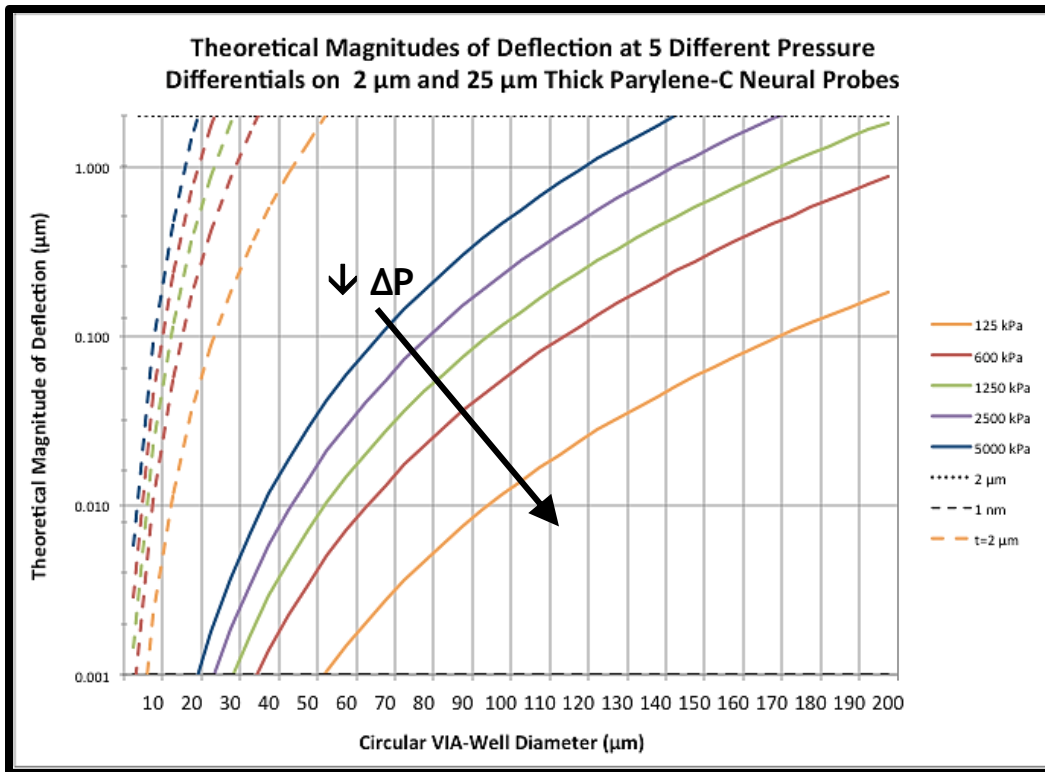


**Figure 56** – Magnitudes of deflection at various pressures for a 2  $\mu\text{m}$  (dashed lines) and a 25  $\mu\text{m}$  (solid lines) thick P-C base layer.

From this figure, it appears that the given material properties and mathematical equation used to predict deflection has created a model in which, with 25  $\mu\text{m}$  base layer, 2  $\mu\text{m}$  of deflection is achievable at a VIA-well diameter of 140  $\mu\text{m}$  and the application of 5000 kPa of pressure. Even with a base layer thickness of 2  $\mu\text{m}$ , 125 kPa is the predicted pressure required for 50  $\mu\text{m}$  diameter VIA-wells. By increasing the pressure up to the completely unrealistic maximum value of 5000 kPa, 2 microns of deflection is achievable for VIA-wells with diameters as small as 20  $\mu\text{m}$ .

A secondary form of the model, based on **Equation 5.3** and shown in Figure 59 below, was created to estimate the pressure differential required to achieve the deflection necessary, assuming an insulating layer thickness (i.e. maximum VIA-well depth) of either 2 (solid lines) or 0.5  $\mu\text{m}$  (dashed lines) with base layer thicknesses of 2, 5, 10, 20 and 25  $\mu\text{m}$ .

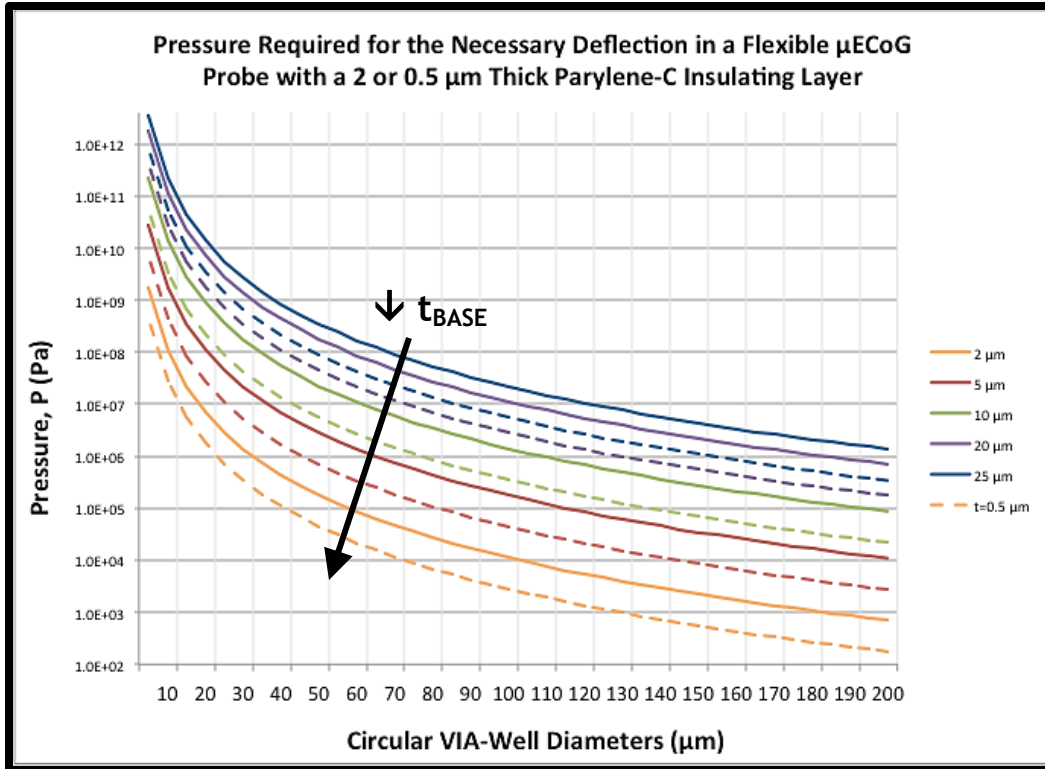


**Figure 57** – Estimated pressure required for the necessary deflection magnitude (solid = 2  $\mu\text{m}$ , dashed = 0.5  $\mu\text{m}$ ) for 2, 5, 10, 20, 25  $\mu\text{m}$  thick base layers of P-C  $\mu\text{ECoG}$  probes.

From the above figure, it is apparent that even with the thinnest device base layer (2  $\mu\text{m}$ ) with the minimum required magnitude of deflection (i.e. minimum VIA-well depth or insulating layer thickness), once VIA-well diameters were reduced below 20  $\mu\text{m}$  the required applied pressure differential enters the range of MPa ( $1 \times 10^6$  Pa). Probes with the thickest device base layer (25  $\mu\text{m}$ ) (similar those fabricated in this work) enter the MPa range of required applied pressures at VIA-well diameters around 200  $\mu\text{m}$ , with the required pressure getting more intense and unreasonable as VIA-well diameter is reduced.

### 5.5.3 MODEL PREDICTIONS VS. EXPERIMENTAL RESULTS

A comparison of the modeling of Equation 5.3, with the given physical parameters, to the experimental deflection under pressure test results theoretically provides some insight into the accuracy and therefore the

practical viability of **Equation 5.3** (which was derived from **Equation 5.2**) as a predictive modeling equation.

The minimum required applied pressure in the deflection tests to obtain contact at a VIA-well diameter of 30  $\mu\text{m}$  (GMP2 electrodes with an approximate interface depth of 0.5  $\mu\text{m}$ ) was 125 kPa and at 20  $\mu\text{m}$  (GMP1 electrodes with an approximate interface depth of 0.8  $\mu\text{m}$ ) was 1250 kPa. The VIA-well diameters and pressures required were turned into coordinate pairs: (20  $\mu\text{m}$ , 1250 kPa), (30  $\mu\text{m}$ , 125 kPa), and marked by an 'X' on the previous Figure 59 (the model based on Eq. 5.3) in Figure 60, next page.

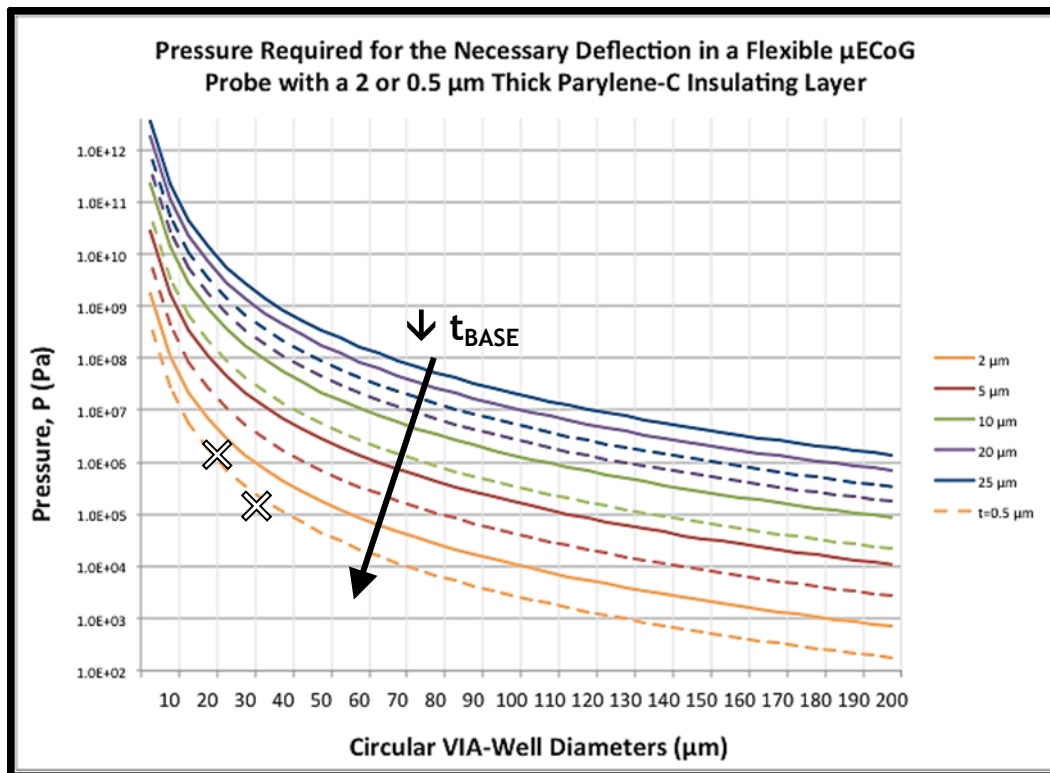


**Figure 58** – Predicted pressure required for the deflection model compared to the experimental results of the deflection test: (20  $\mu\text{m}$ , 1250 kPa), (30  $\mu\text{m}$ , 125 kPa) – marked with X's.

The marked coordinates, based on the minimum pressures required experimentally to deflect the GMP2 electrodes, which into electrical contact correlate fairly closely with the orange dashed-curve within Figure 60, represented a device with a 2  $\mu\text{m}$  base layer and an electrode interface depth

of 0.5  $\mu\text{m}$ . While this correlation is somewhat promising for the viability of the Eq. 5.3 as a predictive model, unfortunately the base layer thicknesses and electrode interface depths of the actual  $\mu\text{ECoG}$  devices that were tested are much more similar in dimension to the theoretical devices represented by the blue dashed curve in Figure 60, with a base layer thickness of 25  $\mu\text{m}$ . Ultimately, the accuracy of this modeling equation in predicting the required applied pressure to make ohmic electrode contact is around 4 orders of magnitude off. However, the trend demonstrated by the correlation of the two data points provides a small amount of credibility to the use of mathematical models, possibly enough to merit the consideration of a similar model for future flexible  $\mu\text{ECoG}$  probe designs.

## **5.6 - SUMMARY OF WORK**

In Chapter 5 I focused on exploring the physical surface of the modified and as-made  $\mu\text{ECoG}$  microelectrodes to obtain characterizations of the dimensions. Once average dimensions were obtained using AFM and associated software, estimates for layer thickness were made so that adhesion tests could be carried out and pressure driven deflection testing was executed. Finally, a mathematical equation used two ways to model the P-C probe behaviour based on a set of physical parameters. To qualify the accuracy of the equation being used, a comparison between the results of the deflection test and the mathematical models was performed.

### **5.6.1 DEPTH MEASUREMENT METHODS USING AFM SOFTWARE:**

There was often some user difficulty in correcting for planar bending in the data obtained during the AFM scan during pre-processing and it was found that these corrections (or miss-corrections) could seriously affect the final outcomes of the measured interface depths. In an attempt to obtain accurate values, the data was processed two times with differing methods: cross-sectional

profiles and pixel-population depth histograms. Cross-sectional profiles were taken for all electrode sizes and modification types and showed similar interface depths for both the 20 and 30  $\mu\text{m}$  diameter electrodes with the same type of electrode modification. Histograms of the AFM scan's pixel population were also used to obtain interface depths for all electrode sizes and types and there was typically good congruency between the smaller and larger electrodes of the same modification type. While this technique can be very effective with highly contrasted and homogeneous z-axis values, the width, height and any skewing of the population that occurs with non-planar surfaces can make this method rather difficult to interpret and cause the resulting measurements to become ambiguous.

The resulting measurements were then compared between the two methods by electrode size and modification type. When noticeable discrepancies arose between the results it was found that re-processing the original data in a more raw or less pre-processed state often helped correct for this discrepancy between methods. Reducing the amount of pre-processing (such as bend removal or planarization) also prevented the homogenization of pixel population that made the histogram method's measurements clearer and unambiguous; this was especially an issue with the GMP2 modification due to its relative closeness in interface depth and non-uniform deposition height.

### 5.6.2 LAYER THICKNESS AND ADHESION:

The approximate layer thickness of each modification was calculated by using the average depth measurements obtained by both AFM depth measurement methods taken before and after the electrodeposition procedures carried out in Chapter 4. P1 modification layer thicknesses on AM electrodes were found to be  $0.07 \pm 0.04 \mu\text{m}$  and  $0.08 \pm 0.02 \mu\text{m}$  for the 20 and 30  $\mu\text{m}$  diameter electrodes, respectively. The thicker P2 modification layer thicknesses on AM electrodes were found to be  $0.32 \pm 0.03 \mu\text{m}$  and  $0.37 \pm 0.05 \mu\text{m}$  for the 20 and 30  $\mu\text{m}$  diameter electrodes, respectively.

As for the surface-roughened GM electrodes, P1 layer thicknesses were found to be  $0.01 \pm 0.02 \mu\text{m}$  and  $0.03 \pm 0.02 \mu\text{m}$  for the 20 and 30  $\mu\text{m}$  diameter electrodes, respectively. P2 thicknesses were found to be  $0.21 \pm 0.02 \mu\text{m}$  and  $0.23 \pm 0.02 \mu\text{m}$  for the 20 and 30  $\mu\text{m}$  diameter electrodes, respectively. With average thicknesses of roughly 25 nm and 220 nm, both these layer thicknesses were over 80% less thick than had been predicted previously. Unexpectedly, the AM PEDOT layers are 3 and 1.5 times thicker than the GM PEDOT layers measured on 20  $\mu\text{m}$  and 30  $\mu\text{m}$  electrodes, respectively.

### 5.6.3 DEFLECTION TESTING AND MATHEMATICAL MODELING:

Results are congruent with expectations; however the amount of pressure being applied is completely unreasonable from a clinical application point-of-view. From a clinical perspective, practically any intentional pressure being applied externally to an ECoG probe during a craniotomy is beyond reasonable. The pressure applied throughout these experiments was to demonstrate that deflection can occur, outside of the brain, in a dry environment by the closing of the circuit at the electrode as indicated by the sudden passage of current through the probe as previously described. The presence of PEDOT outgrowths is a concern due to the creation of an electrical connection at the VIA-well edge without the expected deflection occurring.

The mathematical modeling of the deflection of flexible P-C  $\mu$ ECoG probes was moderately successful, keeping in mind the simplicity with which it operates. The predicted pressure required to deflect fully is entirely prohibitive and the predicted deflection resulting from the application of unreasonable amounts of pressure indicates that the deflection is severely limited and far from what is needed. The trends of the curves in the models demonstrate that the trend of reduction in size will create problems with deflection magnitude. By comparing the model results to the successful experimental deflection test results, it seems that the curves are following the right trend, but several orders of magnitude less pressure was required to apparently deflect into contact based on the comparison.

The core point of all those tests being that, while the application of pressure theoretically (and in alternate situations) can enable contact between micro-electrodes with relatively deep VIA-wells, the presence of sufficient additional electrode material (e.g. PEDOT) should eventually reduce the pressure required to a negligible amount that enables easy and constant makes contact with the neural tissue of the neo-cortex.

---

**CHAPTER 6 - SUMMARY OF**  
**EXPERIMENTAL RESULTS, CONCLUSIONS**  
**AND SUGGESTIONS FOR FUTURE WORK**

---

## **6.1 - RESTATEMENT OF THESIS**

A fundamental difference has become apparent in the micro-scale probes of today when compared to the mm-scale probes of the previous few decades due to the shift in fabrication methods and the reduced size-scale of new thin-film neural probes.<sup>25</sup> Tissue-electrode contact is critical for obtaining the best signal-to-noise ratio (SNR) and therefore the best quality (or most accurate) signal. As the microelectrode diameters are reduced while the supporting/insulating thin-film material is limited to a minimum required layer thickness, the electrode-diameter/VIA-well-depth aspect ratio will eventually inhibit or prevent tissue-electrode contact from being made.

Since we are measuring and investigating an unknown biological system that works in a very different way than computer technology and we understand very little about it the data quality is the most essential requirement for effective, meaningful analysis. The main concern with these size reductions is that the fidelity of the neuronal signal, or quality of the recorded signal, would suffer from the performance-limiting dimensions of the probes themselves reducing signal-quality, introducing signal artefacts and making all following analysis and interpretation more difficult, if not losing all meaningfulness that a higher-quality recording would have contained.

I propose that a feasible solution to this problem is through post-fabrication electrochemical modification of  $\mu$ ECoG electrodes to fill-in the VIA-wells. A variety of electrode modifications with PEDOT and/or a rough-gold adhesion layer were used to investigate whether ohmic electrical contact was lost at microelectrode diameters of 20 and 30  $\mu$ m by providing various electrode interface depths for deflection testing. The bigger-picture objective was the maintenance of the signal-quality obtained using passive, flexible,  $\mu$ ECoG multi-electrode arrays (MEAs) as their disc-shaped electrodes are progressively reduced in diameter for enhanced spatial resolution of the device.

## 6.2 - EXPERIMENTAL RESULTS AND DISCUSSION

In this section the summarized results from Chapter's 3, 4 and 5 will be reviewed and discussed with respect to the objectives of the chapter, the overall experimental work and their significance within or contribution to the scientific community.

### 6.2.1 THIN-FILM $\mu$ ECOG PROBE SYSTEM DESIGN OBJECTIVES

The following reflections on the design objectives for the “front-end”  $\mu$ ECOG probe device from Chapter 3 and discussion as to whether I did or didn't meet the objectives set out for me.

#### 6.2.1.1 $\mu$ ECOG DESIGN OBJECTIVE SUMMARIES

- Matrix material selected was Parylene-C, meeting all criteria; although an increased base-layer thickness was used throughout the fabrication process for ease of handling during post-fabrication modifications and testing. The base-layer thickness of  $23.8 \pm 0.2 \mu\text{m}$  and  $1.97 \pm 0.04 \mu\text{m}$  thick insulating layer of P-C were used to support and insulate the circuitry, respectively.
- Electrochemically safe, inert metallic Au selected to serve as the base electrode material on top of a Ti adhesion layer (unexposed). Conductive
- Gold met these standards and was used for the metallic layer material with approximately 7.5 nm of Ti as an underlying adhesion layer the overall metal layer thickness was  $134 \pm 19 \text{ nm}$  that composed the insulated circuitry and as-made electrodes. Gold was also used in post-fabrication modifications as the electrodeposited adhesion layer.
- Further electrode modifications applied  $\text{PEDOT}^+|\text{ClO}_4^-$  as the final electrode-tissue interface material which also met the requirements of this objective.

- Electrode sizes and spacing's roughly match the size of (some) neurons and spacing of neurons in small or medium functional nuclei of interest.
- The electrodes were designed to match specific nuclei from neo-natal rat brain slices, specifically the *ventro-medial hypothalamus* (VMH) and the *locus coeruleus* (LC), however the effectiveness of these layouts remain unknown due to difficulty in effectively carrying out the electrophysiological recordings.
- Probe body long enough to allow for slack between probe head and probe tail.
- Designed to accommodate 5 probe devices per wafer with each probe reaching a length of 7 cm on a 10 cm Si wafer, the probes were adequately long for the post-fabrication handling and experimentation.
- Optimized microfabrication process flow maximizing batch yields of defect-free probes with good conductivity in the deposited metallic layer.
- After several iterations of the fabrication process and numerous adjustments to lithographic exposure and development times and PVD sputtering times for the metallic layer, in the final batch of wafers I obtained a yield of 94.4% successfully fabricated probe microelectrodes. (Refer back to Section 2.6.1 for the optimized process flow if needed.)
- Metallic circuitry layer resistivity was measured by 4PP and averaged between the batches to a value of  $12 \times 10^{-6} \Omega\text{-cm}$ .
- Compatible connection to the back-end connector device at the ZIF tail of the probe.
- The connection to the back-end ZIF connector device used available CAD drawings for the 18-channel ZIF-clip interface component that was selected as the connector. The back-end ZIF connector devices ZIF tails were thickened to 0.3 mm with Kapton® tape for secure pin-to-pad connections.

The following are my summarized results from the design and fabrication objectives set out in Chapter 3 for the “back-end” ZIF connector device and discussion as to whether the goals were met.

### 6.2.1.2 ZIF-CONNECTOR DESIGN OBJECTIVE SUMMARIES

- Manually connect to any neural probe microelectrode channel repeatedly and easily to external electronics (e.g. amplifiers, potentiostat, etc.).
- Easily connectable to the desired  $\mu$ ECoG electrode at the front end through the numbered back-end wiring that repeatedly allowed for connections to all the necessary electronic equipment via alligator clip without creating short-circuits.
- Negligible amount of resistance across the connector pathways.
- Resistance of each pathway from where the front end connects to the wiring measured at an average of  $0.32 \pm 0.08 \Omega$  within a range from  $0.21$  to  $0.42 \Omega$ . This was deemed negligible in comparison to the impedance found through EIS in following chapters.
- Probe-side clip-component that requires little-to-no insertion force but still enables a secure connection (non-destructively) with the thin, flexible matrix of the probe.
- A gold-plated, 18 channel ZIF-connector component was selected with mm-scale separations between the channels so that the connection was easily and repeatedly made to the Kapton® tape reinforced and adequately thickened back-end connection of the flexible  $\mu$ ECoG with no insertion force necessary.
- Support the clip-component and internal wiring with a Easily assembled or disassembled protective hard-shell case.
- By using 3D CAD and a 3D printer, a hard shell casing was specifically designed for this purpose and fabricated as two pieces that click together. The ZIF-component
- Comprised of three separate pieces, the casing was held together by physical clips that prevented the halves from sliding apart and then the two halves were taped together so that the case could be opened but would not open when it wasn't desired.
- Wires that can be manipulated/handled at the free end without breaking/compromising the circuit pathway.

## 6.2.2 ELECTROCHEMICAL MODIFICATION AND IN VITRO EIS OF $\mu$ ECOG MICROELECTRODES

The following are the various electrochemical modifications of the microelectrodes that I performed in Chapter 3 using a Gamry Reference 3000 and the visual inspections performed using optical microscopy with a Keyence VHX-2000 Digital Microscope.

### 6.2.2.1 ELECTROCHEMICAL MICROELECTRODE MODIFICATIONS

The electrochemical modifications of the flexible neural probe microelectrodes were performed in three-electrode cells within a FC under a blanket of N<sub>2</sub> gas at constant currents.

Resulting from these electrodeposition procedures were 6 variations of electrode modification to be inspected and tested at both the 20  $\mu$ m and the 30  $\mu$ m diameters:

- #1) as-made (AM) sputtered gold;
- #2) gold-modified with a rough gold adhesion layer (GM);
- #3) as-made with a thin layer of PEDOT (AMP1);
- #4) as-made with a thicker layer of PEDOT (AMP2);
- #5) gold modified adhesion layer with a thin layer of PEDOT (GMP1);
- #6) and gold modified adhesion layer with a thicker layer of PEDOT (GMP2).

The electrodes were cleaned thoroughly by submersion of the probe body in successive ultrasound baths of acetone, IPA and DI water and then blow dry with N<sub>2</sub> gas. Following this, all 12 possible variations of the cleaned and dried electrodes were visually inspected by optical microscopy.

### 6.2.2.2 VISUAL INSPECTION OF ELECTRODEPOSITED LAYERS

Microscope images of the various electrodes were taken digitally using a Keyence VHX-2000 Digital Microscope in “depth composition” mode. Shown below in Figures 61, 62 and 63 are the resulting images of the 20  $\mu\text{m}$  and 30  $\mu\text{m}$  diameter electrodes at 1500x magnification, paired by modification type (AM on the left, GM on the right) with PEDOT layer thickness increasing

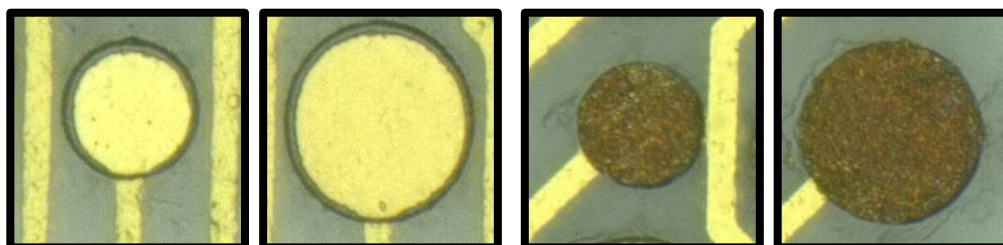


**Figure 59** – Outer Left (OL): 20  $\mu\text{m}$  AM, Inner Left (IL): 30  $\mu\text{m}$  AM;  
Inner Right (IR): 20  $\mu\text{m}$  GM, Outer Right (OR): 30  $\mu\text{m}$  GM.

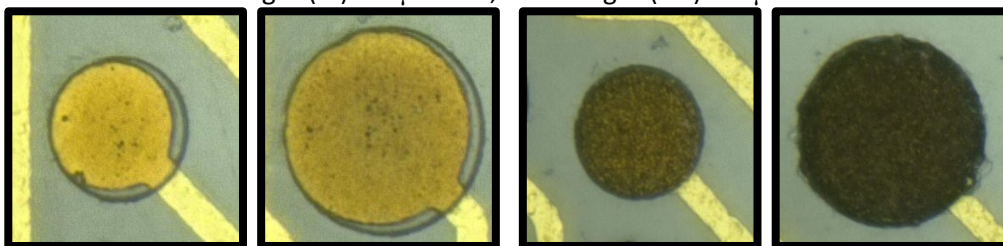


**Figure 60** – OL: 20  $\mu\text{m}$  AMP1, IL: 30  $\mu\text{m}$  AMP1; IR: 20  $\mu\text{m}$  GMP1, OR: 30  $\mu\text{m}$  GMP1.

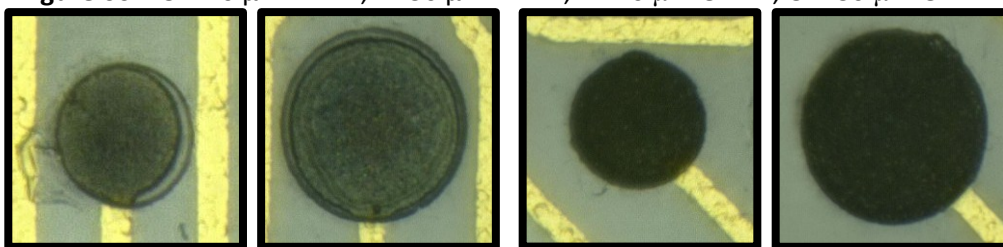


**Figure 61** – OL: 20  $\mu\text{m}$  AMP2, IL: 30  $\mu\text{m}$  AMP2; IR: 20  $\mu\text{m}$  GMP2, OR: 30  $\mu\text{m}$  GMP2.

As discussed previously in Section 4.9, the AM and GM electrodes have distinctly visible differences in surface morphology. AM layers are pocked but relatively flat and specular; GM layers are non-specular, rough surfaces with numerous small grains of gold nucleated across its surface. It appears that these morphological differences impacted the deposition of PEDOT that followed, with each metallic base layer type exhibiting similar deposition

mechanics between both of the thicknesses of PEDOT applied but being different between the two conditions of gold.

The apparent flatness and featureless-ness of the AM layer enabled somewhat uniform deposition thickness, but polymerization was preferred at surface defects or imperfections as indicated by the presence of PEDOT clusters. On the AM variant, it is also shown that the thickness of PEDOT impacts the resulting colour of the layer due to the quantity deposited and the anisotropic nature of PEDOT molecules (AMP1: brown; AMP2: greenish-blue).

On the GM variant, PEDOT deposition occurred more randomly across the surface, growing most quickly at the peaks of the grains of gold and imparting a rougher, more fibrous looking PEDOT layer. GMP1 layers appear thinly spread in a translucent dark blue layer and GMP2 layers appear almost black from the thickness of the layer, it's roughness and the randomly oriented growth directions of the PEDOT molecules resulting from the initial GM state. Increased roughness of the GM PEDOT layers is also supported by inspection by AFM, but the difference in ESA obtained was found to be similar for each PEDOT layer during EIS testing.

### 6.2.2.3 IN VITRO ELECTROCHEMICAL IMPEDANCE SPECTROSCOPY (EIS) TESTING

EIS testing was performed in vitro in 1 M PBS solution. The electrode-electrolyte interface impedances of the various modified and unmodified electrode were performance tested by EIS ( $10^{-1}$  to  $10^5$  Hz, 10 mV<sub>RMS</sub> AC, 5 mV steps) within a three-electrode cell using the pseudo-biological medium of 1 M PBS as the test electrolyte an Ag|AgCl RE and a Pt wire CE. Based on the results of the EIS testing performed:

- AM electrodes had the highest impedance values relative to otherwise modified electrodes. This is due to the AM electrode type having the lowest ESA.

- Slightly lower impedance across all frequencies with any GM type of electrode compared to similar AM electrodes.
- Expected that 20  $\mu\text{m}$  electrodes would always have higher impedance than 30  $\mu\text{m}$  electrodes of the same type. However, the 30  $\mu\text{m}$  AM electrode performed worse at 0.1 Hz and 1 Hz than the 20  $\mu\text{m}$  AM electrodes. Otherwise, the AM electrode impedance is higher in the case of 20  $\mu\text{m}$  electrodes at frequencies greater than 1 Hz, as expected.
- Quantity of PEDOT deposited most greatly impacted the reduction of impedance, regardless of a GM adhesion layer.
- GMP2 goes from a phase angle of nearly  $-90^\circ$  at 0.1 Hz (indicating purely capacitive charge transfer), to  $-10^\circ$  at 100 kHz (where  $0^\circ$  is indicative of ohmic charge transfer).

### 6.2.3 PHYSICAL CHARACTERIZATION OF MICROELECTRODE INTERFACES, MATHEMATICAL DEFLECTION MODELING AND PRESSURE-BASED PROBE DEFLECTION TESTING

In the following section the results of the physical characterization of the modified and unmodified electrodes performed via AFM are summarized along with the results from the subsequent pressure-based deflection testing and discussion of the accuracy of the simple mathematical model.

#### 6.2.3.1 PHYSICAL CHARACTERIZATION OF MICROELECTRODE INTERFACES: PEDOT LAYER THICKNESS

The approximate thickness of each modification was calculated by using the average depth measurements obtained by both AFM depth measurement methods taken before and after the electrodeposition procedures carried out in Chapter 4. The GM layers were the thickest modification ( $0.98 \pm 0.08 \mu\text{m}$ ), the P1 layers were the thinnest ( $75 \pm 30 \text{ nm}$  on AM;  $25 \pm 20 \text{ nm}$  on GM) and the P2 layers ( $350 \pm 40 \text{ nm}$  on AM;  $220 \pm 20 \text{ nm}$  on GM) were thicker than P1 but

thinner than GM, as desired. While these thickness were acceptable, no PEDOT layer that was deposited ever grew to the intended thickness, either on AM or GM electrodes.

At average thicknesses of roughly 75 nm and 350 nm (20  $\mu\text{m}$  and 30  $\mu\text{m}$ , respectively,) depositions onto AM electrodes achieved thicknesses 50% of the expected thicknesses. With average thicknesses of roughly 25 nm and 220 nm, both these GM-based PEDOT layer thicknesses were over 80% less thick than had been predicted previously. Unexpectedly, the AM PEDOT layers are 3 and 1.5 times thicker than the GM PEDOT layers measured on 20  $\mu\text{m}$  and 30  $\mu\text{m}$  electrodes, respectively.

#### 6.2.3.2 PHYSICAL CHARACTERIZATION OF MICROELECTRODE INTERFACES: PEDOT LAYER ADHESION

The evidence suggests that the GM is improving adhesion and demonstrated that the thicker PEDOT layers (P2) adhered most poorly to the as-made (AM) gold electrode surfaces. However with the small sample population that was tested no valuable conclusions can be made.

#### 6.2.3.2 MATHEMATICAL PROBE DEFLECTION MODELING

The mathematical modeling of the deflection of flexible P-C  $\mu\text{ECoG}$  probes was moderately successful, keeping in mind the simplicity with which it operates. The predicted pressure required to deflect fully is largely prohibitive and the predicted deflection resulting from the application of reasonable amounts of pressure indicates that the deflection is severely limited and far from what is needed. The trends of the curves in the models demonstrate that the trend of reduction in size will create problems with deflection magnitude. By comparing the model results to the successful experimental deflection test results, it seems that the curves are following the right trend, but several

orders of magnitude less pressure was required to apparently deflect into contact based on the comparison.

### 6.2.3.3 PROBE DEFLECTION TESTS UNDER PRESSURE

Results were congruent with the hypothesis in that the largest-diameter electrodes/VIA-wells with the shallowest electrode interfaces were most easily and consistently put into direct, ohmic contact and *vice versa*: the smaller electrodes (20  $\mu\text{m}$ ) with less modified and therefore deeper electrode interfaces were the most difficult and least able to be put into direct electrode contact. However, the amounts of pressure being applied to enable the direct contact between most of the electrode modification types and sizes were unreasonable from a clinical application point-of-view. The presence of outgrowths is a concern due to the forming of an electrical connection without the expected deflection occurring.

## 6.3 - CONCLUSIONS AND SUGGESTIONS FOR FUTURE WORK

In this section several suggestions for improvements in device design, possible alternatives for fabrication methods, and experimental changes that could be made in future endeavours to enable more robust studies into the performance limitations of thin-film  $\mu\text{ECOG}$  probes devices created by the insulating material layer's VIA-well dimensions and electrode interface depths therein.

### 6.3.1 DESIGN IMPROVEMENTS

The designing process is rather iterative and many things can be changed in the design to rectify any unwanted performance issues or to target larger or smaller areas with more electrodes.

Increasing the range of electrode diameters per device would also provide additional insight into the dimensional impact of VIA-well depth as a function of decreasing electrode size.

### 6.3.2 FABRICATION CHANGES

Unlike the computer industry, there are size and spacing minimums that match to the size and spacing of the neurons and neuronal networks. As such, there may be the opportunity to use other fabrication technologies such as 2-D or 3-D printed circuits as these technologies are advanced.

With more advanced technology such as electron-beam lithography, single-digit nanometer-scale features can be fabricated, although great skill is required to do so consistently with either technology.

### 6.3.3 ELECTROCHEMICAL MODIFICATION AND CHARACTERIZATION

Experiment with potentiodynamic PEDOT deposition methods (cyclic and/or pulsed voltammetry) for more uniform film thicknesses.<sup>140</sup> The addition of surfactants of some type to the electrolyte solutions could also be an effective solution to obtain more uniformity in the thickness of the deposited layers.

### 6.3.4 DEFLECTION MODELING AND TESTS

Use a more controlled, sensitive setup with more variety in electrode diameter and interface depths as well as the combined electrochemical/mechanical testing.

It would be interesting to combine the deflection testing with a non-submersion EIS test by using a hydrogel electrolyte that approximates the mechanical properties of the neo-cortical surface. In this way, with the additional range of electrode/VIA-well dimensions previously mentioned, a more robust and true-

to-life *in vitro* study of the impact that dimensions have on the quality of neuronal signals recorded *in vivo* could be performed.

### 6.3.5 ADHESION/DELAMINATION TESTS

An increased number of repetitions of the exact same experimental procedure detailed in this work would provide more certainty and merit to the results obtained in this work; however, the same procedure performed across a greater range of electrode sizes and a wider range of more controlled, uniform modification layers and interface depths would more significantly improve the value of this type of study, assuming that a large enough population was tested.

In addition to the expanded range of dimensions being tested, a more repeatable, controlled experimental test, similar in many ways to the improvements to deflection testing, would greatly increase the value of the data being collected.

### 6.3.6 TESTS WITHIN AN ANIMAL MODEL

It would be ideal to have an opportunity to test the probe *in vivo* with an animal model (e.g. adult rat) to obtain useful data regarding the impact of the electrode modifications and resulting interface depth on the sub-dural surface of the mammalian cerebral cortex to better understand the change in efficacy of the microelectrodes in a BCI type application.

## 6.4 - CLOSING REMARKS

In conclusion, although the dataset populations and variations in electrode/VIA-well geometries were not sufficient to make any strong claims, the results from this thesis work seem to suggest that VIA-well depth at small enough electrode diameters can prevent electrode contact from being made, even at levels of applied pressure that exceed what would be reasonably applicable to the human brain, but by the addition of electrodeposited materials, (effectively increasing the electrode thickness and reducing the interface depth,) successful electrode contact can be made with the application of small amounts of pressure, and, perhaps, with further reduction of interface depth no additional pressure at all could be required to make strong tissue-electrode contact with the neo-cortical surface.

The amount of pressure required to initiate contact between dry electrodes was reduced as the electrode thickness was increased, with the reduction of interface depth, indicating that there is an improved rate of successful electrode contact with increased quantities of electrodeposited materials onto the as made electrodes. The use of a rudimentary symmetrical static disc bending equation has also demonstrated that numerical models of these trends were loosely followed, although the magnitudes of pressure differ significantly from the values found to be experimentally required.

Results also indicated a trend of delamination of thick PEDOT layers from unmodified, as-made electrodes while the use of an underlying adhesion layer seems to have allowed for PEDOT layers of the same thickness to resist delamination, as expected from previous studies, although these experiments lack the thoroughness to be truly confident in the claim that they are necessary at all electrode diameters.

This work has taken the first step into exploring a performance limitation that would otherwise remain invisible due to the ionic conduction of current *in vivo*

or *in vitro*. While more repetitions are required to demonstrate this clearly and without any doubt, the initial data indicates that further investigation would be worthwhile and that there is a good chance that other state-of-the-art  $\mu$ ECOG fabricators would benefit from the use of electrochemical methods to raise the interface of their microelectrodes in order to obtain the highest-fidelity signalling data possible, which would no doubt assist in both BCI applications and the neurophysiological analysis of brain signals in the cerebral cortex.

## REFERENCES

1. Nicholls, J. G., Wallace, B. G., Martin, A. R. & Fuchs, P. A. *From Neuron to Brain*. (Sinauer Associates, Inc., 2001).
2. *The human nervous system: structure and function*. (Humana Press, 2005).
3. Nowinski, W. L. Ch. 2 - Introduction to Brain Anatomy. in *Biomechanics of the Brain* 5-40 (Springer Science & Business Media, 2011).
4. Alivisatos, a. P. *et al.* Nanotools for neuroscience and brain activity mapping. *ACS Nano* **7**, 1850-1866 (2013).
5. Bainbridge, W. S. *Converging technologies for improving human performance: Nanotechnology, biotechnology, information technology and cognitive science*. (Springer Science & Business Media, 2013).
6. *Implantable Neural Prostheses 1*. (Springer US, 2009). doi:10.1007/978-0-387-77261-5
7. *Implantable neural prostheses 2: techniques and engineering approaches*. (Springer, 2010).
8. Baker, M. From promising to practical: tools to study networks of neurons. *Nat. Methods* **7**, 877 (2010).
9. Sreedharan, S., Sitaram, R., Paul, J. S. & Kesavadas, C. Brain-computer interfaces for neurorehabilitation. *Crit. Rev. Biomed. Eng.* **41**, (2013).
10. Cheung, K. C. Thin-Film Microelectrode Arrays for Biomedical Applications. in *Implantable Neural Prostheses 2* (eds. Zhou, D. D. & Greenbaum, E.) 157-190 (Springer Science & Business Media, 2010).

11. Demetriades, A. K., Demetriades, C. K., Watts, C. & Ashkan, K. Brain-machine interface: The challenge of neuroethics. *The Surgeon* **8**, 267-269 (2010).
12. Ramey, C. H. Neuroethics: Challenges for the 21st century. *Philos. Psychol.* **23**, 125-129 (2010).
13. Glannon, W. Neuroethics. *Bioethics* **20**, 37-52 (2006).
14. *Artificial sight: basic research, biomedical engineering, and clinical advances.* (Springer, 2007).
15. *Guide to Brain-Computer Music Interfacing.* (Springer London, 2014). doi:10.1007/978-1-4471-6584-2
16. Kotchetkov, I. S., Hwang, B. Y., Appelboom, G., Kellner, C. P. & Connolly Jr, E. S. Brain-computer interfaces: military, neurosurgical, and ethical perspective. *Neurosurg. Focus* **28**, E25 (2010).
17. Cogan, S. F. Neural stimulation and recording electrodes. *Annu. Rev. Biomed. Eng.* **10**, 275-309 (2008).
18. Escabí, M. A. *et al.* A high-density , high-channel count , multiplexed  $\mu$  ECoG array for auditory-cortex recordings. 1566-1583 (2014). doi:10.1152/jn.00179.2013
19. Ledochowitstch, P. (Berkeley), Felus, R. J. (INP-P., Miyakawa, A. (Berkeley) & Maharbiz, M. M. (Berkeley). FABRICATION AND TESTING OF A LARGE AREA , HIGH DENSITY , PARYLENE MEMS  $\mu$  ECOG ARRAY. *IEEE 24th Int. Conf. Micro Electro Mech. Syst.* 1031-1034 (2011).
20. Cheung, K. C. Thin-film Microelectrode Arrays for Biomedical Applications. in *Implantable Neuroprostheses 2* (eds. Zhou, D. D. & Greenbaum, E.) 157-190 (Springer Science, 2010).

21. Harris, A. R. *et al.* Conducting polymer coated neural recording electrodes. *J. Neural Eng.* **10**, 016004 (2013).
22. Schendel, A. a., Eliceiri, K. W. & Williams, J. C. Advanced materials for neural surface electrodes. *Curr. Opin. Solid State Mater. Sci.* **18**, 301-307 (2014).
23. Buzsáki, G., Anastassiou, C. A. & Koch, C. The origin of extracellular fields and currents – EEG, ECoG, LFP and spikes. *Nat. Rev. Neurosci.* **13**, 407-420 (2012).
24. Stacey, W. C., Kellis, S., Patel, P. R., Greger, B. & Butson, C. R. Signal distortion from microelectrodes in clinical EEG acquisition systems. *J. Neural Eng.* **9**, 056007 (2012).
25. Leuthardt, E. C., Schalk, G., Roland, J., Rouse, A. & Moran, D. W. Evolution of brain-computer interfaces: going beyond classic motor physiology. *Neurosurg. Focus* **27**, E4 (2009).
26. Nieuwenhuys, R., Voogd, J. & Huijzen, C. van. *The human central nervous system.* (Springer, 2008).
27. Hendelman, W. J. *Atlas of Functional Neuroanatomy.* (CRC Press, 2006).
28. Liebenthal, E. Introduction to Brain Imaging. in *Biomechanics of the Brain* (ed. Miller, K.) 41-68 (Springer Science, 2011).
29. Lauterbur, P. C. The Classic: Image Formation by Induced Local Interactions: Examples Employing Nuclear Magnetic Resonance (1973). *Clin. Orthop.* **244**, 3-6 (1989).
30. Ogawa, S., Lee, T.-M., Kay, A. R. & Tank, D. W. Brain magnetic resonance imaging with contrast dependent on blood oxygenation. *Proc. Natl. Acad. Sci.* **87**, 9868-9872 (1990).

31. Kwong, K. K. *et al.* Dynamic magnetic resonance imaging of human brain activity during primary sensory stimulation. *Proc. Natl. Acad. Sci.* **89**, 5675-5679 (1992).
32. Leuthardt, E. C., Schalk, G., Wolpaw, J. R., Ojemann, J. G. & Moran, D. W. A brain-computer interface using electrocorticographic signals in humans. *J. Neural Eng.* **1**, 63-71 (2004).
33. Henle, C. *et al.* First long term in vivo study on subdurally implanted Micro-ECoG electrodes, manufactured with a novel laser technology. *Biomed. Microdevices* **13**, 59-68 (2011).
34. Buzsáki, G. Neural Syntax: Cell Assemblies, Synapsembles, and Readers. *Neuron* **68**, 362-385 (2010).
35. Tudor, M., Tudor, L. & Tudor, K. I. [Hans Berger (1873-1941)--the history of electroencephalography]. *Acta Medica Croat. Cas. Hravatske Akad. Med. Znan.* **59**, 307-313 (2005).
36. *Niedermeyer's Electroencephalography: Basic Principles, Clinical Applications, and Related Fields.* (Wolters Kluwer, 2010).
37. Bazhenov, M. & Makeig, S. Ch. 8 - Multiscale Electroencephalographic Dynamics and Brain Function. in *Principles of Brain Dynamics* 165-181 (MIT Press, 2012).
38. Frank, M. G. Brain Rhythms. *Encyclopedia of Neuroscience* 482-483 (2009).
39. Buzsáki, G. Neural Syntax: Cell Assemblies, Synapsembles, and Readers. *Neuron* **68**, 362-385 (2010).
40. Collingridge, G. L. The brain slice preparation: a tribute to the pioneer Henry McIlwain.pdf. *J. Neurosci. Methods* 5-9 (1995).

41. Kantor, C. *et al.* Ch. 11 - Spontaneous Neural Network Oscillations in Hippocampus, Cortex, and Locus Coeruleus of Newborn Rat and Piglet Brain Slices. in *Isolated Central Nervous System Circuits* (ed. Ballanyi, K.) **73**, 315-356 (Humana Press, 2012).
42. Windhorst, U., Lalley, P. M. & Binder, M. D. Action Potential. in *Encyclopedia of Neuroscience* 22-29 (Springer, 2009).
43. Haider, B. & McCormick, D. A. Rapid Neocortical Dynamics: Cellular and Network Mechanisms. *Neuron* **62**, 171-189 (2009).
44. Kruskal, P. B., Jiang, Z., Gao, T. & Lieber, C. M. Beyond the Patch Clamp: Nanotechnologies for Intracellular Recording. *Neuron* **86**, 21-24 (2015).
45. Berdondini, L. *et al.* Active pixel sensor array for high spatio-temporal resolution electrophysiological recordings from single cell to large scale neuronal networks. *Lab. Chip* **9**, 2644 (2009).
46. Song, Y. *et al.* A novel dual mode microelectrode array for neuroelectrical and neurochemical recording in vitro. *Biosens. Bioelectron.* **38**, 416-420 (2012).
47. Kubler, A., Nijboer, F. & Birbaumer, N. Ch. 22 - State of the Art in Clinical Applications of BCIs. in *Towards Brain-Computer Interfacing* 373-391 (MIT Press, 2007).
48. Do, A. H. *et al.* Sensitivity and specificity of upper extremity movements decoded from ECoG. in *EMBS* 5618-5621 (IEEE, 2013).
49. Jadhav, A. D., Aimo, I., Cohen, D., Ledochowitsch, P. & Maharbiz, M. M. Cyborg eyes: microfabricated neural interfaces implanted during the development of insect sensory organs produce stable neurorecordings in the adult. in *Micro Electro Mechanical Systems (MEMS), 2012 IEEE 25th International Conference on* 937-940 (IEEE, 2012).

50. Polikov, V. S., Tresco, P. A. & Reichert, W. M. Response of brain tissue to chronically implanted neural electrodes. *J. Neurosci. Methods* **148**, 1-18 (2005).
51. Ward, M. P., Rajdev, P., Ellison, C. & Irazoqui, P. P. Toward a comparison of microelectrodes for acute and chronic recordings. *Brain Res.* **1282**, 183-200 (2009).
52. Lusted, H. S. In Vivo Electrical Stimulation Using Multichannel Photolithographic Electrode Arrays. *IEEE Trans. Biomed. Eng.* 800-803 (1986).
53. Campbell, P. K., Jones, K. E., Huber, R. J., Horch, K. W. & Normann, R. A. A silicon-based, three-dimensional neural interface: manufacturing processes for an intracortical electrode array. *IEEE Trans. Biomed. Eng.* **38**, 758-768 (1991).
54. Leuthardt, E. C. What's holding us back? Understanding barriers to innovation in academic neurosurgery. *Surg. Neurol.* **66**, 347-349 (2006).
55. Leuthardt, E. C., Freudenberg, Z., Bundy, D. & Roland, J. Microscale recording from human motor cortex - implications for minimally invasive ECoG brain-computer interfaces. *Neurosurg. Focus* **27**, 1-8 (2009).
56. Kubánek, J., Miller, K. J., Ojemann, J. G., Wolpaw, J. R. & Schalk, G. Decoding flexion of individual fingers using electrocorticographic signals in humans. *J. Neural Eng.* **6**, 066001 (2009).
57. Ulbert, I., Halgren, E., Heit, G. & Karmos, G. Multiple microelectrode-recording system for human intracortical applications. *J. Neurosci. Methods* **106**, 69-79 (2001).

58. Jones, R. S. G., da Silva, A. B., Whittaker, R. G., Woodhall, G. L. & Cunningham, M. O. Human brain slices for epilepsy research: Pitfalls, solutions and future challenges. *J. Neurosci. Methods* **260**, 221-232 (2016).
59. Vallejo-Giraldo, C., Kelly, A. & Biggs, M. J. P. Biofunctionalisation of electrically conducting polymers. *Drug Discov. Today* **19**, 88-94 (2014).
60. Massia, S. P., Holecko, M. M. & Ehteshami, G. R. In vitro assessment of bioactive coatings for neural implant applications. *Bioact. Coat. Neural Implants* 177-186 (2003).
61. Yoshida Kozai, T. D. *et al.* Ultrasmall implantable composite microelectrodes with bioactive surfaces for chronic neural interfaces. *Nat. Mater.* **11**, 1065-1073 (2012).
62. Justin, G., Finley, S., Abdur Rahman, A. R. & Guiseppi-Elie, A. Biomimetic hydrogels for biosensor implant biocompatibility: electrochemical characterization using micro-disc electrode arrays (MDEAs). *Biomed. Microdevices* **11**, 103-115 (2009).
63. Sridharan, A., Rajan, S. D. & Muthuswamy, J. Long-term changes in the material properties of brain tissue at the implant-tissue interface. *J. Neural Eng.* **10**, 066001 (2013).
64. Schalk, G. & Leuthardt, E. C. Brain-Computer Interfaces Using Electrocorticographic Signals. *IEEE Rev. Biomed. Eng.* **4**, 140-154 (2011).
65. Schendel, A. A. *et al.* The effect of micro-ECOG substrate footprint on the meningeal tissue response. *J. Neural Eng.* **11**, 046011 (2014).
66. Prohaska, O. J., Olcaytug, F., Pfundner, P. & Dragaun, H. thin-film multiple electrode probes- possibilities and limitations. *IEEE Trans. Biomed. Eng.* **BME-33**, 223-229 (1986).

67. Khodagholy, D. *et al.* NeuroGrid: recording action potentials from the surface of the brain. *Nat. Neurosci.* **18**, 310-315 (2014).
68. Viventi, J. *et al.* Flexible, foldable, actively multiplexed, high-density electrode array for mapping brain activity in vivo. *Nat. Neurosci.* **14**, 1599-1605 (2011).
69. Takaura, K., Tsuchiya, N. & Fujii, N. Frequency-dependent spatiotemporal profiles of visual responses recorded with subdural ECoG electrodes in awake monkeys: Differences between high- and low-frequency activity. *NeuroImage* **124**, 557-572 (2016).
70. Khodagholy, D. *et al.* In vivo recordings of brain activity using organic transistors. *Nat. Commun.* **4**, 1575 (2013).
71. Smith, S. W. *The Scientist and Engineer's Guide to Digital Signal Processing*. (California Technical Publishing, 1999).
72. Santos, R. M., Laranjinha, J., Barbosa, R. M. & Sirota, A. Simultaneous measurement of cholinergic tone and neuronal network dynamics in vivo in the rat brain using a novel choline oxidase based electrochemical biosensor. *Biosens. Bioelectron.* **69**, 83-94 (2015).
73. Fröhlich, F. & McCormick, D. A. Endogenous Electric Fields May Guide Neocortical Network Activity. *Neuron* **67**, 129-143 (2010).
74. Robblee, L. S. & Rose, T. L. Electrochemical Guidelines for Selection of Protocols and Electrode Materials for Neural Stimulation. in 26-66 (1989).
75. Brummer, S. B., Robblee, L. S. & Hambrecht, F. T. Criteria for selecting electrodes for electrical stimulation: theoretical and practical considerations. *Ann. N. Y. Acad. Sci.* **405**, 159-171 (1983).

76. Robblee, L. S., Lefko, J. L. & Brummer, S. B. Activated Ir: An electrode suitable for reversible charge injection in saline solution. *J. Electrochem. Soc.* **130**, 731-733 (1983).
77. Lu, Y. *et al.* Anodically electrodeposited iridium oxide films microelectrodes for neural microstimulation and recording. *Sens. Actuators B Chem.* **137**, 334-339 (2009).
78. Meyer, R. D., Cogan, S. F., Nguyen, T. H. & Rauh, R. D. Electrodeposited iridium oxide for neural stimulation and recording electrodes. *IEEE Trans. Neural Syst. Rehabil. Eng.* **9**, 2-11 (2001).
79. Su, H.-C. *et al.* A cone-shaped 3D carbon nanotube probe for neural recording. *Biosens. Bioelectron.* **26**, 220-227 (2010).
80. Danieli, T., Colleran, J. & Mandler, D. Deposition of Au and Ag nanoparticles on PEDOT. *Phys. Chem. Chem. Phys.* **13**, 20345 (2011).
81. Castagnola, E. *et al.* PEDOT-CNT-Coated Low-Impedance, Ultra-Flexible, and Brain-Conformable Micro-ECoG Arrays. *IEEE Trans. Neural Syst. Rehabil. Eng.* **23**, 342-350 (2015).
82. Elschner, A., Kirchmeyer, S. & Lovenich, W. Ch. 1 - The Discovery and Development of Conducting Polymers. in *PEDOT: Principles and Applications of an Intrinsically Conductive Polymer* 1-20 (CRC Press, 2010). doi:10.1201/b10318-2
83. Elschner, A., Kirchmeyer, S., Lovenich, W., Merker, U. & Reuter, K. Ch. 4 - A Short History of the PEDOT Invention. in *PEDOT: Principles and Applications of an Intrinsically Conductive Polymer* 41-46 (CRC Press, 2010). doi:10.1201/b10318-5

84. Asplund, M. *et al.* Toxicity evaluation of PEDOT/biomolecular composites intended for neural communication electrodes. *Biomed. Mater.* **4**, 045009 (2009).
85. Chen, Y. *et al.* Poly(3,4-ethylenedioxythiophene) (PEDOT) as interface material for improving electrochemical performance of microneedles array-based dry electrode. *Sens. Actuators B Chem.* **188**, 747-756 (2013).
86. Venkatraman, S. *et al.* In Vitro and In Vivo Evaluation of PEDOT Microelectrodes for Neural Stimulation and Recording. *IEEE Trans. Neural Syst. Rehabil. Eng.* **19**, 307-316 (2011).
87. Wilks, S. Poly(3,4-ethylene dioxythiophene) (PEDOT) as a micro-neural interface material for electrostimulation. *Front. Neuroengineering* **2**, (2009).
88. Elschner, A., Kirchmeyer, S. & Lovenich, W. Ch. 2 - Conductive Polymers versus Metals and Insulators. in *PEDOT: Principles and Applications of an Intrinsically Conductive Polymer* 21-30 (CRC Press, 2010). doi:10.1201/b10318-3
89. Elschner, A., Kirchmeyer, S. & Lovenich, W. Ch. 7 - Counterions for PEDOT. in *PEDOT: Principles and Applications of an Intrinsically Conductive Polymer* 83-89 (CRC Press, 2010). doi:10.1201/b10318-8
90. Elschner, A., Kirchmeyer, S. & Lovenich, W. Ch. 6 - From EDOT to PEDOT: Oxidative Polymerization and Other Routes. in *PEDOT: Principles and Applications of an Intrinsically Conductive Polymer* 67-81 (CRC Press, 2010). doi:10.1201/b10318-7
91. Zhou, D. D., Cui, T., Hines, A. & Greenberg, R. J. Conducting Polymers in Neural Stimulation Applications. in *Implantable Neural Protheses 2* 217-252 (Springer Science & Business Media, 2010).

92. Sawyer, D. T., Sobkowiak, A. & Roberts, J. L. *Electrochemistry for Chemists*. (Wiley, 1995).
93. Samba, R., Chassé, T. & Stelzle, M. Is the enhanced adhesion of PEDOT thin films on electrodes due to sulfur-gold interaction - An XPS study. *Open Surf. Sci. J.* **5**, 17-20 (2013).
94. Kayinamura, Y. P., Roberts, J. H. & Rubinson, J. F. Near-Ohmic Behavior for Conducting Polymers: Extension Beyond PEDOT on Gold-Plated Platinum to Other Polymer-Counterion/Substrate Combinations. *ACS Appl. Mater. Interfaces* **4**, 1601-1607 (2012).
95. Kayinamura, Y. P., Ovadia, M., Zavitz, D. & Rubinson, J. F. Investigation of Near Ohmic Behavior for Poly(3,4-ethylenedioxythiophene): A Model Consistent with Systematic Variations in Polymerization Conditions. *ACS Appl. Mater. Interfaces* **2**, 2653-2662 (2010).
96. Shanmugasundaram, B. & Gluckman, B. J. micro-reaction chamber electrodes for neural stimulation and recording. in *EMBS* 656-659 (IEEE, 2011).
97. Cui, X. & Martin, D. C. Fuzzy gold electrodes for lowering impedance and improving adhesion with electrodeposited conducting polymer films. *Sens. Actuators Phys.* 384-394 (2003).
98. Lin, T.-H., Lin, C.-W., Liu, H.-H., Sheu, J.-T. & Hung, W.-H. Potential-controlled electrodeposition of gold dendrites in the presence of cysteine. *Chem. Commun.* **47**, 2044 (2011).
99. Chapman, C. A. R. *et al.* Nanoporous Gold as a Neural Interface Coating: Effects of Topography, Surface Chemistry, and Feature Size. *ACS Appl. Mater. Interfaces* **7**, 7093-7100 (2015).

100. Nick, C., Quednau, S., Sarwar, R., Schlaak, H. F. & Thielemann, C. High aspect ratio gold nanopillars on microelectrodes for neural interfaces. *Microsyst. Technol.* **20**, 1849-1857 (2014).
101. Seker, E. *et al.* The fabrication of low-impedance nanoporous gold multiple-electrode arrays for neural electrophysiology studies. *Nanotechnology* **21**, 125504 (2010).
102. Zhang, H., Shih, J., Zhu, J. & Kotov, N. A. Layered Nanocomposites from Gold Nanoparticles for Neural Prosthetic Devices. *Nano Lett.* **12**, 3391-3398 (2012).
103. Kim, R., Hong, N. & Nam, Y. Gold nanograin microelectrodes for neural interfaces. *Biotechnol. J.* **8**, 206-214 (2013).
104. Rose, T. L., Kelliher, E. M. & Robblee, L. S. Assessment of capacitor electrodes for intracortical neural stimulation. *J. Neurosci. Methods* **12**, 181-193 (1985).
105. Marin, C. Biocompatibility of intracortical microelectrodes: current status and future prospects. *Front. Neuroengineering* **3**, (2010).
106. Khodagholy, D. *et al.* Highly Conformable Conducting Polymer Electrodes for In Vivo Recordings. *Adv. Mater.* **23**, H268-H272 (2011).
107. Castagnola, V. *et al.* Parylene-based flexible neural probes with PEDOT coated surface for brain stimulation and recording. *Biosens. Bioelectron.* **67**, 450-457 (2015).
108. Pepin, B. *Transparent microECoG arrays for optogenetic mapping of surface potentials*. 31 (University of California at Berkley, 2013).
109. Elschner, A., Kirchmeyer, S., Lövenich, W., Merker, U. & Reuter, K. *PEDOT: Principles and Applications of an Intrinsically Conductive Polymer*. (CRC Press, 2010). doi:10.1201/b10318

110. Castagnola, E. *et al.* Biologically Compatible Neural Interface To Safely Couple Nanocoated Electrodes to the Surface of the Brain. *ACS Nano* **7**, 3887-3895 (2013).
111. Mandal, H. S. *et al.* Improving the performance of poly(3,4-ethylenedioxythiophene) for brain-machine interface applications. *Acta Biomater.* **10**, 2446-2454 (2014).
112. Castagnola, V., Bayon, C., Descamps, E. & Bergaud, C. Morphology and conductivity of PEDOT layers produced by different electrochemical routes. *Synth. Met.* **189**, 7-16 (2014).
113. Pettersson, L. A. A., Ghosh, S. & Inganäs, O. Optical anisotropy in thin films of Poly(3,4-ethylenedioxythiophene)-poly(4-styrenesulfonate). *Org. Electron.* 43-148 (2002).
114. Baek, S., Green, R. A. & Poole-Warren, L. A. The biological and electrical trade-offs related to the thickness of conducting polymers for neural applications. *Acta Biomater.* **10**, 3048-3058 (2014).
115. Fattahi, P., Yang, G., Kim, G. & Abidian, M. R. A Review of Organic and Inorganic Biomaterials for Neural Interfaces. *Adv. Mater.* **26**, 1846-1885 (2014).
116. Forcelli, P. A. *et al.* Histocompatibility and in vivo signal throughput for PEDOT, PEDOP, P3MT, and polycarbazole electrodes: Histocompatibility and In Vivo Signal throughput for Polymers. *J. Biomed. Mater. Res. A* **100A**, 3455-3462 (2012).
117. Aasmundtveit, K. E. *et al.* Structure of thin films of PEDOT. *Synth. Met.* 561-564 (1999).
118. Martin, D. C. *et al.* The Morphology of Poly(3,4-Ethylenedioxythiophene). *Polym. Rev.* **50**, 340-384 (2010).

119. Thaning, E. M., Asplund, M. L. M., Nyberg, T. A., Inganäs, O. W. & von Holst, H. Stability of poly(3,4-ethylene dioxythiophene) materials intended for implants. *J. Biomed. Mater. Res. B Appl. Biomater.* **93B**, 407-415 (2010).
120. King, Z. A., Shaw, C. M., Spanninga, S. A. & Martin, D. C. Structural, chemical and electrochemical characterization of poly(3,4-Ethylenedioxythiophene) (PEDOT) prepared with various counter-ions and heat treatments. *Polymer* **52**, 1302-1308 (2011).
121. Du, X. & Wang, Z. Effects of polymerization potential on the properties of electrosynthesized PEDOT films. *Electrochimica Acta* **48**, 1713-1717 (2003).
122. Tamburri, E., Orlanducci, S., Toschi, F., Terranova, M. L. & Passeri, D. Growth mechanisms, morphology, and electroactivity of PEDOT layers produced by electrochemical routes in aqueous medium. *Synth. Met.* **159**, 406-414 (2009).
123. Pigani, L., Heras, A., Colina, Á., Seeber, R. & López-Palacios, J. Electropolymerisation of 3,4-ethylenedioxythiophene in aqueous solutions. *Electrochem. Commun.* **6**, 1192-1198 (2004).
124. Duraisamy, N., Muhammad, N. M., Ali, A., Jo, J. & Choi, K.-H. Characterization of poly(3,4-ethylenedioxythiophene):poly(styrenesulfonate) thin film deposited through electrohydrodynamic atomization technique. *Mater. Lett.* **83**, 80-83 (2012).
125. Cui, X. & Martin, D. C. Electrochemical deposition and characterization of poly (3, 4-ethylenedioxythiophene) on neural microelectrode arrays. *Sens. Actuators B Chem.* **89**, 92-102 (2003).

126. Niu, L., Kvarnström, C., Fröberg, K. & Ivaska, A. Electrochemically controlled surface morphology and crystallinity in poly (3, 4-ethylenedioxythiophene) films. *Synth. Met.* **122**, 425-429 (2001).
127. Bard, A. J. & Faulkner, L. R. *Electrochemical methods: fundamentals and applications*. (Wiley, 2001).
128. Chen, Y.-C. *et al.* An active, flexible carbon nanotube microelectrode array for recording electrocorticograms. *J. Neural Eng.* **8**, 034001 (2011).
129. Campbell, S. A. *Fabrication Engineering at the Micro- and Nano-Scale*. (Oxford University Press, 2008).
130. Yeager, J. D., Phillips, D. J., Rector, D. M. & Bahr, D. F. Characterization of flexible ECoG electrode arrays for chronic recording in awake rats. *J. Neurosci. Methods* **173**, 279-285 (2008).
131. Mineev, I. R. *et al.* Electronic dura mater for long-term multimodal neural interfaces. *Science* **347**, 159-163 (2015).
132. Castagnola, E. *et al.* Smaller, softer, lower-impedance electrodes for human neuroprosthesis: a pragmatic approach. *Front. Neuroengineering* **7**, (2014).
133. Khodagholy, D. *et al.* High Speed and high density organic electrochemical transistor arrays. *Appl. Phys. Lett.* **99**, 1-3 (2011).
134. Liang Guo, Meacham, K. W., Hochman, S. & DeWeerth, S. P. A PDMS-Based Conical-Well Microelectrode Array for Surface Stimulation and Recording of Neural Tissues. *IEEE Trans. Biomed. Eng.* **57**, 2485-2494 (2010).
135. Green, R. A. *et al.* Substrate dependent stability of conducting polymer coatings on medical electrodes. *Biomaterials* **33**, 5875-5886 (2012).

136. Timoshenko, S. & Woinowsky-Kreiger, S. *Theory of Plates and Shells*. (McGraw Hill Book Company, Inc., 1959).
137. Ashby, M. F. *Materials Selection in Mechanical Design*. (Elsevier Ltd., 2011).
138. Harder, T. A., Yao, T.-J., He, Q., Shih, C.-Y. & Tai, Y.-C. Residual Stress in Thin-Film Paralene-C. *IEEE* 435-438 (2002).
139. Sim, W., Kim, B., Choi, B. & Park, J.-O. Theoretical and experimental studies on the parylene diaphragms for microdevices. *Microsyst. Technol.* **11**, 11-15 (2005).
140. Pandey, G. P. & Rastogi, A. C. Synthesis and characterization of pulsed polymerized poly(3,4-ethylenedioxythiophene) electrodes for high-performance electrochemical capacitors. *Electrochimica Acta* **87**, 158-168 (2013).
141. Ballanyi, K. & Ruangkittisakul, A. Brain Slices. *Encyclopedia of Neuroscience* 483-490 (2009).
142. Ferrea, E. *et al.* Large-scale, high-resolution electrophysiological imaging of field potentials in brain slices with microelectronic multielectrode arrays. *Front. Neural Circuits* **6**, (2012).
143. Du, J., Blanche, T. J., Harrison, R. R., Lester, H. A. & Masmanidis, S. C. Multiplexed, High Density Electrophysiology with Nanofabricated Neural Probes. *PLoS ONE* **6**, e26204 (2011).
144. Kwiat, M., Stein, D. & Patolsky, F. Nanotechnology meets electrophysiology. *Curr. Opin. Biotechnol.* **24**, 654-663 (2013).
145. Sarma, M. S. *Introduction to electrical engineering*. (Oxford University Press, 2001).

146. Ramachandra, R. & Subramanian, T. *Atlas of the Neonatal Rat Brain*. (CRC Press, 2011).
147. Binder, M. D. Glutamate. in *Encyclopedia of Neuroscience 1749-1753* (Springer).
148. Campbell, S. A. Chemical Vapor Deposition. in *Fabrication Engineering at the Micro and Nanoscale 356-390* (Oxford University Press, 2008).
149. Campbell, S. A. Vacuum Science and Plasmas. in *Fabrication Engineering at the Micro and Nanoscale 259-282* (Oxford University Press, 2008).
150. Williams, K. R., Gupta, K. & Wasilik, M. Etch rates for micromachining processing-part II. *J. Microelectromechanical Syst.* **12**, 761-778 (2003).
151. Campbell, S. A. Etching. in *Fabrication Engineering at the Micro and Nanoscale 283-313* (Oxford University Press, 2008).
152. Campbell, S. A. Optical Lithography. in *Fabrication Engineering at the Micro and Nanoscale 165-198* (Oxford University Press, 2008).
153. Campbell, S. A. Physical Deposition: Evaporation and Sputtering. in *Fabrication Engineering at the Micro and Nanoscale 323-355* (Oxford University Press, 2008).
154. Hung, A., Goldberg, I. B. & Judy, J. W. Stimulation Electrode Materials and Electrochemical Testing Methods. in *Implantable Neural Prostheses 2 191-216* (Springer Science & Business Media, 2010).
155. *Handbook of Reference Electrodes*. (Springer Berlin Heidelberg, 2013). doi:10.1007/978-3-642-36188-3
156. Bott, A. W. Practical Problems in Voltammetry 3: Reference Electrodes for Voltammetry. *Curr. Sep.* **14**, 64-68 (1995).

---

**APPENDIX A -**  
**FABRICATION AND CHARACTERIZATION**  
**METHODS FOR  $\mu$ ECOG DEVICES**

---

**APPENDIX A.1 -**  
 **$\mu$ ECOG DEVICE FABRICATION METHODS**

**APPENDIX A.2 -**  
**METHODS OF DEVICE CHARACTERIZATION**

# A.1 - $\mu$ ECOG DEVICE FABRICATION METHODS

The devices were fabricated using standard lithographic techniques, in which materials are deposited onto a planar substrate and then patterned using photolithography. The microfabrication methods briefly described here are: chemical vapour deposition (CVD) for insulating layers, reactive ion etching (RIE) with oxygen plasma for dry etching polymer, mask-based contact lithography for patterning, and physical vapour deposition (PVD) of metallic layers.

## A.1.1 CHEMICAL VAPOUR DEPOSITION / POLYMERIZATION OF PARYLENE-C:

Chemical vapour deposition (CVD) is a vacuum chamber process that vaporizes chemical precursors or reactants into a deposition chamber where the low pressure allows for the uniform and even deposition of a material coating on all available surfaces within the entire deposition chamber.<sup>148</sup>

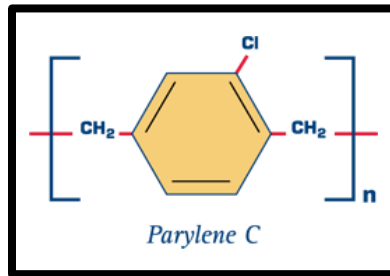


**Figure 62** – Parylene-C (P-C) monomer molecular model.

The P-C molecules are vaporized at 175°C and heated to 690°C, at which point the molecules have become monomers, as shown in Figure 73, above, and upon introduction to the room temperature deposition chamber seek to reduce their free energy by reacting with another chemical or binding to a surface.<sup>148</sup> Keeping low pressure in the deposition chamber and rotating the sample holder, more uniform coatings of deposited P-C were obtained.<sup>148</sup> The

minimum achievable thickness of P-C that is continuous and pin-hole-free, as reported by Khodagholy, et al. is 2  $\mu\text{m}$ .<sup>67</sup>

Interestingly, in the case of Parylene-C (P-C) deposition, whether or not it is truly CVD and not thermal PVD is a matter of some contention.<sup>148</sup> In the case of P-C, the reaction is polymerization individual monomers and so the classification as chemical or physical vapour deposition is kind of ambiguous, but for this work it will be considered as CVD.

### A.1.2 REACTIVE ION ETCHING WITH O<sub>2</sub> PLASMA:

Reactive ion etching (RIE) was developed for anisotropic highly-directional etching using plasma by utilizing the directionality of an electric field and the charged species of plasma. A strong electrical field oscillating at a radio frequency (RF) of 13.56 MHz between two parallel plates is generated (along with a DC electrical field) using an additional RF power supply, dielectric breakdown of the gas in the chamber occurs and “sparks” the oxygen gas into plasma.<sup>149</sup> Due to the RF electrical field, the oxygen ions are unable to cover the same distance as the nearly weightless free-electrons are able to, resulting in a concentrated form of oxygen plasma in close proximity to the wafer. These oxygen radicals, being highly energetic and reactive and break the molecular bonds of organic materials.<sup>150,151</sup>

### A.1.3 OPTICAL LITHOGRAPHY:

Optical lithography is a process in which a physical mask protects certain areas of a photoactive resist-coated wafer from exposure to UV light. With opaque and transparent areas used to mask-off areas and selectively activate light-activated chemicals in photoresist (PR) that has been spread very thinly and evenly on a Si wafer by spin-coating and soft-baking, with sufficient exposure to a UV light, a pattern can be developed within the PR layer through light activated changes in the solubility of the PR in certain developer solutions.<sup>152</sup>

Whether the exposed area becomes soluble or insoluble in the developer solution depends on the PRs classification as either a positive or negative resist, respectively. In some cases a PR can be either positive or negative, such as AZ 5214-E Image Reversal (IR) PR. The fabrication of micro-scale features with mask-based contact lithography is limited to a minimum achievable feature-width of  $2\ \mu\text{m}$ , which was not a limitation for my design and therefore contact lithography is very suitable for fabrication.<sup>152</sup>

### POSITIVE TO NEGATIVE IMAGE REVERSIBLE OF AZ 5214-E

Initially a positive resist, AZ 5214-E is capable of becoming negative and thereby reversing which areas are made soluble in the patterning process through a controlled, post-patterning heat treatment followed by a 60 s mask-less flood exposure to UV light. Refer to Figure 74, below.

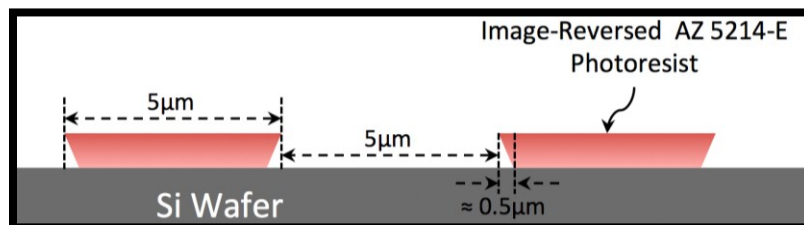


**Figure 63** – An illustrative schematic showing a developed photoresist layer which, due to the IR processing performed, now exhibits a slightly undercut sidewall that is ideal for lift-off patterning.

After this image reversal protocol is followed, the pattern in the positive photoresist develops as a negative resist would. In this case, the sidewalls of the patterns are left under-cut, making them ideal for patterning by lift-off.<sup>151</sup>

#### A.1.4 PHYSICAL VAPOUR DEPOSITION:

The metallic layers are deposited using a style of physical vapour deposition (PVD) called sputtering. Sputtering is accomplished by accelerating heavy, argon ions ( $\text{Ar}^+$ ) into a negatively polarized target metal. As the high-momentum  $\text{Ar}^+$  ions bombard the target surface with tremendous force, it jeopardizes the metallic lattice, and atoms are repeatedly jettisoned from the metal target surface, sputtering atoms of the target material onto any and all surfaces in their path.<sup>153</sup> This process can be done for periods of time ranging from seconds to tens of minutes, but by magnetically constricting the argon-plasma, enhanced metal deposition rates can be achieved through increased ion collisions with the target surface.<sup>153</sup>

## A.2 - METHODS OF DEVICE CHARACTERIZATION

The characterization methods executed in this project were contact profilometry step-height testing, 4-point probe thin film resistivity testing and optical microscopy to check for visible defects in devices during and after the fabrication process.

### A.2.1 SURFACE CONTACT PROFILOMETRY

Contact profilometers, such as the Alphastep iQ surface profilometer (KLA Tencor; [www.kla-tencor.com](http://www.kla-tencor.com)) I used in this work, are capable of measuring very small changes in the z-axis (up-down) that occur and as the probe's stylus-tip was rastered along a specified linear pathway recording them. The stylus tip, typically made of diamond or a similarly hard material and sits at the end of a cantilevered beam that is controlled and monitored by piezoelectric actuators and sensors.<sup>129</sup>

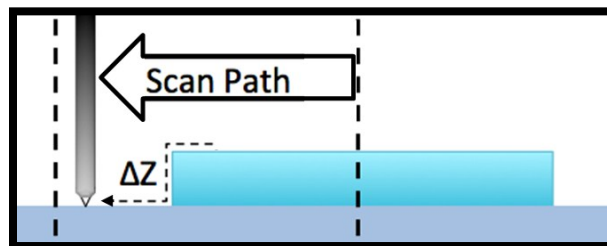


**Figure 64** – An illustrative schematic of contact profilometry.

By applying a specific amount of potential, the piezoelectrics allow for a specific amount of stylus force to be initially exerted. As the tip's position changes (as shown in Figure 75), any z-axis change causes a response in potential of the piezoelectrics. This response was used to provide detailed information about the surface being inspected.

## A.2.2 OPTICAL MICROSCOPY

The use of an optical microscope to check for defects was performed throughout the fabrication process helps to keep track of badly formed devices or contaminated or otherwise defective electrode pathways. The use of optical microscopy was most useful during the lithographical process steps because the quality of the photoresist development can drastically change the yield of devices on a wafer or in an entire batch.

## A.2.3 FOUR-POINT PROBE

A Pro-4 Four Point Probe (4PP) Resistivity System (Lucas Labs; [www.lucaslabs.com](http://www.lucaslabs.com)) powered by a Keithley 2601A System Power Source Meter (Keithley; [www.keithley.com](http://www.keithley.com)) was used along with measured step-height data to measure the resistivity of the Au-Ti metallic layer. Designed to measure the electrical resistivity,  $\rho$ , (or inversely conductivity,  $\sigma$ ,) as the thickness of a metallic conductor is reduced to the nano-scale, the intrinsic material property of resistivity begins to increase relative to that of the macro-scale bulk metal. An illustrated schematic, Figure 76, is shown below that graphically demonstrates the usage of a 4-point probe system.

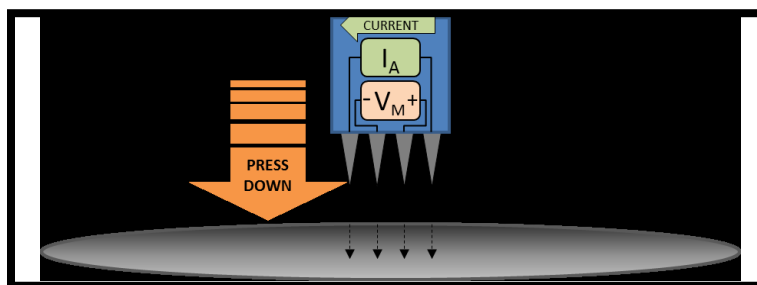


**Figure 65** – Illustrated schematic of a 4-point probe tip above a Si test substrate.

Current was applied between the outermost probes while the innermost probes measured the resulting voltage. Spacing between each probe tip was kept equal between neighbouring probes and fixed at a value 500  $\mu\text{m}$ .

---

**APPENDIX B -**  
**SUPPLEMENTAL ELECTROCHEMISTRY**  
**BACKGROUND**

---

**APPENDIX B.1 - BASICS OF THREE-ELECTRODE**  
**CELLS**

**APPENDIX B.2 - WORKING ELECTRODES**

**APPENDIX B.3 - COUNTER ELECTRODES**

**APPENDIX B.4 - REFERENCE ELECTRODES**

**APPENDIX B.5 - MAINTENANCE AND STORAGE OF**  
**REFERENCE ELECTRODES**

## B.1 - BASICS OF THREE-ELECTRODE CELLS

This section overviews the concept of a three-electrode cell followed by the roles of the three electrodes themselves.

A three-electrode electrochemical cell involves the use of a working electrode (WE), auxiliary or counter electrode (CE), which is the same as a two-electrode electrochemical cell, but includes an additional electrode, the reference electrode (RE), to more accurately measure the deposition potential of the WE.<sup>127</sup> See Figure 77, below, for an illustration showing the arrangement of the three electrodes within the cell.

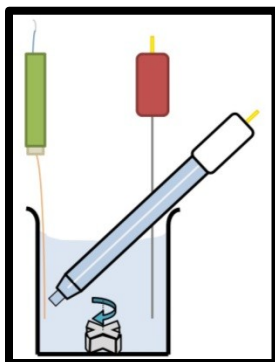


**Figure 66** – An illustrated the three-electrode cell with an X-shaped Teflon<sup>®</sup>-coated magnetic stir bar at the bottom of the cell container, a green capped WE on the left, a Red capped CE on the right and a white capped RE resting diagonally.

In a two-electrode cell, the potential measured between the WE and CE electrodes includes an additional quantity of potential known as resistance overpotential that results from having to overcome the resistance to ionic transport through the electrolyte solution ( $R_s$ ) to supply the required current for the constant-current deposition process.<sup>127</sup> The reason the use of a RE was practical was because of the removal of the majority of this overpotential from the measured potential at the WE, as well as for other reasons that will be touched on shortly.<sup>92,127</sup> Figure 78, below, shows the relative amount of solution

resistance contributing to the measured potential with a RE ( $R_{RE}$ ) instead of a CE.

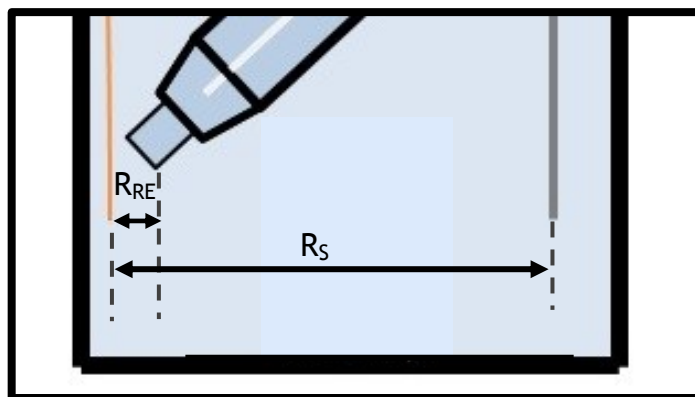


**Figure 67** – Magnified illustration of the three-electrodes (WE, RE, CE from L to R) shown in Figure 76 visually showing the solution resistance ( $R_S$ ) removed from any potential measurements and the reduced RE solution resistance ( $R_{RE}$ ).

Next we will look at the various electrode roles, material choices and the reasons for their selection, beginning with the WE, followed by the CE and finishing with the RE.

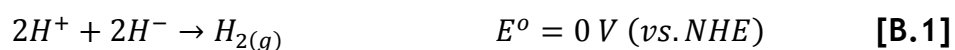
## **B.2 - WORKING ELECTRODES**

It is the working electrode (WE) that undergoes the desired electrochemical half-cell reaction and therefore experiences the electrode reaction of interest as its potential is forced to adhere to an electrochemical process with pre-set program parameters as controlled by the instrumentation.<sup>92,127,154</sup>

## **B.3 - COUNTER ELECTRODES**

The counter or auxiliary electrode (CE) was required to complete the electrical circuit through the electrochemical cell by providing an additional, complimentary half-cell reaction. Two half-cell reactions, one occurring at each electrode, are involved in every electrochemical cell, but to look at just one electrode and observe its half-cell reaction potential a specific,

standardized CE half-cell reaction must be used.<sup>127</sup> The standardized half-cell reaction typically used is the standard hydrogen reduction reaction in which two hydrogen ions ( $H^+$ ) from the electrolyte solution gain two electrons ( $e^-$ ), typically from an inert, platinum (Pt) electrode, forming into a hydrogen gas molecule ( $H_{2(g)}$ ), which under standard conditions has arbitrarily been given the standard reduction reaction potential,  $E^0 = 0\text{ V}$  for clarity and consistency between researchers.<sup>127</sup> The standard NHE reduction reaction is shown in **Equation B.1**, below.



Used as one half-cell reaction in an electrochemical cell reaction, the standard or normal hydrogen electrode reaction (SHE or NHE) allows the measured reduction/oxidation potential to be purely representative of the other half-cell electrode reaction being investigated.<sup>155</sup> These reference potentials are indicated next to the potential value itself to indicate the reference point. The counter electrode material typically used for this reaction is platinum (Pt) because it is a high purity noble metal that is relatively inert, oxidation resistant, and an effective  $H_2$  catalyzer by lowering the activation overpotential required to form hydrogen gas bubbles.<sup>92,127</sup> At negative electrode potentials, Pt has the tendency to adsorb aqueous H atoms, catalyzing  $H_2$  gas generation while as positive electrode potential rises, even noble metals like Pt will form an oxide layer at some point.<sup>92</sup>

Au, although also a noble metal, is more easily oxidized than Pt in the presence of halide or cyanide solutions. Au begins to oxidize at electrode potentials greater than  $+0.760\text{ V}$  (vs. NHE), forming ionic complexes with halide or cyanide ions within concentrated solutions.<sup>34</sup> Based on the aforementioned information a Pt wire was used as CE for these experiments. However, due to the size and complexity of setting up a NHE as a reference electrode, its sole purpose was to be a source or sink for the current required at the WE, and

therefore a RE with a more functional and easily applied half-cell reaction was used for the sake of measuring the WE half-cell reaction potential.

## **B.4 - REFERENCE ELECTRODES**

As mentioned earlier, the use of a reference electrode (RE) in addition to a CE is a way of improving the accuracy of WE potential measurements by removing the solution resistance overpotential.<sup>127</sup> In addition to this, RE provide a known half-cell reaction potential to reference the measured potential against the WE, exactly as in the case of the NHE previously discussed (e.g.  $E^{\circ}_{\text{Ag}|\text{AgCl}} = 0 \text{ V}$  vs. Ag|AgCl).

Many considerations need to be made when selecting a RE for a specific experiment, such as its polarizability, size, electrolyte, temperature sensitivity and the half-cell reactions.<sup>127,155</sup> Regarding electrode polarizability, a non-polarizable electrode (NPE) is desirable because as current flows through the cell a RE potential should remain fixed at its standard potential.

### **B.4.1 SILVER-SILVER CHLORIDE RE (AQUEOUS):**

For aqueous electrochemical processes, a silver-silver chloride RE from BAS Inc. was used: Ag|AgCl|KCl (sat'd).<sup>127</sup> The standard half-cell reaction is shown below in **Equation B.2**.<sup>156</sup>



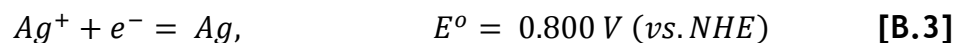
The choice to use an aqueous silver-silver chloride (Ag/AgCl) RE was made based on several factors: it is one of the most effective and widely used aqueous RE in the available literature; it is low cost; it has a fast, one electron reaction; it is relatively non-polarizable; it has good temperature stability; its half-cell reaction creates Cl<sup>-</sup> ions which were already present in the bulk electrolyte solutions; and it has a compact design that was easy to use.<sup>155</sup> The

simple and compact design of Ag|AgCl RE made it much easier to set up within the cell container and was better able to get into close proximity of the WE.<sup>2</sup> It is also a robust RE and has a long performance lifetime with proper storage and maintenance.<sup>2</sup> However, due to the presence of perchlorate ions in the non-aqueous electrolyte, the potassium ions would have had the tendency to form crystals within the glass frit tip, raising the RE impedance, and therefore a separate RE was selected for the non-aqueous electrolytes.

#### B.4.2 SILVER-SILVER ION RE (NON-AQUEOUS):

In addition to avoiding insoluble salt crystal formation within the glass-frit tip of the Ag|AgCl RE, a non-aqueous RE was used for processes with the non-aqueous solvent ACN to prevent contamination due to water leakage from an aqueous RE.<sup>155,156</sup>

For the non-aqueous electrolyte solutions a silver-silver ion RE from BAS Inc. was used: Ag<sup>+</sup>|Ag|AgClO<sub>4</sub> (0.01M). The standard half-cell reaction of the silver-silver ion RE (Ag|Ag<sup>+</sup>) is shown in **Equation B.3** below.



The Ag|Ag<sup>+</sup> RE contained an electrolyte solution with a chemical composition of 0.01 M AgClO<sub>4</sub> in ACN solvent. This reference electrode shared many of the positive traits found in the Ag|AgCl RE, such as low cost, compact design and ease of use with the exception that the electrolyte solution had to be replaced fairly regularly to maintain its efficacy over time.<sup>155</sup>

Finally, I review of the storage practices for maintaining the accuracy of a RE between experiments and over reasonable periods of time.

## B.5 - STORAGE OF REFERENCE ELECTRODES

- Ag|AgCl Aqueous RE Storage Solution:  
Saturated potassium chloride in distilled water (Saturated KCl in DI)
- Ag|Ag<sup>+</sup> Non-Aqueous RE Storage Solution:  
0.01 M lithium perchlorate in acetonitrile (0.01 M LiClO<sub>4</sub> in ACN)

Careful maintenance and storage of the reference electrodes are required to prevent an electrodes reduction potential from shifting away from its initial state - due to the sensitive nature of the electrodes and the ongoing striving toward a state of dynamic equilibrium in the system.<sup>92,127,155</sup>

Electrodes were stored in containers in which the RE tip was kept submerged in solution but suspended in an upright position above the container bottom, as shown in Figure 79, below.<sup>156</sup>



**Figure 68** – A properly stored non-aqueous Ag|Ag<sup>+</sup> RE being kept in a storage container filled to an adequate level with the appropriate storage solution.  
(0.01 M LiClO<sub>4</sub> in ACN)

Throughout these experiments the storage solutions in the containers were refreshed regularly to maintain the equilibrium of all experimentally used reference electrodes.